Quantum dots in a hybrid superconducting-semiconducting architecture

David-Dominik Jarausch

Zurich, 13 February 2013

Master Thesis

Quantum Device Lab
Nanophysics Group

Laboratory for Solid State Physics
ETH Zurich

Supervisors: Dr. Julien Basset
Tobias Frey

Prof. Dr. Andreas Wallraff
Prof. Dr. Klaus Ensslin
Prof. Dr. Thomas Ihn

Abstract

Mesoscopic semiconductor structures are remarkable devices to investigate the fundamentals of quantum physics. Major advances in fabrication technology allow us to fabricate nanostructures and study the dynamics of single electrons in such devices. Recently, Frey *et al.* realized dipole coupling of a semiconductor double quantum dot to a superconducting transmission line resonator. Such a system permits to study cavity QED in an all-solid state device, fabricated on a common chip, and adds a new architecture to the already highly successful and prospering field of circuit QED. Although coupling strengths on the order of a few tens of MHz were shown, such a system still suffers from high dephasing rates. This thesis reports on studies of a single electron double quantum dot that is dipole coupled to a superconducting transmission line resonator. Decoherence is studied when reducing the number of electrons within the quantum dot. In the limit of a single electron double quantum dot, one electron remains that is delocalized between both dots and dipole coupled to a resonator. It is found by comparison between experimental data and numerical simulations that dephasing rates remain large and range from approximately 400 MHz to 5.8 GHz. An increase in the single-particle level spacing did not have a major effect on dephasing in such a system. We conclude that the coupling to excited states in a double quantum dot is not dominating for qubit dephasing. Other decoherence mechanisms are discussed.

Contents

1 Introduction

The theory of computation has traditionally been studied almost entirely in the abstract, as a topic in pure mathematics. This is to miss the point of it. Computers are physical objects, and computations are physical processes. What computers can or cannot compute is determined by the laws of physics alone, and not by pure mathematics.

David Deutsch

In classical computation, the bit is the fundamental unit for computation and computation is based on the laws of classical physics. Quantum computation is based on a similar concept, the quantum bit (qubit). Analogous to the classical bit, a qubit is a physical system that has two distinct states. However, on the contrary to classical computation, quantum computers obey the laws of quantum mechanics. While classical bits remain either in one state or the other of two possible configuration, a qubit can be in a superposition of both states at any time such as $|\Psi> = \alpha|0> + \beta|1>$ where α and β are complex quantities and $|\Psi>$ denotes the quantum state. An introduction to quantum computation and qubits can be found in [1]. The possibility of a qubit to be in a superposition of two states at any given time makes it special in terms of parallel computations. In such a computer, that is based on the laws of quantum mechanics instead of classical physics, certain computational task could be carried out more efficiently by using special quantum properties of the system such as entanglement and superposition (cf. e.g. prime factorization on a quantum computer [2]).

Realizing a computer based on qubits remains extremely challenging. A key feature is classical and quantum noise that leads to decoherence. The ratio between coherence time τ_Q to τ_{op}, the time for elementary unitary transformations, may serve as a characteristic for different physical implementations of quantum bits [3]. An estimation of this quantity gives insights into the merits of different physical realizations. Quantum gates have been shown e.g. with high fidelities in trapped ion systems. Here, a two-qubit gate with fidelities reaching 97%, in the example of a geometric phase gate, could be realized [4]. A complementary approach are artificial atoms that can be realized in an all-solid design on a common chip. Two promising candidates are superconducting qubits [5] and lateral quantum dots [6], fabricated on a chip with techniques borrowed from integrated circuit technology. This approach shows several benefits in terms of scalability and fast operation times whereby long-range qubit interactions can be mediated by a quantum bus, e.g. a superconducting coplanar waveguide that is used to couple different qubits. While such an architecture has been studied widely for superconducting qubits [5, 7, 8], the coupling of quantum dots to transmission line resonators remains a relatively new field. Such a hybrid all-solid quantum device may serve as a building block in a quantum network that couples different qubits respectively different qubit architectures via a common quantum bus [9]. Here, different architectures can be exploited in terms of their individual merits. In such a quantum network, trapped ions may serve as a quantum storage, benefiting from superior coherence and relaxation times, while quantum dots might serve as computation clusters, possessing fast two-qubit operations using exchange coupling between nearest-neighbor systems and showing excellent controllability of quantum states. For instance, fast two-qubit operations in the order of 180 ps were shown [10, 11] in quantum dot architectures. Additionally, quantum dots have the benefit to control quantum mechanical properties and to manipulate quantum states by externally applied currents or voltages

which allows for a high control over the dot. In addition to widely used superconducting qubits, electrons are not paired in quantum dots which allows easier access to the spin degree of freedom.

A semiconductor double quantum dot (DQD) that is coupled to a superconducting coplanar waveguide (CPW) resonator was lately investigated [11, 12, 13]. In such an architecture, the double quantum dot serves as a qubit while the CPW resonator is used for read-out. Coupling the double dot to a resonator, the physical properties of the dot can be explored via the microwave resonator and vice versa [14, 15], with the benefit of coupling the double dot to a remote qubit via the transmission line. Such a design allows to acquire information on the charge state without requiring a separate mesoscopic detector on chip [16]. In a typical setup, a quantum point contact (QPC, cf. also [17]) or direct current (DC) transport measurements are used to readout the dot state. In addition to a DC measurement, no current is required to flow through the quantum dot such that this novel approach serves as a noninvasive readout technique for spin and charge states [14, 16].

So far, the dot was studied in the many [12] electron regime when coupled to a resonator. This has the possible drawback that additional electrons in the quantum dot and/or close-lying excited states in a many electron regime might have a negative influence on decoherence of the qubit state. Futhermore, many electron quantum dots complicate possible qubit states through a hybridization of different charge states in the individual dots and many-body quantum effects. This work reports on a double quantum dot that can be analyzed by DC, QPC and microwave measurements in the many, few and single electron regime. This allows to investigate the properties of a double quantum dot, benefiting from different read-out techniques in a single electron regime. The applied dot design is first analyzed with respect to possible benefits as well as drawbacks on the way to a single electron device. Here, both dots are completely emptied, but a single electron is left delocalized between dots. Benefiting from a better understanding of the sample characteristics, the double dot qubit is studied in the single electron regime. A Markovian master equation approach allows for a numerical simulation of the coupled qubit-resonator system and enables to extract characteristic parameters such as coupling strength and decoherence rate. Comparing those characteristics in the single electron with the many electron regime within the same sample, both regimes are analyzed in terms of decoherence. This might give additional insights on the questions whether close-lying excited states in the many electron regime serve as an additional decoherence channel.

2 Quantum dots in a circuit QED architecture: A hybrid system

Lateral quantum dots are mesoscopic devices in a solid-state structure in which electrons are confined in a potential well. Such a structure can comprise a single electron in a confining potential up to several hundreds or thousands of electrons. This thesis reports on gate defined lateral quantum dots [18]. For a review on self-assembled quantum dots, please refer to [19]. Lateral quantum dots are formed on a semiconductor heterostructure, in which electrons are confined at the interface between two semiconductors such as GaAs and AlGaAs (cf. Fig. 1a). Electrons are free to move in the interface plane but are confined normal to the interface. In the quantum limit of a 2DEG, electronic states are quantized in the third dimension, yet the quantization energy is large such that the electrons are thought to be in their ground state when operated at mK temperatures. Such a two-dimensional electron gas (2DEG) is of great importance in many experiments in nanophysics. Please refer to [20] for more information on semiconductor nanostructures and 2DEGs in particular.

Starting from a 2DEG in which electrons are tightly confined normal to the surface, a quantum dot can be formed by confining electrons in the remaining two dimensions. This may be achieved by depleting electrons in certain regions of the 2DEG with techniques such as local oxidation [21] or appropriately biased metallic top-gates i.e. Schottky gates. In the following studies, the confining potential was created by metallic top-gates only. Biasing those gates negatively, depletion regions form below and electrons become confined in the remaining two dimensions, in the heterostructure interface. Depending on dot size and applied gate voltage, the zero dimensional quantum dot is weakly tunnel coupled to source and drain reservoirs while electrons occupy discrete energy levels within the dot. Single electrons can tunnel from source to unoccupied energy states when sufficient in energy whereby the width of the well and the tunnel rate can be controlled with the applied voltage to top-gates. In such a device, the dynamics of single electrons in a quantum dot respectively the transport of a single electron from source to drain via dot levels can be experimentally analyzed. Especially tunneling of single electrons is at the heart of quantum mechanics and of great interest in man-made mesoscopic structures. Fig. 1a shows a schematic of a GaAs/AlGaAs heterostructure that comprises a 2DEG 90 nm below the surface. Such a configuration is identical to the heterostructure used in all following experiments. For a reference on the physical properties and designs of semiconductor heterostructures, please refer to [22]. A scanning electron microscope (SEM) picture that shows the shape of the gates defining a DQD, similar to the sample used in this study, is given in Fig. 1b. Metallic top-gates are visible that form two tunnel coupled potential wells when depleting parts of the 2DEG around the gate. Note that the biased gates not only form the double well, but also give the static potential within the dot. Two plunger gates enable to additionally change the static potential and thereby the energy levels within the dot which allows to independently vary the dot potential while maintaining the overall dot characteristics such as interdot tunneling rates and coupling to the leads in a first approximation, as a finite cross-coupling might be evident.

In the following hybrid architecture, a DQD, that is two tunnel coupled quantum dots, is dipole coupled to a cavity such as a transmission line resonator. This approach is similar to the well established and successful field of circuit QED with superconducting quantum bits [23] except for replacing superconducting qubits with quantum dots. In both architectures, the qubit can be controlled and readout via a CPW resonator whereas quantum dot qubits have additionally the benefit to access the spin degree of freedom.

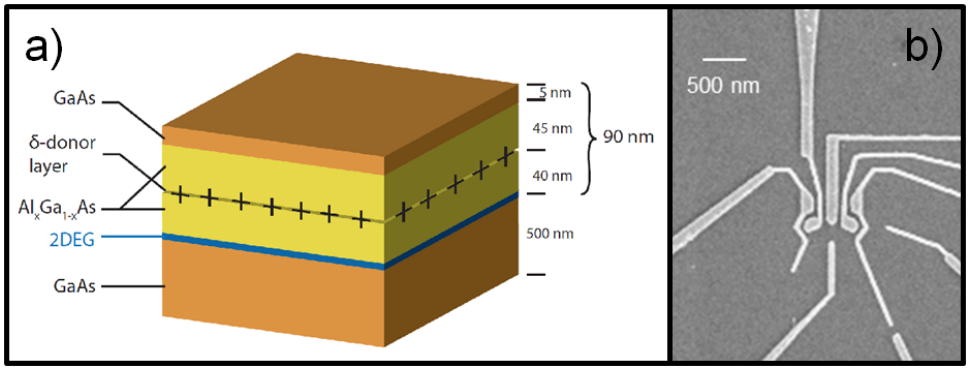

Figure 1: a) GaAs/AlGaAs heterostructure with a 2DEG confined 90 nm below the surface, adopted from [24], b) SEM picture of the metallic gate shapes that define the DQD. This design is identical to the sample used for all experiments, described in the following. Picture by courtesy of Dr. Julien Basset, ETH Zurich

2.1 Sample geometry

For a full characterization of the double dot, a readout of the charge state is intended to be possible via the transmission line in a microwave regime as well as through direct current measurements or by using a QPC as an embedded charge detector, first employed in measurements by Field *et al.* [17]. Manipulation and readout should be feasible both in the many and single electron regime. The employed structure of the double dot will allow for a high tunability, changing from a single dot to a double dot configuration. This section intends to discuss the realized sample design. Different designs approaches were investigated in earlier projects [12, 14, 15, 24], which lead to the final sample geometry that was used in this work.

The sample employed in this thesis is special as it allows for probing the dynamics of single electrons in a double quantum dot structure in direct current (DC) measurement as well as probing the electronic state using a quantum point contact (QPC). Complementary, the DQD can be investigated via its capacitive coupling to a superconducting microwave transmission line resonator (Chapter 4). Fig. 2a shows an optical photograph of the GaAs/AlGaAs heterostructure with resonator and DQD. This design is similar to the one used in the following experiments which remained under investigation at the current point of time and no photograph was available.

Regions of the chip in dark gray color show the GaAs/AlGaAs heterostructure with a 2DEG at 90 nm below the surface in a design identical to Fig. 1a. The position of the DQD (red circle in Fig. 2b) was chosen such that it is situated at an antinode of the fundamental mode and capacitively coupled to the resonator by an extension of the center conductor, shown in Fig. 2b. Titanium-gold top-gates (Ti(3nm)Au(25nm) for small structure in Fig. 1b and Ti(3nm)Au(55nm) for golden structure in Fig. 2a) are shown and biased via contacts labeled C in the picture. Ohmic contacts, indicated by M, allow to access the 2DEG directly and to measure a direct current through the double quantum dot or QPC detector. An enlarged picture of the top-gates that form the DQD is shown in Fig. 1b for a small and in Fig. 4 for a wider region. Top-gates are defined in an electron beam lithographic process. Resonator‘s (R) center conductor and ground plane were defined by photo-lithography. Here, 3 nm titanium and 200 nm aluminum were deposited on top of the heterostructure. Center conductor and ground plane are shown

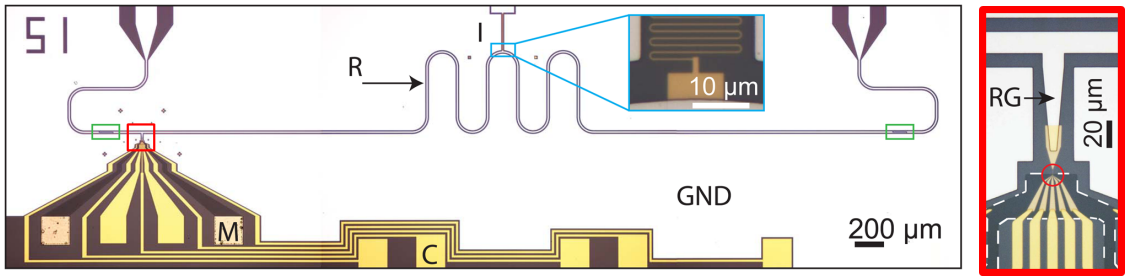

Figure 2: a) Optical photograph of a similar sample design, showing resonator (R), ohmic contacts (M), metallic top-gates (C), inductor (I), b) enlarged view of the extended resonator center conductor that forms the resonator gate (RG) on the DQD (red circle). Metallic top-gates are shown in gold. The dark gray area shows regions of two dimensional electron gas. The 2DEG is etched away at the resonator position (white and light gray shaded region). Adopted from [24]

by the white areas in Fig. 2, separated by a gap (light-gray area) of 7.1 μm. In this area, the 2DEG was wet-etched to avoid for an additional dissipative channel of resonator excitations into the 2DEG. An inductor, shown in the inset in Fig. 2, allows to bias the center conductor, which is capacitively coupled via an extension to one of the two dots. Biasing the center conductor sets a constant offset on top of the oscillating potential that is given by the resonator field. Thus, an external voltage applied to the center conductor, which is connected to one of the plunger gates, changes the static potential in the coupled dot as capacitively coupled to the dot. The transmission line resonator is accessed through a capacitive coupling to input respectively output transmission lines by means of finger capacitors (cf. [25] for a review on coplanar waveguide resonators). The total resonator length is 8205 μm by excluding the input/output capacitors with a total width of the center conductor of 10 μm, chosen by design.

2.2 Resonator design

A superconducting transmission line resonator is used to realize the resonator which is coupled to the DQD. The initial idea is comparable to a coaxial line with center conductor and ground plane, whereas in this design such an architecture was realized in two dimensions only. Additionally to a 2D coaxial line, the center conductor was cut at both ends such that the electromagnetic wave is reflected at an open end thereby forms the resonator. The resonator is coupled capacitively to input and output transmission lines. In the current design, finger capacitors (cf. eg. [7, 15]) are used, indicated by two green boxes in Fig. 2a. Please refer to [25] for a more comprehensive review on transmission line resonator. A description of relevant length scales is given in the previous section. Fig. 3 shows a typical transmission spectrum of the resonator for a configuration at which all top-gates are set to 0 V, except for LPG which was set to -450 mV. The value for LPG was chosen such that the 2DEG will be depleted below the gate which forms the resonator gate connected to the center conductor. This avoids for dissipative processes from the resonator gate into the 2DEG below (see section 6) and corresponds to a voltage regime for LPG that is typical for operating the dot in a single electron configuration.

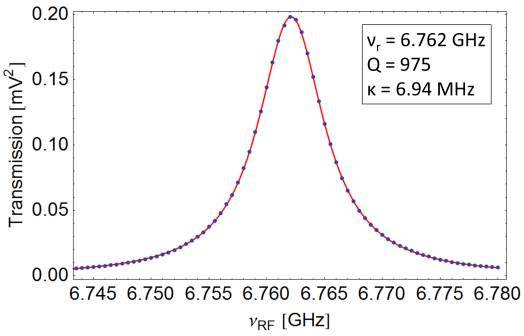

Figure 3: Squared resonator transmission amplitude and fit for all top-gates at 0 V, except for LPG = -450 mV (see text) and Appendix B [A1]

The squared transmitted amplitude has a Lorentzian line shape, given by equation

$$T(\nu_0) = y_0 + \frac{A}{1 + \frac{(\nu-\nu_0)^2}{\delta\nu_0^2}} \qquad (1)$$

where A describes the amplitude in mV^2, ν_0 the resonance frequency, y_0 a constant offset and $\delta\nu_0$ the linewidth of the peak. In such a parameter space, a quality factor Q = 975 respectively linewidth κ = 6.939 MHz was fitted. The Lorentzian shows a frequency ν_0 = 6.762 GHz, amplitude A = 0.2 mV^2 and offset y_0 = -0.00126 mV^2 derived from a line fit, shown by the red curve in Fig 3. The resonance frequency for the fundamental mode ν_0 is described by $\nu_0 = c/2l\sqrt{\epsilon_{eff}}$ respectively equivalently $2l = \lambda_0$ [25] where ϵ_{eff} gives an effective permittivity of the transmission line resonator, c is the speed of light in vacuum, l the resonator length and λ_0 the wavelength in the fundamental mode. An input power of -7 dBm was applied which corresponds to a mean photon number of 25.7, approximating a total attenuation of -106 dB down to the resonator and considering $\kappa = 6.939$ MHz in this measurement. It was experimentally verified that no non-linearities in the resonator transmission occurred at the chosen input power. All ohmic contacts were grounded in this measurement and all the following microwave measurements thereby grounding the 2DEG. It is found however that the characteristic resonator parameters such as transmission amplitude, resonance frequency and linewidth strongly depend on the gate configuration, which is discussed more detailed in section *6 Influences of 2DEG on resonator characteristics*. The extracted parameters can thus serve only as a first estimate and a unique characterization of the resonator is not possible.

2.3 Double quantum dot design for single electrons

A scanning electron microscope image of the employed DQD geometry is given in Figure 4. Note that the image shows a SEM photograph of a double dot that is similar in its design to the geometry used. No SEM image has been available yet for the currently used sample which is still being measured at this point. The sample was designed in some earlier work not by the author [24].

Eight top gates are used to form the lateral quantum dot, labeled by their abbreviation in Fig. 4. The quantum dot is formed by means of side gates (LSG, RSG). Source drain barrier (SDB) and the center gate (CG), separate the structure such that a double dot forms. Furthermore, SDB and CG have the benefit to control the coupling between the individual dots. The static potential of an individual dot can be additionally tuned via left plunger gate (LPG) for the left dot respectively right plunger gate (RPG) for the right dot. The CPW resonator is capacitively coupled via LPG to the left dot which is achieved by directly coupling an extension of the center conductor to LPG, as shown in Fig. 2b. If the length of the extension is short compared to the wavelength, the extension can be assumed to be on the same potential as the center conductor at the respective position

for all times, thus coupling a resonator excitation to the left quantum dot. An oscillating field at the antinode, below which the dot is positioned, results in voltage oscillations at the center conductor and equivalently at its extension which translates via a capacitive coupling to a variation of the static potential in the left dot in a classical description. The coupling between resonator and DQD is explained in section *4 Dipole coupling of a single electron to a microwave field*. The center conductor can be independently biased with a voltage source by means of an inductor shown in Fig. 2a. Besides the periodic voltage modulation on LPG, given by the oscillating field in the resonator, a constant voltage offset can thereby be added to LPG via biasing the center conductor, which translates to a changed static potential in the left dot.

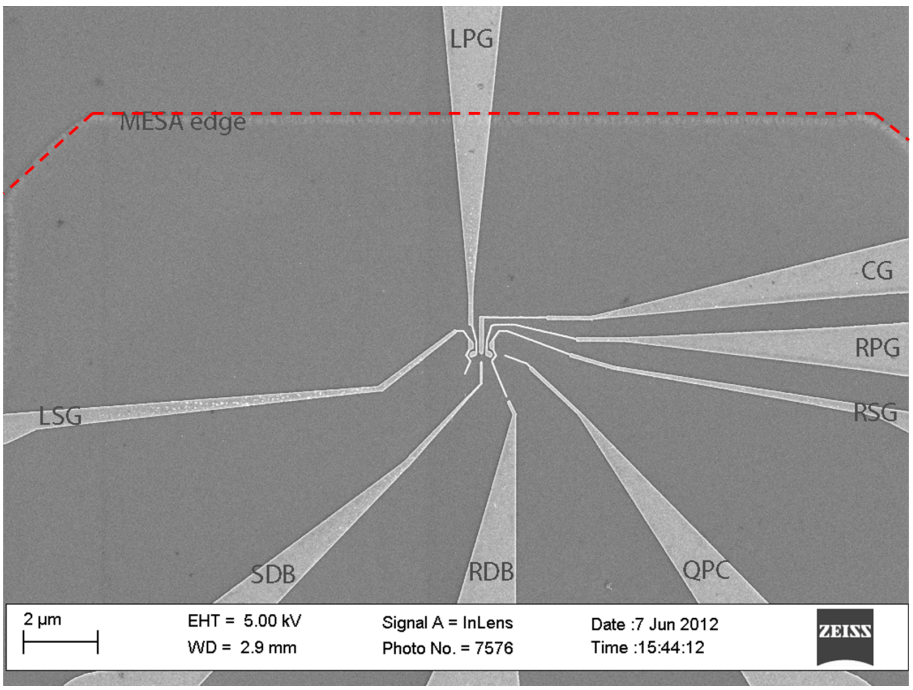

Figure 4: SEM image of the double dot design showing left plunger gate (LPG), center gate (CG), left side gate (LSG), right plunger gate (RPG), right side gate (RSG), quantum point contact (QPC), soure drain barrier (SDB) and right drain barrier (RDB). The mesa edge is indicated by the red dashed line. The picture shows a double quantum dot with similar design to the sample under investigation. No SEM picture of the currently measured dot is available at this point.

In addition RSG, and the gate labeled QPC form a quantum point contact that serves as an on-chip charge detector, first implemented by Field *et al.* [17]. The right drain barrier gate (RDB) is used to change between different DC channels, where appropriate. Also shown is the MESA edge, above which the 2DEG was etched away. A more detailed view of the DQD region is also available from Fig. 1b. Not shown are four ohmic contacts to access the 2DEG. Those are situated at both sides of the gates SDB and QPC to allow for DC and QPC measurements separately, explained in section *3 Transport and charge detection for a double quantum dot*. Also not shown is the coupling of the resonator to the resonator gate LPG. An extension of the center conductor translates voltage oscillations onto LPG and thereby through a capacitive coupling onto energy levels in the left quantum dot. Note that the right dot is not directly coupled to the resonator, but a finite cross-coupling of resonator gate (LPG) to right dot can not be avoided in such a mesoscopic structure.

3 Transport and charge detection for a double quantum dot

This section discusses electron transport in a DQD architecture in the linear and non-linear regime. The description of the transport phenomena follows [20, 26]. Experimental data for direct current and QPC measurements are presented and discussed for the few and many electron regime. Here and in the following, all experiments were carried out at a base temperature of about 10 mK in a dilution refrigerator. The electronic temperature T_e is higher and was estimated to be approximately 130 mK from thermal broadening. The exact value for T_e was not yet determined in the experiment. Transport measurements were carried out either measuring the direct current (DC) throught the double dot respectively QPC or by calculating the numerical derivative dI/dV_{PG} where dV_{PG} is the change in voltage at plunger gate PG. Alternatively, the transconductance through the QPC was measured. In such a measurement, an AC modulation with constant amplitude was added to the voltage applied at the plunger gate and the change in the current at the charge detector is measured, i.e. dI_{CD}/dV_{PG}. This has the benefit to incerase the detection sensitivity. Such measurements were carried out using a Stanford Research Systems SR830 DSP lock-in system. A small modulation of 10 μV was applied to the source-drain bias respectively 150 μV to the voltage applied at LPG for transconductance measurements with a modulation frequency of 75 Hz respectively 37 Hz, unless outlined differently.

3.1 Relevant energy scales and capacitance model

In a classical description, the DQD is modeled by a circuit of various resistors and capacitors [26] without considering quantum behavior. However, in a quantum description energy states become quantized in a strongly confining potential and further excited states enter the model additional to electron tunneling processes. The coupling to the leads can be taken into account by a small perturbation in this description. A schematic of a DQD circuit modeled in terms of resistors and capacitors is shown in Fig. 5 for the linear transport regime where no bias between source and drain is applied, i.e. the chemical potential of source and drain are equal. The description follows [18, 26]

In **Fig. 5a**, the individual dots are capacitively coupled only to their respective gates PG1 for Dot1 and PG2 for Dot2. Each dot is independently coupled to source or drain, modeled by a resistor and capacitor in parallel to account for the tunnel barrier. The interdot coupling in this model is purely resistive. In this notation, (N,M) indicates N electrons in the left dot and M electrons in the right dot. Energetic electrons with energy sufficient to overcome the resistive barrier and Coulomb repulsion, resulting from electron-electron interaction to electrons within the dot, can enter from source respectively drain into the dot and occupy empty states. The static dot potential can be tuned independently for Dot1 by voltage V_{PG1} and for Dot2 by V_{PG2}. Whenever an unoccupied state is in resonance with electrons of sufficiently large energy, a new electron can occupy a dot state and the occupation number changes e.g. from (N,M) to (N+1,M) for one additional electron in the left dot. Additionally, the dots are only resistively coupled such that the number of electrons in the left dot has no effect on the potential energy in the right dot and vice versa. However, an electrons might overcome the resistive barrier between both dots and Coulomb repulsion and changes the occupation number from e.g. (N,M) to (N-1, M+1).

Fig. 5b on the contrary models a cross-coupling respectively cross-capacitance between the plunger gates PG1 (PG2) and Dot2 (Dot1). Changing the applied voltage at PG1 not only tunes the static potential in Dot1, but also has a effect on the potential in Dot2. Conductance resonances, showing the coupling between dot and lead, become tilted.

In a more realistic description, a capacitive in addition to the resistive coupling between Dot1 and Dot2 is taken into account (cf. **Fig. 5c**). The number of electrons in Dot1 influence additionally the static potential in Dot2 and vice versa. That is, the electrostatic field of electrons in one dot changes the potential in the neighboring well. The static potential in left and right dot are degenerate along the green line that connects two triple points (red), whereas the mean potential changes along the line from resonant with source and drain at one triple point to off-resonant along the line and on-resonant again at the second triple point for a different charge configuration (cf. also Fig. 6). This region in LPG-RPG subspace is commonly referred to as interdot charge transfer line or charge degeneracy line (green line in Fig. 5c). A derivation of the DQD electrostatics is given in [18, 26]. Energy states within a quantum dot are due to an interplay of various effects:

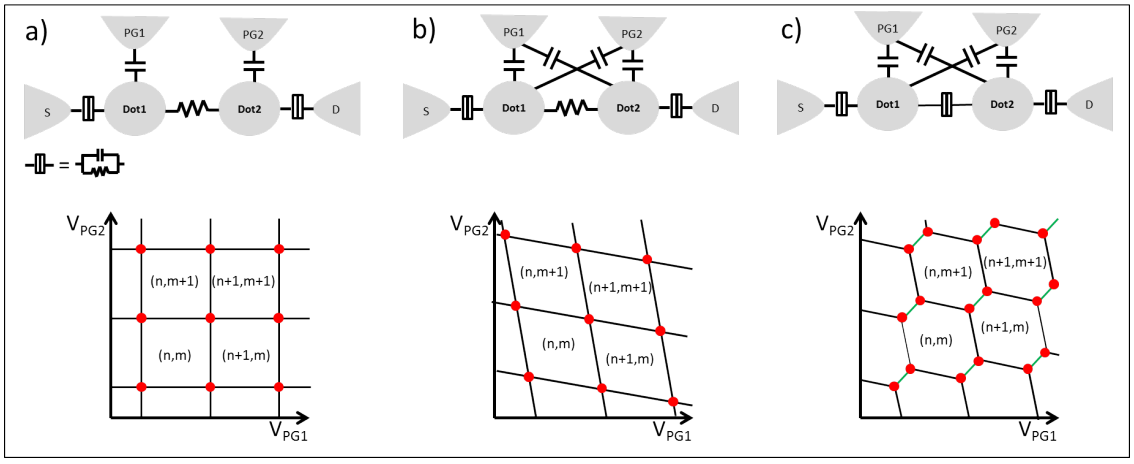

Figure 5: DQD modeled as a circuit of resistors and capacitors with corresponding charge stability diagrams, assuming resistive coupling between both dots (a), resistively coupled dots and cross-coupling to capacitively coupled plunger gates (b), resistive and capacitive interdot coupling (c) (see text). Figure similar to [27].

Coulomb interaction energy: The Coulomb interaction energy between electrons can be estimated from the electrostatic island energy, following [18]. Modelling a single quantum dot as metallic disk with self-capacitance C, $E_{electro}(N) = \frac{e^2N^2}{2C}$, where e is the electric charge and N the number of electrons. The energy necessary to add one additional electron, assuming that N electrons occupy the dot, is $E_c(N+1) = E_{electro}(N+1) - E_{electro}(N) = \frac{e^2}{C}(N+1/2) \simeq \frac{e^2N}{C}$. The difference $\Delta E_c = E_c(N+1) - E_c(N) = e^2/C$ is tradionally used, often named charging energy. An estimate following [18] gives a typical charging energy of $\Delta E_c \simeq 1.7$ meV, assuming the self-capacitance of a disk $C = 8\epsilon\epsilon_0 r$ with radius $r = 100$ nm, a size typical for quantum dots, and a dielectric constant $\epsilon = 13$ typical for GaAs. However, in the case of two coupled quantum dots, the charging energy changes. Following [26], $\Delta E_{C_{1(2)}} = \frac{e^2}{C1}(\frac{1}{1-C_m^2/C_1C_2})$ with $C_{1(2)}$ the sum of all capacitances attached to Dot1 (Dot2) and C_m accounts for the capacitive coupling between both dots. Additionally, an electrostatic coupling energy $\Delta E_m = \frac{e^2}{C_m}(\frac{1}{C_1C_2/C_m^2-1})$ enters that accounts for the capacitive coupling between both dots.

Confinement energy: Following [18], an approximation of the confinement respectively quantization energy in a single quantum dot is given by $E_{conf}(N) = \frac{\hbar^2}{2m^* r^2} N^2$, with m^* the effective electron mass, r the dot radius and N the number of electrons. From this expression, the energy necessary to add one additional electron is $\epsilon(N+1) = E_{conf}(N+1) - E_{conf}(N) = \frac{\hbar^2}{2m^* r^2}(2N+1)$ and therefore the spacing between adjacent levels $\Delta = \epsilon(N+1) - \epsilon(N) = \frac{\hbar^2}{m^* r^2}$, what is often termed single-particle level spacing. An estimate for GaAs gives $\Delta \simeq 110\ \mu$eV for a dot of radius $r = 100$ nm. Energetic states of quantization energy form excited states in a quantum dot whereby the spacing between adjacent excited states respectively ground and first excited state scales like $1/r^2$.

3.2 Transport in the linear regime

Diagrams that are shown in Fig. 5 are called charge stability diagrams and state the number of electrons (N,M) as a function of the plunger gate voltages V_{PG1} and V_{PG2}. In regions indicated by (N,M), transport is blocked as a result of Coulomb repulsion from electrons already occupying states in the dot, thus no additional electrons can enter the quantum dot. The description of blocked transport is known also as Coulomb blockade [28]. However, when decreasing the static potential in the dots by adjusting the applied voltage V_{PG1} or V_{PG2}, energy levels eventually become degenerate with a lead and additional electrons can enter the dot elastically. At the edges of the honeycomb lattice, where three charge states are degenerate (red points in Fig. 5), electrons can tunnel through the entire double dot from source to drain and a current is observable in the case of applied bias between both reservoirs. Please refer to [26] for more information.

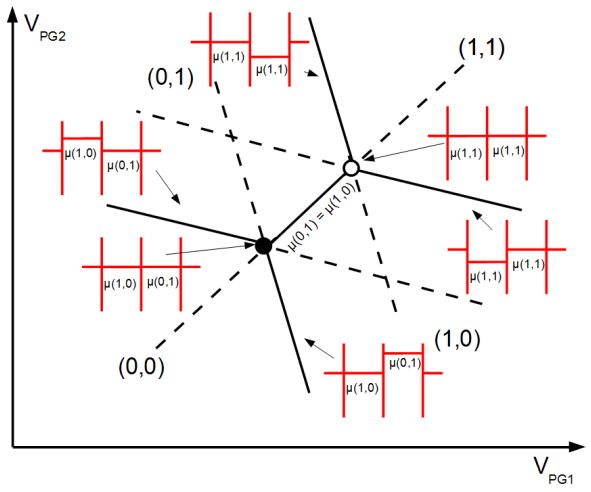

Figure 6: Quantum dot states at or close to the interdot charge degeneracy line. Direct current flow is possible at triple points where three charge states are degenerate, co-tunneling processes are shown for a dot configuration where the charge state of one dot is degenerate with the lead while the remaining stays off-resonant, Adopted from [26]

Fig. 6 gives a detailed view on this regime where the electrochemical potential of Dot1 $\mu_1(N_1, N_2)$ is the energy needed to add electron N_1 to Dot1 when already N_2 electrons occupy Dot2. In a quantum description, $\mu_1(N_1, N_2)$ is the sum of a classical electrochemical potential and the quantization energy E_n. Note that linear transport through the dot is only possible at the triple points where all energy levels are degenerate. However, co-tunneling processes are possible at regions where a dot state is resonant with its neighboring lead but the energy state of the remaining dot is off-resonant [26]. DC transport is possible in such a region, which corresponds to higher order processes in quantum mechanics when calculating the transition matrix elements. In general, tunnel barriers need to be sufficiently transparent to ensure electron transport but at the same time opaque to allow for discrete electrons tunneling only [26]. The setup allows to detect currents as small as 5 fA

in direct current measurements. Complementary, a QPC can be used to image charge states.

The current through a quantum point contact, positioned close to the double quantum dot, is sensitive to changes in the number of electrons in the individual dots. When operating such a device at the transition between quantized conductance pleateaus, the QPC conductance responds sensitively to changes in the electrostatic potential in its vicinity [18]. A change in occupation number of a dot comes along with a change of electrostatic potential at the QPC. Measured between conductance plateaus, the QPC thus serves as an instrument to image charge states of individual dots. Please refer to [29] for a more comprehensive description on quantum point contacts. Fig. 7 shows a direct current (Fig. 7a) measurement as well as a measurement of the transconductance through a quantum point contact (Fig. 7b) in the few electron regime. Note that the dot is completely emptied from electrons in the Coulomb blockade region at the bottom-left corner where no additional conductance resonances are visible (cf. Fig. 7b). It is important here to note that no direct current was observable for the last electron whereas the QPC measurement stays sensitive in this regime. A QPC serves as an essential tool when forming a single electron double quantum dot and especially to verify the dot regime in terms of electron number in our measurements.

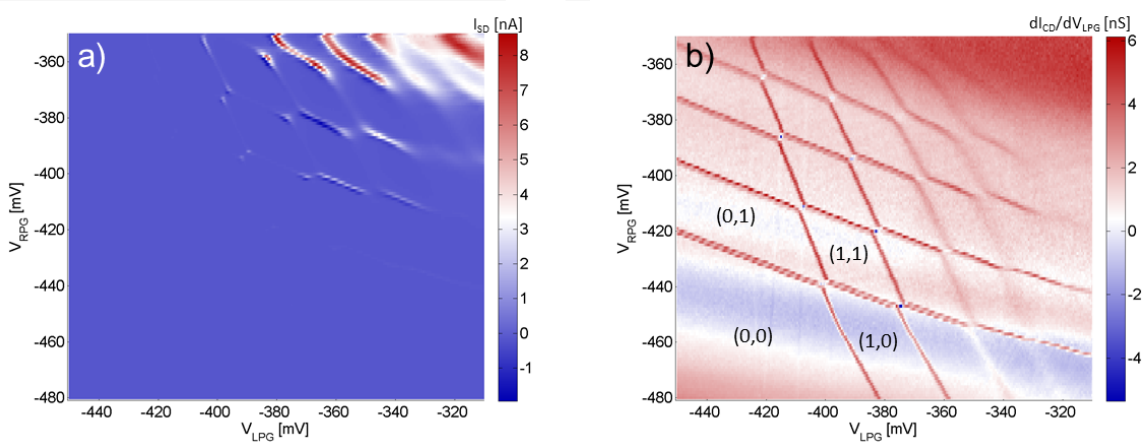

Figure 7: Charge stability diagram in close proximity of the last electron configuration: a) Direct current measurement in LPG-RPG subspace. The plot shows a false-color image of the measured current flow from source to drain, b) QPC measurement in LPG-RPG subspace. The plot shows a false-color image of the transconductance dI_{CD}/dV_{LPG} whereas dV_{LPG} indicates a small voltage oscillation of amplitude 100 μV applied to the left plunger gate, using standard Lock-In techniques. Refer to Appendix B [A2] for a full set of parameters.

A small bias of 25 μV was applied between source and drain for a directional electron transport through the DQD. It was checked that non-linear transport phenomena such as finite-bias triangles at triple points, which are an indication for a finite bias regime [26], were not observed. Additionally, a bias of 300 μV was applied between both sides of the QPC. Please refer to Appendix B [A2] for a list of applied top-gate voltages.

A careful analysis of the transport properties in the few electron regime, based on the measurement shown in Fig. 7, illustrates that by emptying the dot a possibly resulting small tunnel or co-tunnel current can not be resolved in DC measurement for the Coulomb blockade region with one electron in each dot only. The measured current vanishes when

biasing the left and right plunger gate sufficiently negative which is necessary to empty both dots. This suggests that the plunger gates not only change the static potential in the dots, but also have an effect on the tunnel barriers, either between the dots or from dot to lead. However, a full charge stability diagram is visible in a QPC measurement, even when tunneling rates are so small that no direct current is observable. The DQD is completely emptied in the region shown bottom-left in Fig. 7, no additional conductance resonances are measured. The region up-right in Fig. 7 shows a strongly tunnel coupled DQD. The conductance at triple points is seen to be rounded, caused by tunnel broadening between the individual dots [26]. In such a region, the two separated dots behave increasingly as a single large dot what can be observed by the strong DC current in this region (cf. Fig. 7a). Note that the tunnel coupling from dot to lead can be controlled additionally via the respective side gate voltage or the voltage applied to the source drain barrier SDB. Similarly, the interdot coupling can be controlled by changing the voltage applied to the center gate CG respectively to SDB. Thus, by increasing tunneling rates it might be possible to observe direct current through the dot in principle at the corners of the (1,1) Coulomb-Blockade region. However, it was not yet possible in the experiment to tune the DQD to a region in parameter space where a finite DC current was measured what suggests strong effects of both plunger gates on tunnel barriers.

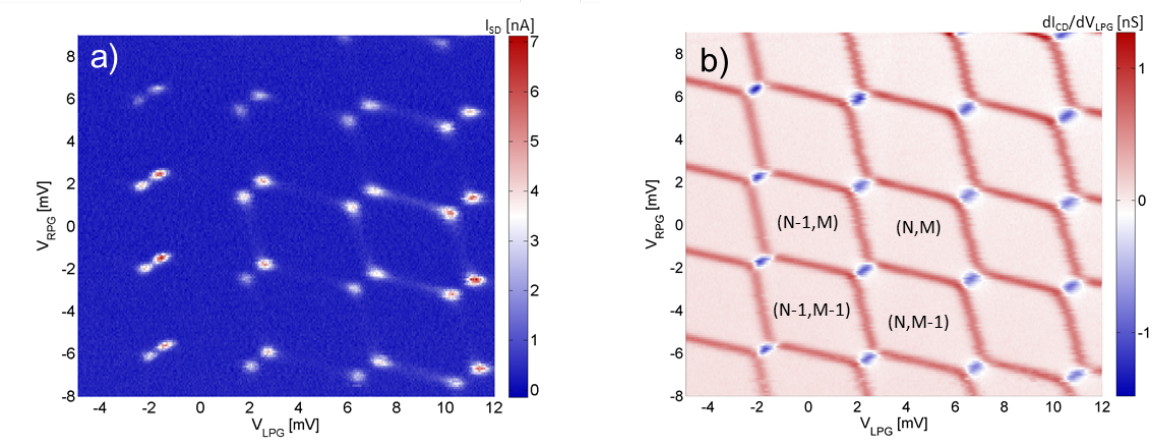

Figure 8: a) Direct current measurement in LPG-RPG subspace. The plot shows a false-color image of the measured current flow from source to drain, b) QPC measurement in LPG-RPG subspace. The plot shows a false-color image of the transconductance dI_{CD}/dV_{LPG} whereas dV_{LPG} indicates a small voltage oscillation of amplitude 100 μV applied to the left plunger gate using standard Lock-In techniques. Refer to Appendix B [A3] for a full set of all parameters.

On the contrary to the single electron regime, a strong DC current can be measured over many Coulomb blockade hexagons in the many electron regime, whereby both plunger gates are set less negative in voltage. Fig. 8 shows a DC and transconductance measurement for the DQD in the many electron regime. Please refer to Appendix B [A3] for all applied gate voltages. Direct current is most pronounced at triple points where three charge states are degenerate and a direct transport of electrons from source to drain is possible. However, co-tunneling lines are slightly visible at the edges of the honeycomb lattice that surround a Coulomb blockade region.

Such measurements give information not only on the dot regime but also allow to estimate the interdot tunnel coupling which becomes important when coupling the DQD to a resonator. Following DiCarlo *et al.* [30], the interdot tunneling t can be investigated from

the width of the charge degeneracy line (blue line in charge detection, Fig. 8b).

3.3 Transport in the non-linear regime

In the non-linear transport regime, a finite bias is applied between source and drain such that a bias window opens in which electron transport is possible for different quantum state configurations [26]. Triple points, at which direct current is measured, extend to triangular shaped regions in LPG-RPG subspace. For spectra with sufficiently separated energy states, even excited states can contribute to the conductance. Such a transport measurement can be used to estimate the lever arms of a plunger gate on left and right dot i.e. the translation factor from applied gate voltage to a change in the static potential energy in the dot. Lever arms $\alpha_{LPG(RPG)}$ for the left (right) dot translate the applied bias by equation [26]

$$\alpha_{LPG(RPG)}\delta V_{LPG(RPG)} = |eV| \tag{2}$$

where V denotes the applied source-drain bias, e the electron charge and $\delta V_{PG1(PG2)}$ is the projective view of the triangle dimensions on the applied plunger voltage for PG1 (PG2) (cf. Fig. 9). Note that this equation is only approximative and takes no cross-coupling between gates into account. Please refer to [31] for a full description with included cross-coupling.

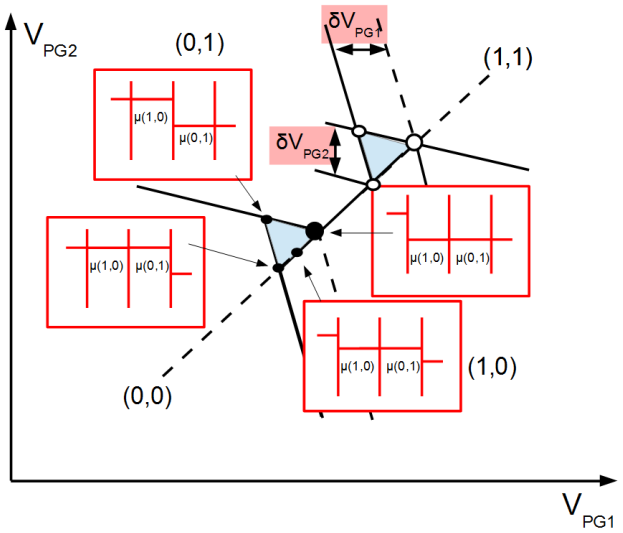

Figure 9: Finite bias triangles: Triple points (large black (white) circles show electron (hole) transport) evolve to triangles (light blue) where resonant DC transport is possible along the boundary. A finite current can be measured within triangles (light blue) due to co-tunneling and further inelastic tunneling processes. Figure similar to [26]

Following [26], the extraction of lever arms is best described by Fig. 9 and employed to a set of experimental data in the few electron regime in Fig. 10a. The data corresponds to a finite bias measurement with a potential difference of 400 μV between source and drain. It was experimentally checked that triangles are most pronounced for this bias setting, although the shown triangles might serve only as an estimate due to uncertainties given by tunnel and temperature broadened coupling to leads and incompletely developed

triangles, that were extracted from our measurement. A mean lever arm of $\alpha_{LPG} = 0.11$ eV/V resp. $\alpha_{RPG} = 0.12$ eV/V was calculated for the left and right dot from the left and right triangle. Note that, although both triangles shall be equal in size by theory, a clear discrepancy between both triangles can be seen what additionally adds to an estimated overall uncertainty of $\pm$ 0.04 eV/V. An accurate estimation of the lever arm is essential for an exact energy calibration which remains an open question for the few electron regime. Alternative methods such as RF-Spectroscopy (cf. e.g. [32, 33]) might lead to higher accuracy. Such an experiment is planned for the future and not yet included in this work.

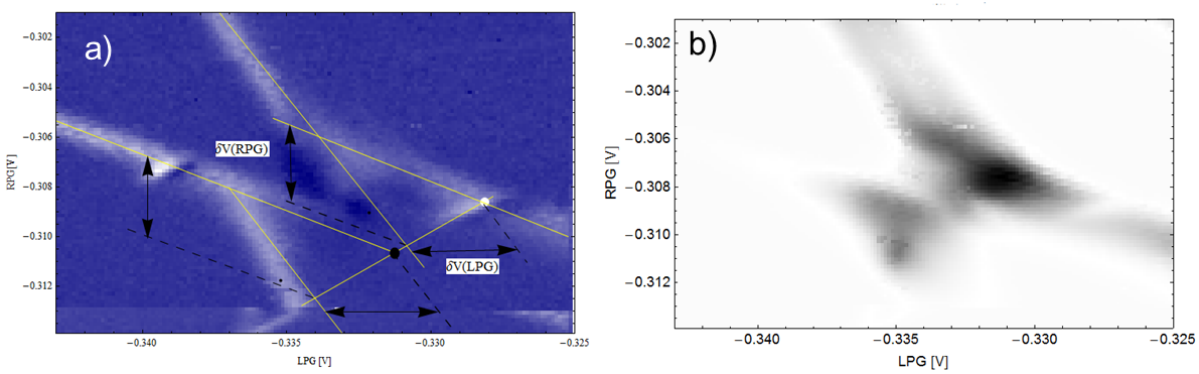

Figure 10: Experimentally measured finite bias triangles in transconductance (a) and direct source-drain current (b) for a few electron DQD. A possible choice of triangles is shown by the yellow lines, while black arrows show a projection of the triangle size on the axes for LPG and RPG. By its projection, finite bias triangles allow to determine energy scales in the system.

3.4 Evidence of a single electron double quantum dot in charge detection

From a DC respectively transconductance measurement, there is evidence to conclude on the number of electrons within a double quantum dot. Fig. 11 compares a QPC transconductance measurement for a many (Fig. 11a) and few (Fig. 11b) electron regime. A summary of various steps to build up the dot is given in Appendix A, while a set of all gate voltages applied is stated in Appendix B [A2, A3] for both configurations. The two configurations are different in terms of charging energy ΔE_c, lever arm α and conductances:

Charging Energy: A comparison of charging energies in both charge stability diagrams shows an increase in the few electron regime. Based on an estimate following van der Wiel *et al.* [26], an approximative charging energy of $E_{c-left} \simeq 2.9$ meV and $E_{c-right} \simeq 3.4$ meV for left respectively right dot was calculated in the few electron regime while $E_{c-left(right)} \simeq 1.0$ meV in the many electron regime. The charging energy of left (right) dot vary due to different sizes, given by fabrication and applied gate voltages. This can be understood from the relevant energy scales (cf. section 3.2). A few electron quantum dot is usually smaller in size r which results in a higher charging energy ΔE_c. From the charging energies, an approximative dot size of $r_{left} = 60$ nm ($r_{right} = 51$ nm) in the single and r = 174 nm in the many electron regime can be estimated. Note that the estimate was done for a single quantum dot only, i.e. not the tunnel coupled system but nevertheless serves as an approximation.

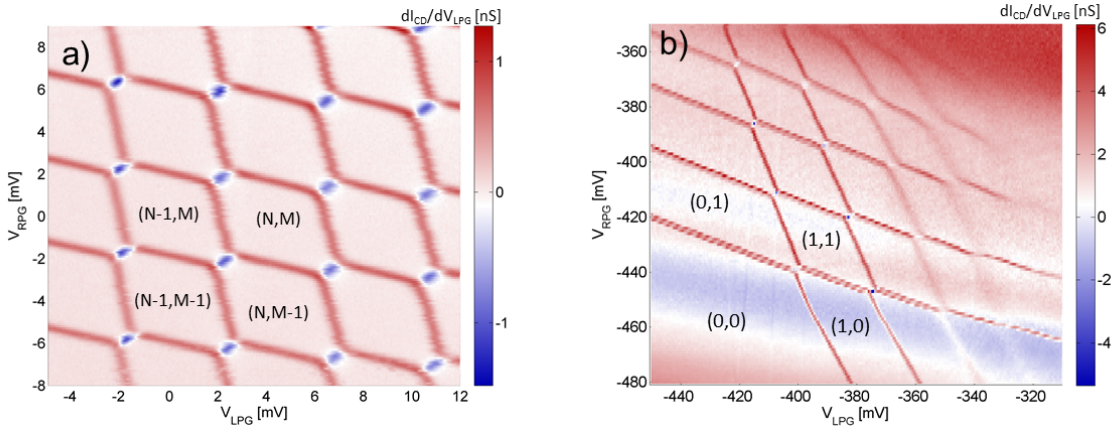

Figure 11: QPC Transconductance measurement: a) Many electron regime, b) few electron regime. There are significant differences in the charge stability diagrams with respect to lever arm α, charging energy E_c and conductance resonance (see text). Please refer to Appendix B [A3] (a) and [A2] (b) for a full set of parameters

Lever arm: The lever arm for plunger gates acting on the individual dots is expected to decrease for a few electron quantum dot, given the fact that a quantum dot with less electrons is assumed to be smaller in size. This leads to a decreased capacitive coupling between gate and dot and thereby a smaller lever arm, in comparison to the many electron regime. Indeed, a lever arm $\alpha_{left} = 0.11$ eV/V for the left and $\alpha_{right} = 0.12$ eV/V for the right quantum dot was experimentally measured in the few electron regime. This was supplemented by $\alpha_{left} = 0.23$ eV/V respectively $\alpha_{right} = 0.23$ eV/V in the many electron quantum dot.

Conductance: No conductance resonances are visible in a region where the dot is completely emptied (cf. Fig. 11b, lower-left). Energetic levels are higher in energy than the source and drain potential such that no electrons can enter the dot. The static potential is further increased for more negative plunger gate voltages $V_{LPG(RPG)}$ and no electrons enter. The dot and thereby the quantum point contact stays unaffected and no resonances are visible in this regime.

No direct current: No direct current through the dot respectively no differential conductances are measurable in the single electron regime (cf. Fig. 7a and 8a) while only the QPC transconductance measurement stays sensitive. This is understood from the voltage applied to the plunger gates. Emptying the dot requires strongly negatively biased plunger gates. In the current sample, plunger gates not only influence the static potential in the dot but also affect tunnel rates to the lead as well as interdot tunneling. A strongly negative plunger gate reduces electron transport through the dot accordingly to a point at which the direct current and differential conductance measurement is not sensitive. The QPC however stays unaffected, as the detector is sensitive to changes in the number of electrons within the dot.

4 Dipole coupling of a single electron to a microwave field

A direct coupling of a quantum dot to a microwave resonator has the potential advantage to measure charge and spin states without the necessity for an additional mesoscopic detector such as a QPC, and thereby better decoupling the qubit from its environment and e.g. from measurement back-action such as radiation generated by the QPC (cf. e.g. [34]). Although a QPC is included in the current sample design, the device can be decoupled by setting the respective gate forming the QPC to zero volt respectively the applied bias voltage. Complementary, the resonator serves as a non-invasive tool to read the quantum dot [16]. This section intends to discuss a DQD in terms of a qubit and its coupling to a resonator.

4.1 Double quantum dot as a charge qubit

A single electron DQD can be modeled as a charge qubit in which an electron occupies the ground state of either the left or the right dot [16, 18]. Starting with both dots initially not tunnel coupled to each other, the Hamiltonian that describes the configuration is given in the basis of charge states $|0,1>$ ($|1,0>$) by

$$\hat{H}_0 = \frac{1}{2} h\delta\hat{\sigma}_z \tag{3}$$

where $\hat{\sigma_z}$ is defined by by $\hat{\sigma}_z = |0,1><0,1| - |1,0><1,0|$ and $|0,1>$ ($|1,0>$) denotes the state of an electron occupying the right (left) dot. The energy difference between both states is given by $h\delta$. Fig. 12a shows a schematic of the two ground state energy levels and the dot either in state $|1,0>$ or $|0,1>$. The chemical potential of the left source (S) and right drain (D) are labeled. In this configuration, both dots are separated by a sufficiently large potential such that electrons do not tunnel between either side of the DQD. In a second step, electrons are allowed to tunnel through the central barrier (Fig 11b). This can be described by an additional term that describes the interaction between both dots [16]:

$$\hat{H}_I = ht\hat{\sigma_x} \tag{4}$$

and adds to the Hamiltonian given in (3) to an overall Hamiltonian which describes a tunnel coupled DQD with $\hat{\sigma_x} = |1,0><0,1| + |0,1><1,0|$. This interaction Hamiltonian accounts for a transition between both dots with tunnel coupling t. Additionally, the interdot tunnel coupling mixes charge states, which leads to a superposition of the electron states left and right dot. The interdot coupling hybridizes states close to zero detuning δ which is observable by a tunnel splitting, schematically shown in Fig. 13b.

The new eigenstates are given by a symmetric and antisymmetric superposition $|\Psi_\pm>$ of the uncoupled states with eigenenergies $E_\pm = \pm\frac{1}{2}h\sqrt{\delta^2 + (2t)^2}$. Those two states $|\Psi_\pm>$ form the basis of a new Hilbert space that can be used to describe the ground and excited state of a qubit. The transition frequency between both states is given by $\Omega = \sqrt{\delta^2 + (2t)^2}$ with a minimal transition frequency of 2t for zero detuning δ. A schematic of bare and hybridized states is shown in Fig. 12.

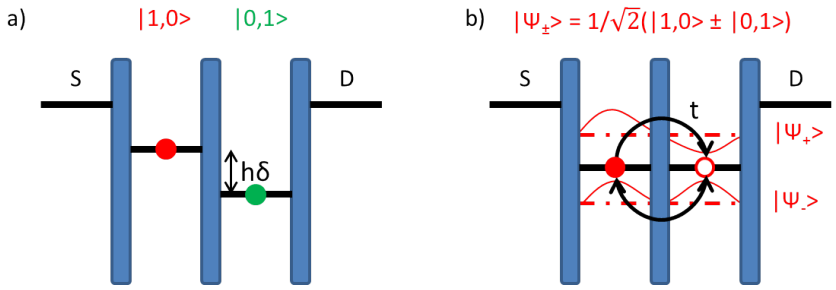

Figure 12: Ground state energy levels of a DQD: a) Individual quantum dot states if not tunnel coupled, b) quantum dots are tunnel coupled and charge states become delocalized between both dots. A bonding (lower dashed red line) and antibonding state (upper dashed red line) form as new eigenstates of the coupled system.

Figure 13: Uncoupled quantum dot energy states (a) and hybridized states (b) as a function of the detuning δ between energy levels of the left and right dot

4.2 Quantum capacitance, tunnel resistivity and DQD admittance

The tunnel process of an electron between both dots and the involved motion of the electron allows to introduce the concept of a change in polarizability. By a tunnel process of an electron into one dot, the electron density changes, which goes along with a change in the potential confining the dot. The potential becomes steeper and the quantization energy rises which changes the width and center of mass of the ground state wave function in the respective dot [20]. This leads to a change in polarization and therefore to a change in AC susceptibility $\mathcal{X}$. The susceptibility depends on the strength of tunneling t and is maximal for zero detuning [10]. A schematic is given in Fig. 14.

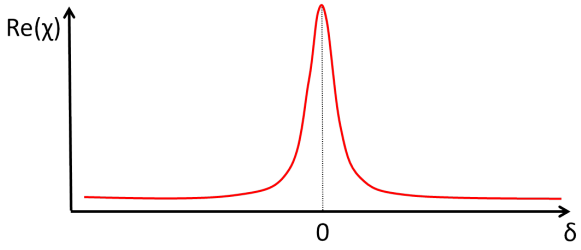

Figure 14: The change in the AC susceptibility Re($\mathcal{X}$) is maximal for zero detuning. Adopted from [10]

A similar description is given by an effective capacitance, defined by the derivative of induced charge with respect to gate voltage. The effective capacitance comprises a geometric capacitance C_{geom} and the quantum capacitance C_Q, that is due to an anticrossing at the degeneracy point [35].The quantum capacitance for a charge qubit is a function of the band curvature which leads to different capacitances for the respective qubit ground and excited state. Following [16], C_Q can be described by

$$C_Q^{\pm} = -(e\kappa)^2 \frac{\partial^2 E_{\pm}}{\partial^2 \delta} \tag{5}$$

where κ is a conversion factor between applied gate voltage V_g and change in level detuning $\Delta\delta$, i.e. $\Delta\delta$ = -e$\kappa\Delta V_g$ and $E_{\pm}$ define bonding (antibonding) state [16, 35]. C_Q is maximal at extrema in curvature i.e. for δ equal zero. A schematic is shown in Fig. 15.

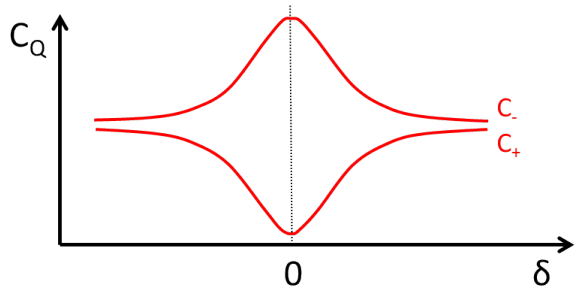

Figure 15: Quantum capacitance of a DQD for two different states. Adopted from [16]

The quantum capacitance C_Q can be probed by coupling a resonant circuit to the double dot. The additional capacitance changes the effective resonator capacitance and therefore the resonator resonance frequency [16]. By means of C_Q, a qubit can be modeled as a nonlinear quantum system with a capacitance that depends on the respective qubit state [5]. A description in terms of quantum capacitance is valid only in the dispersive regime, where cavity and qubit transition frequency are largely detuned i.e. $g^2/\Delta \ll 1$ where g describes the coupling of qubit to resonator and Δ the detuning between resonator and qubit transition frequency. For a full description, the tunnel resistivity enters additionally [36]. A lumped element representation of the circuit that describes the coupled qubit resonator system is given in Fig. 16 (cf. [14, 25]). The resonator is coupled capacitively (C_κ) to input and output lines. R_L gives an additional resistive load. The LCR-Circuit that describes the transmission line resonator close to resonance is highlighted by the red box. Additional information for coplanar waveguide resonators can be accessed via [25]. A qubit that is coupled to a resonator gives an additional contribution due to its tunnel resistivity R_{tunnel} and effective capacitance $C_{eff} = C_{geom} + C_Q$. A lumped element circuit for the DQD is denoted by the green box in Fig. 16. A coupled double quantum dot induces a dispersive frequency shift (changed C_Q) and possibly dissipation in the resonator (losses e.g. due to non-resonant tunneling) which can be probed by a microwave tone.

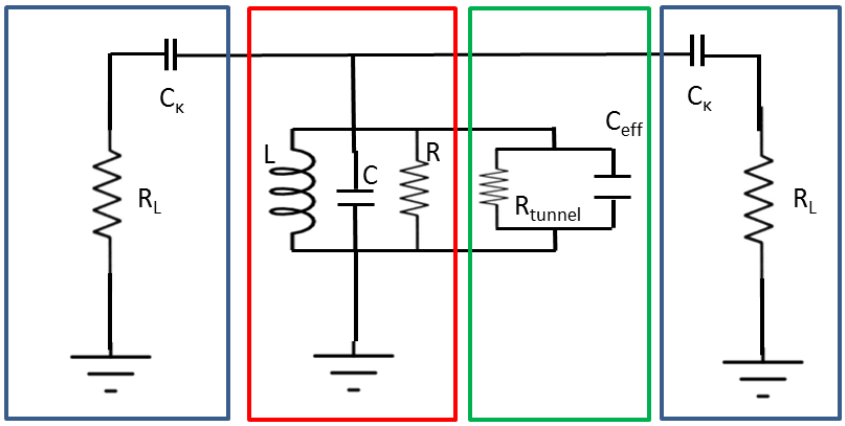

Figure 16: Coupled resonator-DQD system represented as electric circuit. A state dependent effective capacitance C_{eff} of the DQD (green) changes the resonator (red) resonance frequency

However, experimental data together with theoretical concepts suggest that besides capacitive effects, inductive behavior enters the reactance and therefore influences the admittance X of a mesoscopic system differently, in addition to purely resistive effects described by the real part of the complex impedance Z. The admittance is defined as X = 1/Z in this context. This can be described quite intuitively following Frey *et al.* [14]. As the tunneling rate between dots or dot and lead decreases, the electron can not follow the drive field anymore when the dwell time exceeds the field period. A current defined by the tunneling electron lacks behind the field respectively the applied voltage. The overall response of current to voltage shows more and more inductive behavior. This will be visible measuring the resulting frequency shift of the resonator, as capacitive reactance and inductive reactance show opposite sign and therefore influence the resonance shift in the resonator in opposite direction. Such a system can be modeled in terms of the dynamic admittance $g^{QD}(\omega)$, that describes the tunnel coupled quantum dots [14].

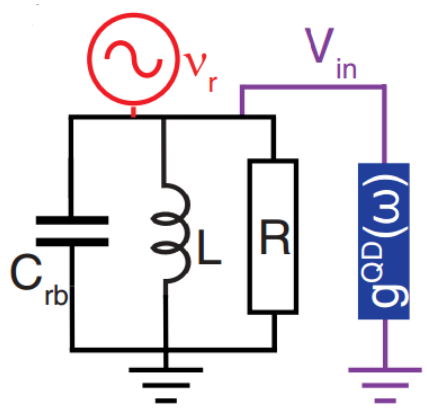

Figure 17: Lumped element diagram of Resonator-DQD system. The dot is represented by its dynamic admittance $g^{QD}(\omega)$ coupled to a resonator (LCR-circuit), adopted from [14]

A lumped element description is shown in Fig. 17, following Frey *et al.* [14]. Here, the DQD is modeled in terms of its dynamic admittance $g^{QD}(\omega)$. The dot is connected in parallel to an LRC-circuit that serves as a model for the coupled transmission line resonator whereas excitations in the resonator translate via V_{in} on the dot. The resonator is driven at its resonance frequency ν_r. However, the resonance frequency of the coupled quantum-dot resonator system shows a frequency shift in comparison to the bare resonator frequency that depends on the complex admittance. This fact can be used to read out the qubit state or the DQD characteristics in a transmission measurement. Probing the resonator at its bare resonance frequency ν_r, the amplitude of the transmitted signal decreases when the resonator frequency shifts. This model was proposed by Frey *et al.* [14] for the tunnel process between dot and lead in and remains to be investigated for the interdot tunneling.

In a Coulomb blockade region, the energy of the dot is dominated by the charging energy E_c which is two orders of magnitude higher than the photon energy in the transmission line at resonance, given a charging energy of around 1 meV respectively 240 GHz which is typical for lateral defined semiconductor quantum dots. The cavity is unaffected by the presence of a DQD respectively by a change in the dynamic admittance $g^{QD}(\omega)$. However, near a charge transition line, i.e. for the interdot detuning δ approaching zero, energy scales are of similar size which leads to an observable frequency shift when the admittance of the DQD is influenced by excitations in the resonator. This can be understood as a change of the electron wavefunction, resulting from resonator excitations, which is equivalent to a change in the polarization of the DQD. Additionally, dissipative processes might contribute, given by the real part of the complex impedance, although those are not yet completely understood. Frey *et al.* speculate that charge relaxation processes have a major effect in high-frequency resistance measurements [14]. Presented work by Gabelli *et al.* [37] shows a similar effect in a quantum RC circuit.

4.3 Quantum mechanical treatment

A quantum mechanical treatment of a coherently coupled resonator-DQD system in the following closely follows ideas developed by Childress, Sorensen and Lukin [38]. The coupling between both systems relies on a capacitive interaction between a quantized resonator excitation and the electron charge within the DQD. Deviating from [38], a finite cross-coupling was introduced to account for the experimentally observed situation. In such a description, mesoscopic systems separated in space might be coherently coupled for quantum information processing, provided that strong coupling between resonator excitations and charge qubit exists. The basic idea is outlined in Fig. 18.

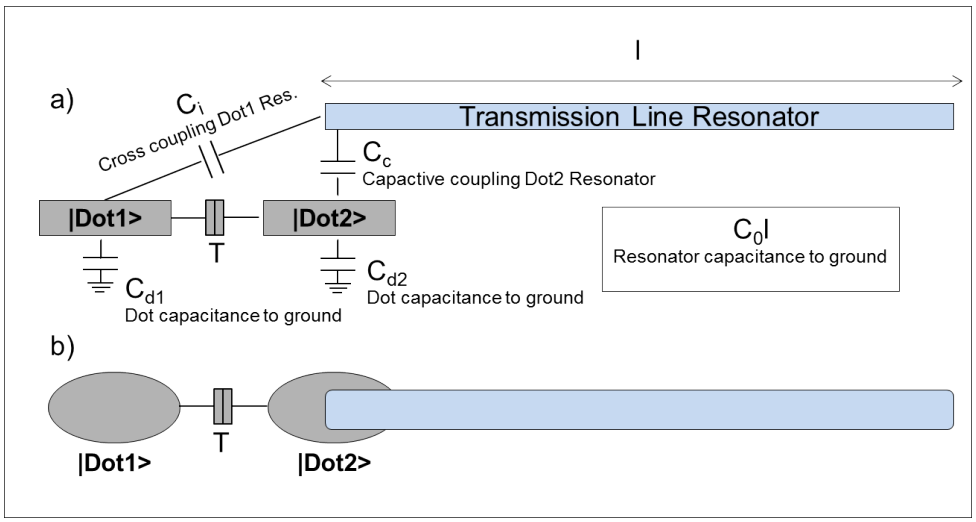

Figure 18: Schematic of a quantum dot capacitively coupled to a transmission line resonator and tunnel coupled to its neighboring quantum dot, side view (a) and top view (b). Concept and figure similar to [38]. Deviating from this publication, the cross capacitance C_i was introduced to account for the experimentally relevant situation.

The DQD is described in terms of a single electron which occupies a charge state either in the left $|Dot1>$ or right $|Dot2>$, for both dots initially not tunnel coupled. When a finite coupling is switched on, the electron wavefunction becomes displaced between both dots and bare charge states $|Dot1>$ and $|Dot2>$ hybridize, described previously section 4.1. Additionally to this system, a transmission line resonator is capacitively coupled with strength C_c to the right quantum dot and with capacitance C_i to the left dot. Quantized excitations in the resonator change the static potential in the right and left dot to a different extend as a reason of a different capacitive couplings. The electron charge interacts with resonator photons via such a process. Changing the static potential predominantly in one of the coupled dots changes the electron wavefunction and therefore the effective dipole moment. In the following, it is shown that such an interaction is equivalent to a dipole coupling between resonator and DQD and formally analogous to cavity quantum electrodynamics with atoms [38].

In the limit of a dot that is much smaller in size than the wavelength of the radiation, which is well fulfilled in the case of microwave radiation where the wavelength (mm) is orders of magnitude larger than the dot size (nm), the interaction strength can be described in terms of the electrostatic potential energy of the coupled system [38]. In this derivation, it is assumed that the resonator is predominantly coupled to the right dot whereas a cross coupling to the left dot is neglected for simplicity.

$$\hat{H}_{int} = e\hat{V}c|Dot2 >< Dot2| \tag{6}$$

where $|Dot2><Dot2|$ describes the coupling to the right dot, e is the electronic charge, $\hat{V}$ the voltage of a field excitation at the position of the right dot i.e. the potential of the center conductor at the dot position, $c = C_c/(C_c + C_{d1})$ with C_c the capacitive coupling of the right dot to resonator and C_{d1} the capacitance of the right dot to ground. In the case of a finite cross coupling, c needs to be reduces to $c = C_c/(C_c + C_{d1}) - C_i/(C_i + C_{d2})$ as only a difference in coupling strength changes the polarization. Note that an identical capacitive coupling gives a common oscillation in energy in both dots, when coupled to resonator excitations, and thereby does not change the dipole moment. The constant offset in both dots changes the overall energy while only the difference in induced energy shifts accounts for the dipole coupling. A strong dipole coupling can thus be achieved by increasing the capacitive coupling to the right dot and minimizing the cross coupling between resonator and left dot. Rewriting the interaction Hamiltonian in terms of DQD eigenstates

$$|+ >= sin(\Phi)|Dot1 > +cos(\Phi)|Dot2 > \tag{7}$$

$$|- >= cos(\Phi)|Dot1 > -sin(\Phi)|Dot2 > \tag{8}$$

In this description $tan(\Phi) = -2t/(\Omega + \delta)$ and $\Omega = \sqrt{(2t)^2 + \delta^2}$. Ω describes the qubit transition frequency i.e. the energy splitting between bonding and antibonding state of the tunnel coupled DQD, t is the matrix element that models the tunnel coupling between both dots and δ is the detuning between the respective dot charge states. Rewriting equation (6) in terms of raising and lowering operators of the qubit state $\sigma^+ = |+ >< -|$ and $\sigma^- = |- >< +|$ and introducing quantized resonator excitations,

$$\hat{V} = \sum_n \sqrt{\frac{h\nu_n}{lC_0}}(\hat{a}_n + \hat{a}_n^\dagger) \tag{9}$$

where ν_n describes the frequency of mode n, $\hat{a}_n$, $\hat{a}_n^\dagger$ are creation and annihilation operators from a canonical quantization of the resonator field obeying the bosonic commutation relation $[\ \hat{a}_n,\ \hat{a}_m^\dagger] = \delta_{mn}$ and $[\ \hat{a}_n^{(\dagger)},\ \hat{a}_m^{(\dagger)}] = 0$. Following [38], the full Hamiltonian that describes the coupled resonator-DQD system reads in this notation

$$\hat{H} = \frac{h\Omega}{2}\hat{\sigma_z} + \sum_n h\nu_n \hat{a}_n^\dagger \hat{a}_n + \hbar(g_z^n \hat{\sigma_z} + g_x^n \hat{\sigma_x})(\hat{a}_n^\dagger + \hat{a}_n) \tag{10}$$

where $|+>$ and $|->$ are eigenstates of $\hat{\sigma}_z$ with eigenvalues ± 1, $\hat{\sigma}_x = \hat{\sigma}^+ + \hat{\sigma}^-$ and coupling constant g:

$$g_z^{(n)} = g(\delta/2\Omega)\sqrt{\omega_n/\omega_0} \tag{11}$$

$$g_x^{(n)} = g(t/\Omega)\sqrt{\omega_n/\omega_0} \tag{12}$$

$$g = \omega_0 c\sqrt{\frac{2Z_0 e^2}{h}} \tag{13}$$

Z_0 is the characteristic resonator impedance. Neglecting non-energy conserving terms respectively rewriting the full Hamiltonian in the rotating wave approximation (RWA), the Hamiltonian reads for the fundamental mode $\nu_{n=0}$ [38]

$$\hat{H} = \frac{h\Omega}{2}\hat{\sigma_z} + h\nu_0\hat{a}^\dagger\hat{a} + \hbar g\frac{t}{\Omega}(\hat{a}^\dagger\hat{\sigma}^- + \hat{a}\hat{\sigma}^+) \tag{14}$$

where ν_0 is the fundamental mode frequency and $\hat{a}^\dagger$ and $\hat{a}$ are creation and annihilation operators for an excitation in the fundamental mode i.e. of a photon into and from the resonator. This Jaynes-Cummings type Hamiltonian describes a dipole coupling between resonator and double quantum dot and shows a direct analogy between the coupled resonator-DQD system and atomic cavity QED [38] for a two-level system with eigenenergies

$$E_\pm = h\nu_0 n \pm \sqrt{(h\nu_0 - h\Omega)^2 + (2\hbar g\frac{t}{\Omega})^2(n+1)} \tag{15}$$

in a subspace with basis $|+, n>$ and $|-, n+1>$. For a full description of the coupled system in use, a resonator drive as well as decoherence respectively relaxation needs to be taken into account. The resonator drive can be described by a coherent field that is coupled capacitively through input lines to the resonator. This drive field adds additional photons to the resonator, modeled by a Hamiltonian of the form (cf. e.g. [39])

$$\hat{H}_{res.drive} = \hbar(\epsilon^*(t)\hat{a}^\dagger + \epsilon(t)\hat{a}) \tag{16}$$

with photon creation operator $\hat{a}^\dagger$. $\epsilon(t)$ refers to a time dependent change in the drive amplitude of the form $\epsilon(t) = \epsilon e^{i\omega_D t}$ and ω_D is the drive frequency. Similar to a coherent drive, losses of the resonator field need to be taken into account. An intuitive picture is given by a resonator mode that is coupled to the environment via an effective coupling constant. The coupling of a free field Hamiltonian to the i-th environmental modes is given by [40]

$$\hat{H}_{res.-loss} = -\sum_i \hbar\frac{j_i}{2}(ab_i^\dagger e^{-i(\omega_0-\omega_i)t} + a^\dagger b_i e^{i(\omega_0-\omega_i)t}) \tag{17}$$

where the sum includes all environmental modes i and j_i is a coupling constant that depends on the respective mode. a ($a^\dagger$) and b_i ($b_i^\dagger$) are annihilation (creation) operators for a photon in the resonator respectively environmental mode. The full Hamiltonian with coherent drive and resonator losses reads

$$\begin{aligned}\hat{H} = \frac{h\Omega}{2}\hat{\sigma_z} + h\nu_0\hat{a}^\dagger\hat{a} + \hbar g\frac{t}{\Omega}(\hat{a}^\dagger\hat{\sigma}^- + \hat{a}\hat{\sigma}^+) + \hbar(\epsilon^*(t)\hat{a}^\dagger + \epsilon(t)\hat{a}) \\ - \sum_i \hbar\frac{j_i}{2}(ab_i^\dagger e^{-i(\omega_0-\omega_i)t} + a^\dagger b_i e^{i(\omega_0-\omega_i)t})\end{aligned} \tag{18}$$

In a resonant case, an anticrossing would be observable at the degeneracy point where qubit transition frequency and resonator frequency are degenerate. Please refer to [41] for

more details on the Jaynes-Cummings Hamiltonian at resonance. However, equation (18) only holds in an ideal model without qubit dephasing and relaxation. In a more realistic model, qubit relaxation and decoherence need to be taken into account. Such a system can be modeled by a Markovian master equation with additional operators to account for such processes.

Fig. 19a shows a schematic of an anticrossing while Fig. 19b gives an example for the steady-state solution of a master equation approach that includes relaxation and dephasing for a similar case. A software for numerical simulation, developed in the group of Alexandre Blais at University of Sherbrooke, Canada is used to extract coupling strength as well as tunneling and dephasing rates following Frey *et al.* [12].

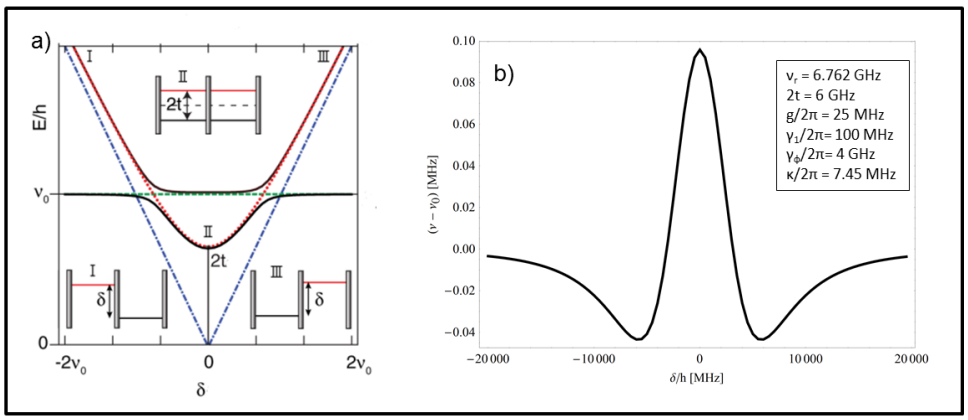

Figure 19: a) Eigenenergies of the coupled resonator-qubit system (black). Avoided level crossing at the degeneracy point where resonator (green) and DQD transition frequency (red) meet, adopted from [12]. The figure corresponds to a Jaynes-Cummings Hamiltonian without qubit dephasing and relaxation. b) Resonator frequency shift simulated numerically from a master equation approach based on a Jaynes-Cummings Hamiltonian. The model includes additionally qubit relaxation and dephasing (see text).

Depending on the qubit transition frequency with respect to the resonator resonance frequency, the resonator shifts either to lower ($\nu_{qubit} > \nu_{resonator}$) or higher frequencies ($\nu_{qubit} < \nu_{resonator}$), compared to the bare resonator frequency. An intuitive explanation for the strong coupling regime can be derived from an effective Hamiltonian that is approximated in the dispersive regime where qubit transition frequency and resonator frequency are far off-resonant, i.e. $\Delta \gg 1$. The approximative Hamiltonian reads for the Hamiltonian in Eq. (14)

$$\hat{H_{eff}} = h(\nu_0 - \frac{G^2}{4\pi^2\Delta}\sigma_z)\hat{a}^\dagger\hat{a} + \frac{1}{2}h(\Omega + \frac{G^2}{4\pi^2\Delta})\sigma_z \tag{19}$$

where G = $g\ t/\Omega$ and $\Delta = \Omega - \nu_0$. Please refer to e.g. [5, 42] for a derivation. Here, Δ accounts for a positive or negative frequency shift of the resonator, depending on the qubit and resonator frequency. This serves as an additional read-out channel for the qubit state by probing the state-dependent frequency shift of the resonator with resonance frequency $\nu_0 \pm G^2/4\pi^2\Delta$. Assuming the DQD always in its ground state, justified by large relaxation rates in similar systems of the order of $\gamma_1/2\pi = 100$ MHz [12, 43, 44, 45], a changing sign in the resonator shift translates to a positive respectively negative detuning. Due to large qubit dephasing and energy relaxation rates, an anticrossing is not visible at the degeneracy points (cf. Fig. 19b).

5 Double quantum dot charge qubit in a circuit QED architecture

Different theories of coupling a DQD to a microwave resonator, developed by Childress *et al.* [38] and discussed in section 4.2 in terms of probing the dot admittance and in 4.3 for a quantum mechanical treatment, suggest a shift in resonance frequency whenever the qubit transition frequency is close to the resonator frequency. It has been shown with great success, that the dipole coupling of a transmission line resonator is an impressive tool to probe the state of gate defined quantum dots [10, 12, 13, 16]. This section reports on studies of a DQD by means of its interaction with a microwave resonator.

5.1 Detection scheme

Resonator and DQD are probed in a heterodyne detection scheme. Please refer to Appendix C for a schematic of all components. A coherent microwave tone is applied to the resonator and the transmitted signal is measured in terms of its field quadratures I and Q, where $Ae^{i\phi} = I + iQ$, after down-conversion with a local-oscillator field. Amplitude A and phase ϕ of the transmitted signal is studied. The reader is referred to e.g. Wallraff *et al.* [7] for more information on the heterodyne detection scheme.

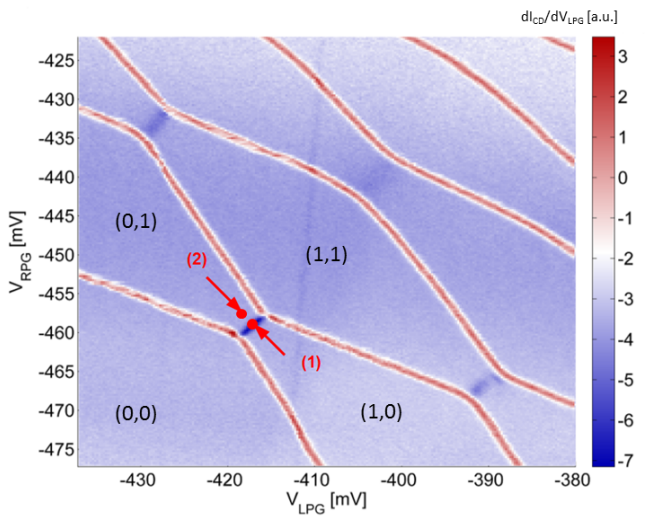

Figure 20: QPC transconductance measurement in the vicinity of the (1,1) Coulomb blockade region. Two characteristic measurement positions (1) and (2) are indicated, please refer to Appendix B [A5] for a set of all gate voltages

To probe for the previously discussed classical (admittance) and quantum mechanical model, the resonator response is measured at two characteristic points (1) and (2), depicted in Fig. 20. Both models suggest that the resonator resonance frequency is different at point (1) compared to (2), as there is either a difference in the DQD admittance (classical model) or a different detuning between qubit transition and resonator frequency. Note that the transconductance measurement, shown in Fig. 20, is intended to indicate the measurement points only. Although the measurement techniques are different between DC and microwave readout, the transconductance map nevertheless serves as a reference for microwave studies. A full transmission spectrum for the fundamental mode of the resonator allows to extract amplitude, resonance frequency and linewidth by a Lorentzian line shape fit, identical to the procedure presented in section 2.2. For such a measurement, it is assumed that the transmission spectrum remains Lorentzian at each point in LPG-RPG subspace (cf. Fig. 21a). A change (e.g.) in the admittance of the dot, comparing point (1) and (2), should be visible in terms of a frequency shift and possibly a reduction in amplitude for dissipative processes. Note that the measured points (1) and (2) are different. Within the Coulomb blockade region (point (2)), the energy difference between neighbouring charge

states is dominated by the charging energy, which is orders of magnitude higher than the energy of a photon in the transmission line resonator. The electron wavefunction remains unaffected and no significant change in the dipole moment is induced by the resonator. However, close to an interdot charge transfer line (point (1)), energy scales are comparable and the dynamics of an electron within the double dot can be probed via the resonator. In a full quantum mechanical description (cf. section 4.3), these two points are different when considering the detuning between qubit transition and resonator frequency. Off-resonant, a possible state-dependent frequency shift $G^2/4\pi^2\Delta$ (cf. Eq. (19)) would only be observable for sufficiently small detuning. Nevertheless, the qubit transition frequency changes along a line from (1) to (2) and both points show a different detuning from the bare resonator frequency, which will be observed in the following. The qubit is assumed to be in its ground state at all times due to large relaxation rates, typical for charge qubits [12, 44].

Fig. 21 gives exemplarily the squared transmission amplitude (a) and phase (b) at the two characteristic points (1) and (2). Resonance frequencies of 6.7622 GHz (blue) and 6.7619 GHz (red) are fitted what corresponds to a shift of 300 kHz in this example. The amplitude decreased at the same time by 336 μV^2 and the quality factor is 58.5 less for the resonator measured at point (1). The resonator shows a quality factor of 905.8 (2) respectively 847.3 (1) for the gate-voltages chosen. An increasing linewidth suggests a dissipative process at which the resonator is sensitive to a non-vanishing real-part of the complex impedance, when the dynamic admittance of the DQD is probed.

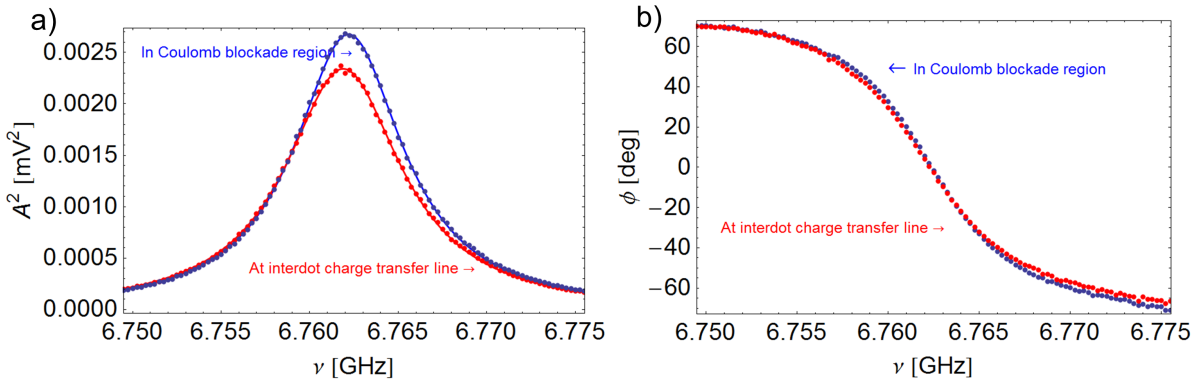

Figure 21: Squared transmission amplitude and phase at two characteristic points in the charge stability diagram, refer to Appendix B [A6] for all voltages.

Measuring the full transition spectrum at each point in LPG-RPG subspace for a series of various DQD configurations is however time-consuming. Alternatively, the resonator is probed at a fixed resonator frequency for each plunger gate configuration (LPG,RPG). First, a reference frequency is extracted from a measurement of the full transmission spectrum for a point (LPG,RPG) deep within the Coulomb blockade region. In a second step, the resonator transmission is analyzed for each point on the map at fixed frequency, assuming that the probe signal is close to resonance within different Coulomb blockade regions and becomes off-resonant close to or at the interdot charge transfer line, depicted by the dark blue color in Fig. 20. An off-resonant signal will be observable by a drop in transmission amplitude, compared to the on-resonant case. Complementary, the transmission phase can be measured at fixed frequency while a unique phase shift in both regions translates into positive or negative frequency shift.

5.2 Interdot charge transfer line

The model suggested in section 4.3 predicts two characteristic regimes when probing the resonator in the vicinity of an interdot charge transfer line, including dephasing and relaxation processes. The minimal qubit transition frequency 2t is either higher or lower in comparison to the uncoupled resonator frequency ν_r. In the case of a higher transition energy (Fig. 22), the resonator frequency shift is only negative, whereas in the case of a lower frequency, the shift is expected to be negative at the edges of an interdot charge transfer line and positive along the line (Fig. 23b, 19a). A frequency shift translates into a change in transmission phase, such that a negative (positive) frequency shift results in a negative (positive) phase shift. Fig. 22 and Fig. 23 show data sets for transmission phase, measured at a fixed resonator frequency $\nu_r = 6.762$ GHz in LPG-RPG subspace in the vicinity of a charge transfer line. Refer to Appendix B [A7, A8] for a set of parameters. Also shown is schematically the expected frequency shift along the line indicated δ in Fig. 22a (Fig. 23a), cf. also Fig. 19. The minimal qubit transition frequency was tuned by the voltage applied to the center gate V_c, which translates to a different tunnel barrier width and height and thus a different dispersion relation of the qubit.

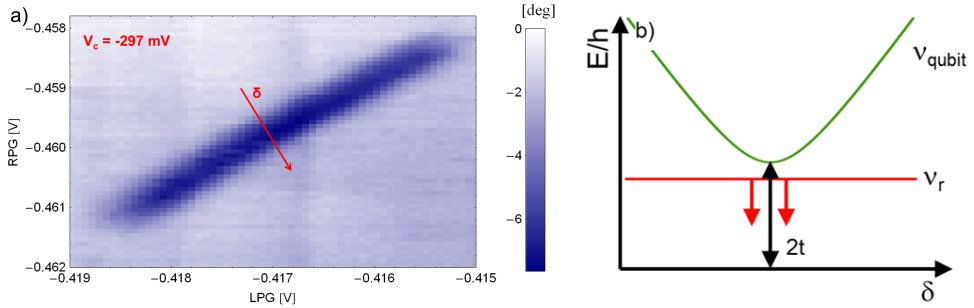

Figure 22: $2t > \nu_r$: Transmission phase from experiment a) and schematic along δ b). Decreasing resonator frequency in the case of minimum qubit transition frequency larger than resonator frequency. Refer to Appendix B [A7] for a set of all parameters

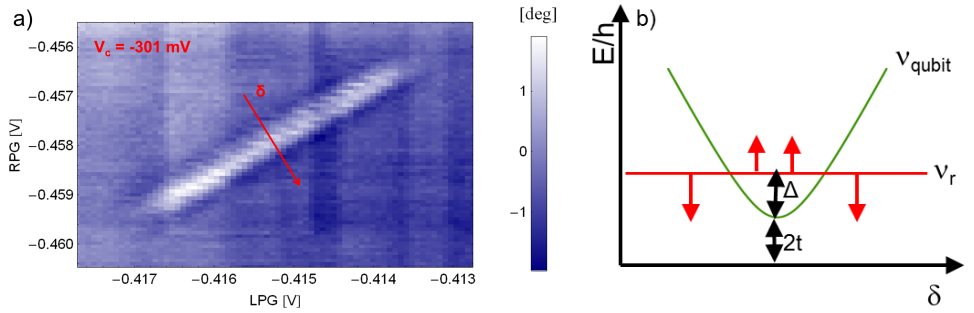

Figure 23: $2t < \nu_r$: Transmission phase from experiment a) and schematic along δ b). Decreasing as well as increasing resonator frequency in the case of minimum qubit transition frequency larger than resonator frequency. Refer to Appendix B [A8] for a set of all parameters

In a similar manner, the transmission amplitude can be measured for fixed resonator frequency. Fig. 24 presents the transmission amplitude for a parameter set that corresponds to the phase signal shown in Fig. 22 (a) and 23 (b). A drop in the signal is observed, indicated by the dark blue color. The resonator resonance is probed at fixed frequency, which was chosen on-resonant in a Coulomb blockade region. Close to and at the in-

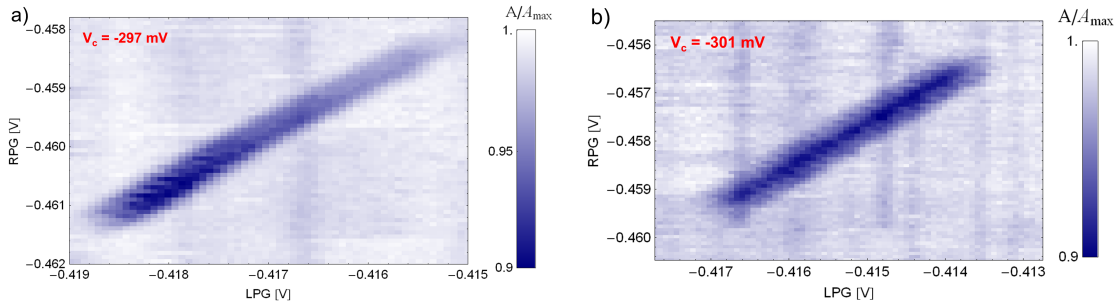

Figure 24: Transmission amplitude for fixed resonator frequency. Refer to Appendix B [A7]

terdot charge transfer line, the resonator frequency shifts and the probe signal becomes off-resonant and the transmission amplitude decreases. Dissipation might further decrease the transmission amplitude. Depending on the resonator quality factor and parameter regime, the sensitivity in measuring amplitude or phase might vary. It was experimentally observed that a signal in amplitude was measured while no signal in phase occurred and vice versa (not shown).

5.3 Necessity for single electron charge qubits

Recently published data by Frey *et al.* [12] for many electron quantum dots reports on decoherence rates in the order of 1 to 3 GHz, while a coupling strength of 50 MHz is achieved. Decoherence rates, orders of magnitude higher than the dipole coupling, remain a fundamental issue on the way towards strong coupling.

Fig. 25 summarizes some of the main results of [12]. Shown is the transmission phase in LPG-RPG subspace, (a) and (b), as well as the change in resonance frequency along the black dashed line. Frey *et al.* motivate the absence of an anticrossing, respectively of vacuum Rabi mode splitting, by a qubit decoherence rate that is significantly larger than the coupling strength. The measured frequency shift (c) closely follows the predicted behavior, assuming the minimal qubit transition frequency 2t (cf. section 4.1) lower than the resonator frequency respectively larger (d). A numerical simulation of the frequency shift, assuming a Jaynes-Cummings Hamiltonian (Eq. (18)) as well as qubit and resonator relaxation and qubit dephasing, predicts the observed frequency shift.

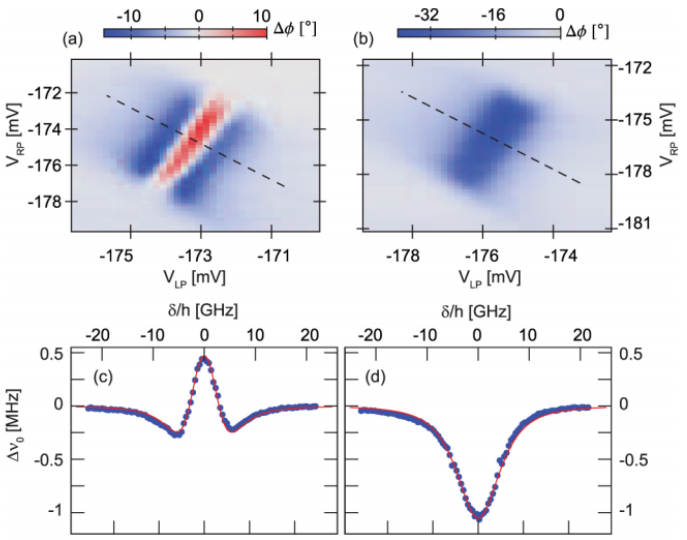

Figure 25: Transmission phase (a) and (b) for two different interdot tunnel rates $2t < \nu_r$ (a) and $2t > \nu_r$ (b). The resonator frequency along the black dashed line is shown in (c) and (d), corresponding to the configuration in (a) respectively (b). No avoided level crossing observable. Data and plots from Frey *et al.* [12]

A comparison can be drawn e.g. to Fig. 19b which simulates a qubit with minimal transition frequency 2t = 6 GHz, qubit dephasing rate $\gamma_\phi/2\pi = 4$ GHz, qubit relaxation rate $\gamma_1/2\pi = 100$ MHz and coupling strength $g/2\pi = 25$ MHz. The resonator frequency was set to 6.762 GHz in this simulation. Please refer to section 5.5 for a systematic study of the previously introduced model (Eq. (18)) and further numerical simulations.

Excited charge states, resulting from discrete quantization energies, might constitute an additional decoherence channel. The spacing in energy between those states, known as the single particle level spacing, can be estimated to be $\Delta = \hbar^2/m^* r^2$, following [18] and a derivation given in section 3.1. The spacing between ground and excited charge states thereby scales like $1/r^2$ with r the dot size. Few and single electron dots are smaller in size compared to many electron dots and thereby excited states are energetically more separated. Thus, a promising approach to study and to reduce dephasing rates is to analyze single electron quantum dots for which this additional decoherence channel, due to nearby excited states, is reduced. Additionally, single electron quantum dots have the benefit that the system can be modeled without considering many-particle effects, such that the previously derived Hamiltonian (Eq. (18)) holds and describes a single electron that occupies either the left or the right dot at zero interdot tunnel coupling.

5.4 Towards the last electron

This section discusses steps and difficulties towards the observation of a dipole coupling between a single electron and a resonator. Measurements in the single electron regime are presented and compared to the many electron DQD.

5.4.1 Effects of plunger gates on interdot tunnel rate

Separate plunger gates are employed in the used sample design currently to change the static dot potential, whereas the dot itself is primarily formed by side and center gates. However, a finite cross-coupling of gates can not be avoided in mesoscopic structures. This effect became first evident in the charge stability diagrams in terms of a finite slope of co-tunneling lines corresponding to a resonance condition between one dot and its neighboring reservoirs, depicted in Fig. 5c and 7a respectively for experimental data. More significant in terms of charge qubits is an effective change of the tunnel barrier with a change in plunger gate voltage, that was shown to be pronounced in the given sample. Such a dependence was first observed in DC measurements (cf. 2.4.2) and is measurable in the microwave regime likewise. A plot of transmitted amplitude (Fig. 26a) and phase (Fig. 26b) at fixed resonance frequency shows this effect. The data maps the measured transmission signal in LPG-RPG subspace. A change in plunger gate voltage leads to a transition from negative (dark blue color in Fig. 26b) to positive phase shift (white color in Fig. 26b) whereby the minimal qubit transition frequency changes from above to below the resonator frequency. This is explained by a change in tunnel rate and shows the dependence of the interdot tunel rate on plunger gate voltages in our sample.

The dependence of the voltage applied to plunger gates on the interdot tunnel barrier was a crucial point to consider when operating the DQD in the single electron regime. In such a regime a single electron remains that is shared between both dots. Emptying the dot requires increasingly negative plunger gate voltages to tune the static potential

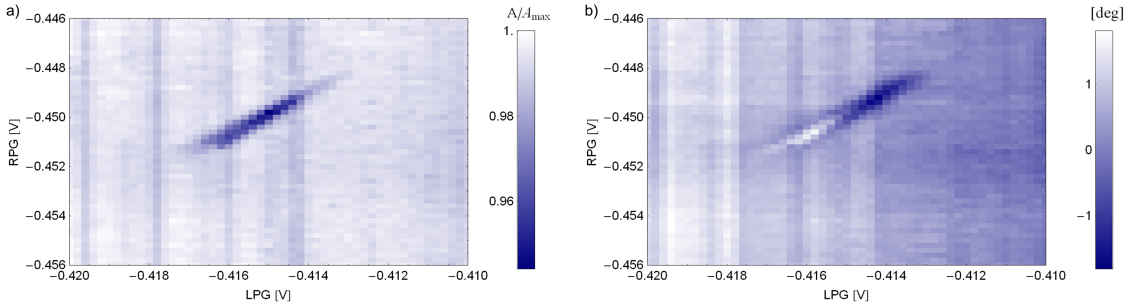

Figure 26: Transmission amplitude (a) and phase (b) at fixed resonator frequency in the vicinity of a charge degeneracy line. Please refer to Appendix B [A9] for a set of all parameters. A change in the transmission phase from positive (white) to negative (dark blue) within the same interdot charge transfer line signifies a strong effect of plunger gates on the interdot tunnel barrier.

appropriately, which decreases the interdot tunnel-coupling to a regime where the resonator is not necessarily sensitive to the qubit transition frequency. A careful selection of voltages applied to side and center gates was important when a single electron DQD is formed.

5.4.2 Resonator characteristics (ν, Q, A) and its dependence on top-gate voltages

A change in amplitude and phase is observable in LPG-RPG subspace which goes along with static resonances that are independent of the voltage applied to the right plunger gate over large voltage ranges, shown in Fig. 27. This change in amplitude and phase, on top of possible DQD resonances, complicates the detection and systematic studies and formed a major difficulty on the way to a single electron DQD, especially as the transition occurred in a region where a single-electron resonance was expected. The resonator dependence on top-gate voltages is more systematically discussed in section 6.

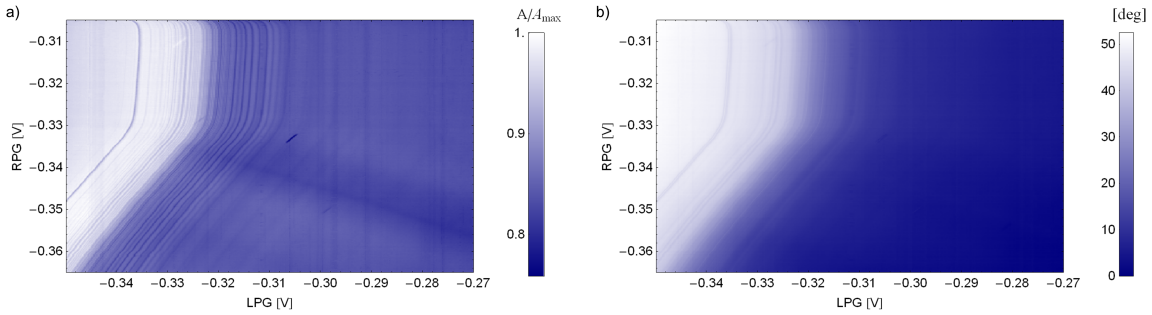

Figure 27: Transmission amplitude (a) and phase (b) in LPG-RPG subspace. A change from light blue to dark blue shows an abrupt change in the measured amplitude and phase of the transmitted microwave signal that is independent of the charge state of the DQD. Additional resonances are visible in the vicinity of this transition region. Refer to Appendix B [A10] for a set of all parameters

One strategy to overcome these difficulties is to operate the dot in a regime, where few-electron resonances are expected to be far from this transition region, respectively by tuning resonances away from this region. This can be achieved by an appropriate interplay of side and plunger gates. More negative side gates allow for less negative plunger gates and vice versa to resemble a similar dot configuration.

5.4.3 Single electron double quantum dot

Facing the difficulties mentioned in the previous subsection, a better understanding of the dot characteristics allowed to tune the system into a regime in which the interdot tunneling of a single remaining electron in the DQD can be observed in a microwave measurement.

Formation of a single electron DQD: A series of steps necessary for the formation of a DQD is given in Appendix A for the currently used sample design. However, special care has to be taken to avoid the difficulties discussed previously. For one point, it was observed that the plunger gates have a significant effect on the interdot tunnel rate whereby it is expected that strongly negative plunger gate voltages decrease the tunnel rate to an extent at which the resonator becomes insensitive to those processes. To overcome this, we attempted to operate the DQD in a single electron regime but tried to avoid for increasingly negative voltages applied to plunger gates. This can be achieved by setting the side gates more negative. Side gates not only form the dot, but also contribute to the static potential within the dot. In combination with side gates, plunger gates now need to be less negative in voltage to reach the single electron limit. In a second step, the double quantum dot was further tuned into a region at which a direct current through the dots was measurable almost up to the last electron which indicates that all tunneling currents through the dot are strong. This was achieved mainly by changing the center gates V_c (CG) and SDB and thereby increasing the interdot tunnel rate (cf. Fig. 4). Once a resonance is visible in the microwave measurement, the signal to noise ratio was further optimized by a combination of varying side and center gate voltages, based on the observed phase signal, i.e. the direction of the phase shift.

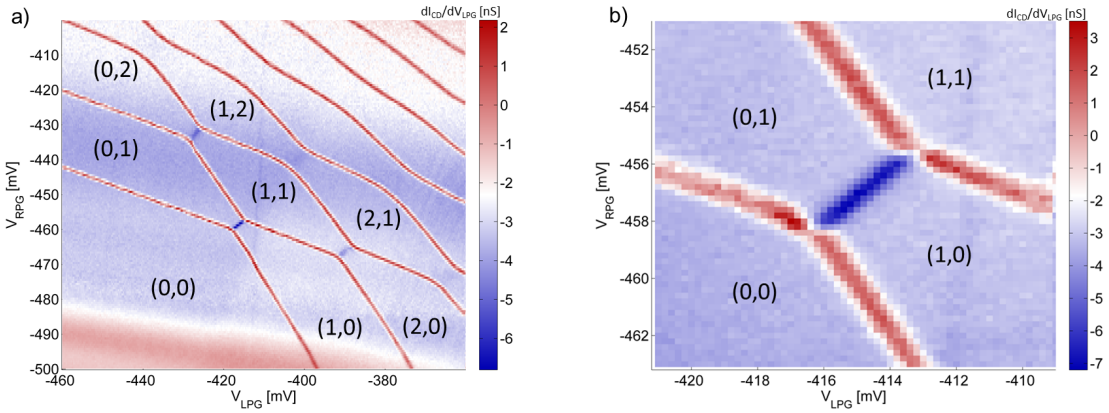

Figure 28: QPC transconductance charge stability diagram in the few electron regime. The number of electrons in the dots is indicated. Here, (0,1) stands for no electron in the left and one electron in the right dot. Refer to Appendix B [A11] and [A12] for a set of all parameters

Starting from a direct current measurement, the DQD was first formed and tuned into the single electron regime as depicted above. A QPC transconductance measurement is plotted exemplary in Fig. 28a and in 28b for the interdot charge transfer line (blue) from (0,1) to (1,0) whereas (0,1) indicates no electron in the left and one electron in the right dot. From this measurement, it can be seen that the DQD charge qubit predominantly forms close to the (1,1) Coulomb blockade region. For an increasing number of electrons, i.e. less negative plunger gate voltages, the two individual dots become strongly coupled and show the response of a single large quantum dot. The theoretically expected hexagonal

shape disappears, seen in the upper right corner in Fig. 28a. Additionally, a pronounced rounding of the conductance (red line) close to the interdot charge transfer line from (1,2) to (2,1) respectively from (0,1) to (1,0), also shown in Fig. 28b, indicates a strong interdot tunnel coupling. The rounding is related to a tunnel broadening of the co-tunneling lines [26, 18].

The corresponding microwave measurement shows a resonance at the expected position of the interdot charge transfer line from (0,1) to (1,0). Assuming that no charge rearrangement has occurred, a direct comparison between DC and microwave studies proofs that the observed resonance in Fig. 29 indeed corresponds to a single remaining electron in the double quantum dot, dipole coupled to the resonator (cf. Fig 28). The resonance is clearly visible in amplitude (Fig. 29a) and less pronounced in phase (Fig. 29b). Note that no further resonances are visible in the vicinity of the (1,1) Coulomb blockade region by comparing Fig. 28 and 29. This again shows the effect of plunger gates on the interdot tunnel rate. Changing the plunger gate voltage by a few millivolts changes the tunnel rate and thereby the qubit transition frequency into a regime at which the resonator is not sensitive anymore, i.e. the detuning between resonator and qubit transition frequency increases significantly. It was checked, that by adjusting side and center gate, the remaining resonances individually become visible while the initial resonance, shown in Fig. 29, disappears. The number of visible resonances depends on the exact gate configurations and is only to be shown here as an example. A different gate configuration might allow for different resonances visible at the same time in the vicinity of the (1,1) Coulomb blockade region.

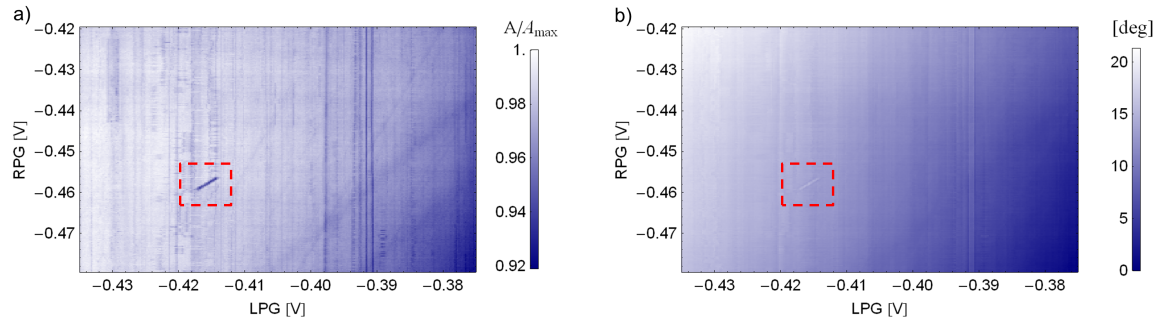

Figure 29: Resonator response in the few electron regime from a microwave measurement. A resonance at the position of the interdot charge transfer line from (1,0) to (0,1) is visible in amplitude (a) and phase (b), highlighted by the red-dashed line. The resonator is not sensitive to other charge degeneracy lines. Set of parameters in Appendix B [A13]

We proceed by further analyzing the interdot charge transfer line depicted above. In agreement with the previously discussed model, a positive or negative frequency shift in the resonator is expected to be observable whenever the qubit transition frequency is close to the resonator frequency. For such a measurement, a resonator transmission spectrum was probed for the fundamental mode at each point along the red dashed line indicated in Fig. 30a and 30b for different voltage applied to the center gate V_c (cf. also Fig. 4) and therefore for different interdot tunnel rates. A set of transmission phases, measured at fixed resonator frequency, is shown in Fig. 30a and 30b, with the resonator resonance frequency and linewidth shown in Fig. 30c and 30d for three different center gate voltages. Note that a transition from a negative frequency shift (green) to a positive frequency shift (blue) occurs when applying more negative voltage to the center gate V_c. This is in good agreement with the model previously discussed and shows a change in the minimum

transition frequency 2t from above (green) to below (blue) the resonator frequency as a result of decreasing tunnel rate. This data looks similar to work by Frey *et al.* [12], despite carrying out experiments in a single electron DQD. In fact, no indications for a strong coupling regime respectively reduced dephasing rates, compared to previously published work, are visible. However, a conclusion on dephasing rates between the single and many electron regime should be drawn within the same sample. This is because contributions of various decoherence sources (cf. chapter 5.7) might change when considering different sample designs and semiconductor heterostructures.

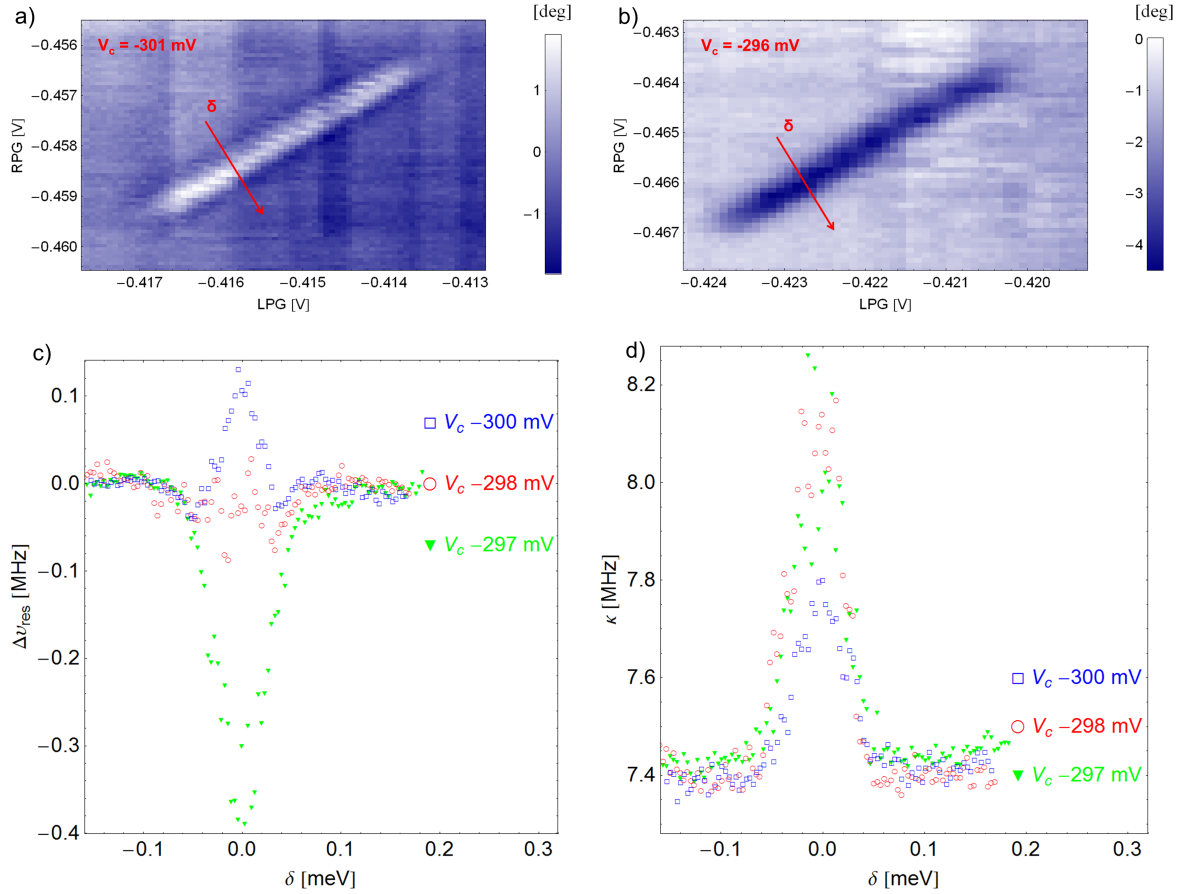

Figure 30: a) and b): Transmission phase for two different interdot tunnel rates, given a different voltage applied to the center gate V_c in a single electron DQD, c) and d): Resonator frequency shift and linewidth, measured along the red dashed line in a) and b), are extracted from a Lorentzian line fit similar to the procedure described in section 2.2. Please refer to Appendix B for a full set of parameters: [A8] (a), [A14] (b), [A15] (c) & (d)

Based on these data, it is instructive to further study decoherence and to compare the qubit characteristics with previously published work on DQD charge qubits. We therefore model our system in terms of a Jaynes-Cummings Hamiltonian (equation 14, following [12]) and introduce dephasing and relaxation. The resonator frequency and linewidth are obtained from a numerical simulation, based on a Lindblad master equation with the previously described Hamiltonian. A program to simulate those data was provided by the group of Alexandre Blais, University of Sherbrooke [46]. In the following, the proposed model is analyzed in terms of coupling strength, qubit dephasing and relaxation as well as interdot tunnel rates. Comparing those results with the obtained experimental data, conclusions on qubit parameters are drawn.

5.5 Numerical simulation: Pre-analysis for model

Simulating a quantum systems, based on a Jaynes-Cummings type Hamiltonian with qubit relaxation and dephasing, is fruitful to understand the physics of a qubit coupled to an environment and to explain the characteristic features that were observed in the experiment. In the following, resonator resonance frequency and linewidth are numerically simulated for changing characteristics such as coupling strength g, interdot tunneling t, qubit dephasing rate γ_ϕ, qubit relaxtion rate γ_1, drive amplitude ϵ, qubit temperature T, resonator thermal population n_{th} and Hamiltonian size i.e. number of photons in the simulation n_{ph}. An understanding of the coupled resonator-qubit characteristics, based on those parameters, is essential to further analyze experimental data in the single and many electron regime. All data sets shown in this section are based on a numerical simulation, following a Markovian master equation approach in a Lindblad form, following [47]:

$$\partial\hat{\rho}/\partial t = -i[\hat{H},\hat{\rho}] + \kappa D[\hat{a}]\hat{\rho} + \gamma_1 D[\hat{\sigma}_-]\hat{\rho} + \gamma_\phi D[\hat{\sigma}_z]\hat{\rho}/2 \tag{20}$$

$\hat{H}$ describes the previous model in equation (14) with qubit relaxation γ_1 and dephasing rate γ_ϕ and photon decay rate κ. $D[\hat{O}]\rho = (2\hat{O}\hat{\rho}\hat{O}^\dagger - \hat{O}^\dagger\hat{O}\hat{\rho} - \hat{\rho}\hat{O}^\dagger\hat{O})$ in this context. The reader is refereed to e.g. [48] for details of a master equation with Lindblad operators. The employed software SQUACK - Sherbrooke QUantum pACKage - was kindly provided by Prof. Dr. Alexandre Blais [5] and Dr. Maxime Boissonneault [47].

5.5.1 Coupling strength g

The coupling between a DQD charge qubit and resonator depends on the capacitive differences in the coupling of the resonator to the individual dots, and scales as $g = \omega_0 c\sqrt{2Z_0 e^2/\hbar}$ with $c = \mid C_c/(C_c+C_{d1}) - C_i/(C_i+C_{d2}) \mid$ where $C_{c(i)}$ describe the capacitive coupling to the individual dots (cf. Fig. 18 and section 4.3), $C_{c(i)}+C_{d1(d2)}$ the total capacitance of the respective dot, $\omega_0/2\pi$ the resonator resonance frequency and Z_0 is the characteristic resonator impedance. Equivalently, the coupling strength can be reformulated in terms of lever arms to account for the capacitive coupling between dot and resonator gate. In the following, the influence of the coupling strength g is studied for two cases, minimum qubit transition frequency below (Fig. 31 and 32) and above (Fig. 33 and 34) the resonator frequency. In such a simulation, all parameters, except for the coupling strength, were held constant (cf. inset Figures 31 to 34). Following equation (15), the resonance frequency of the coupled system is given by $\nu = \nu_0 n \pm \sqrt{(\nu_0-\Omega)^2 + (4\pi g t/\Omega)^2(n+1)}$. In the off-resonant approximation, a resonator frequency shift $G^2/(\nu_0-\Omega)$ (cf. Eq. (19)) is predicted. A resonance shift thus scales with the square of the coupling strength, whereas the magnitude of the shift is inversely proportional to the detuning between qubit and resonator. At constant detuning, i.e. constant δ for all cases, the frequency shift is expected to increase quadratically, as seen along a line parallel to the y-axes in Fig. 31 and 33, both for positive (Fig. 31) and negative frequency shifts (Fig. 31 and 33). Note that this predicted behavior is affected by dephasing and relaxation, not included in equation (15) and (19). Nevertheless, the overall tendency for an increasing frequency shift with increasing coupling strength is evident. Worth noting is that the position of the minima, as well as the overall shape, remain unaffected. The coupling strength therefore mainly scales the overall resonance frequency shift, a feature similarly observed for the resonator linewidth in Fig. 32 and 34.

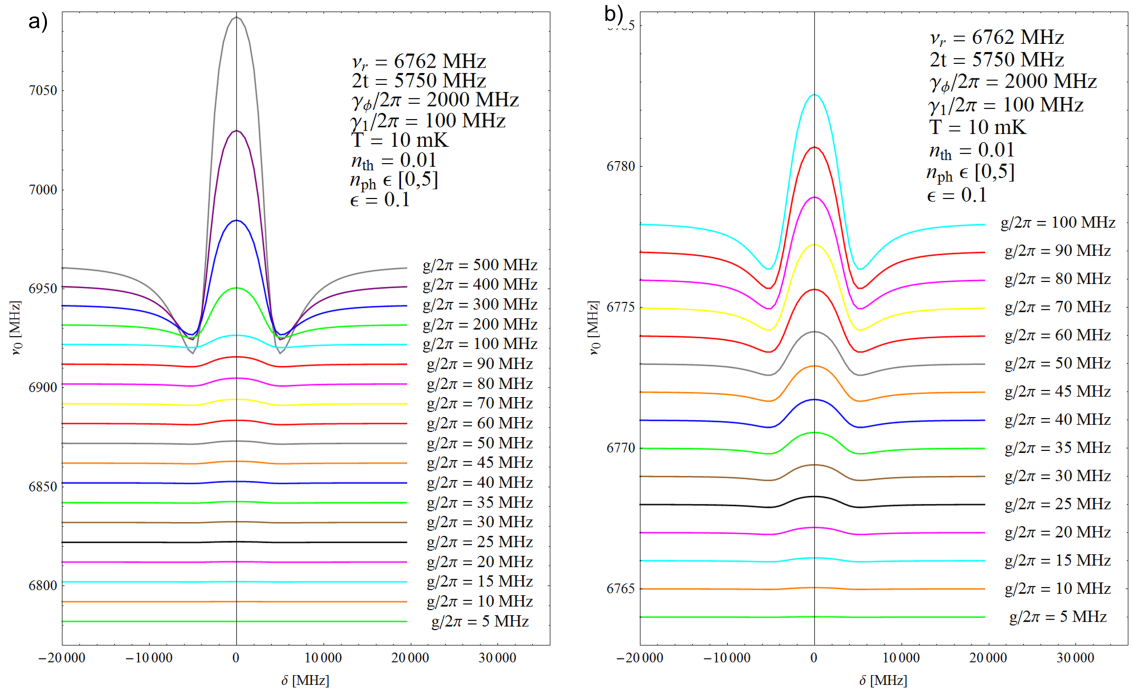

Figure 31: Case 1: Evolution of resonator resonance frequency as a function of coupling g. In this configuration $2t < \nu_r$ with $\nu_r = 6.762$ GHz. An offset of 10 MHz was included for clarity to subsequent curves. Large scale (a) and subset (b).

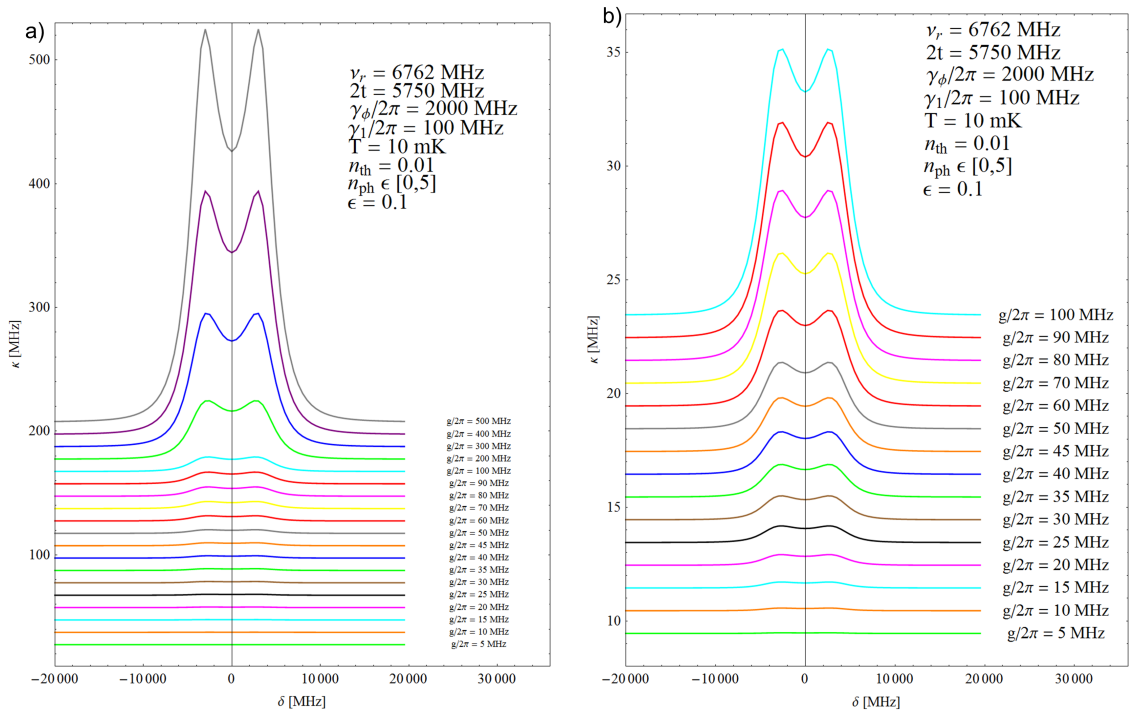

Figure 32: Case 1: Evolution of resonator linewidth as a function of coupling g. In this configuration $2t < \nu_r$ with $\nu_r = 6.762$ GHz. An offset of 1 MHz was included for clarity to subsequent curves. Large scale (a) and subset (b).

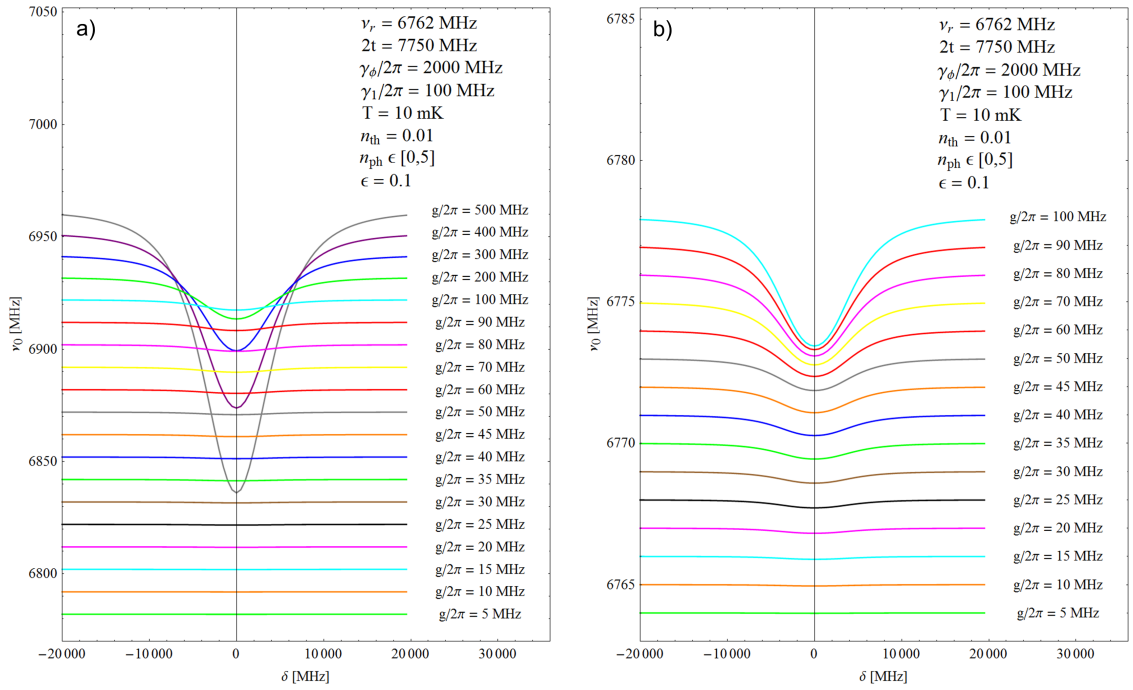

Figure 33: Case 2: Evolution of resonator resonance frequency as a function of coupling g. In this configuration $2t > \nu_r$ with $\nu_r = 6.762$ GHz. An offset of 10 MHz was included for clarity to subsequent curves. Large scale (a) and subset (b).

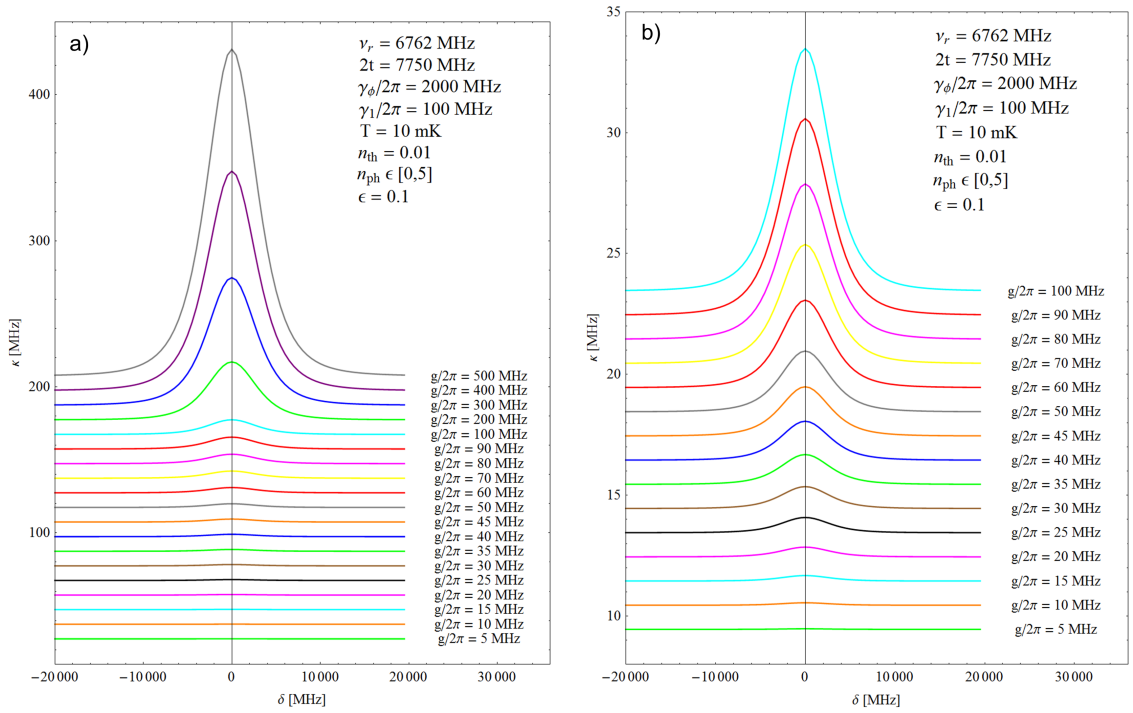

Figure 34: Case 2: Evolution of resonator linewidth as a function of coupling g. In this configuration $2t > \nu_r$ with $\nu_r = 6.762$ GHz. An offset of 1 MHz was included for clarity to subsequent curves. Large scale (a) and subset (b).

5.5.2 Interdot tunneling t

Studying the interdot tunnel rate is essential as this parameter can be controlled within the experiment by the width of the depletion region between both dots i.e. with applied gate voltage V_c. Similar to the coupling strength g, t is found to scale the overall frequency shift and linewidth (cf. $G = g\ t/\Omega$ for the dispersive case, equation (19)). Additionally, Fig. 19a suggests that the position of the minima changes as a function of the dot detuning δ, in the case of minimum transition frequency below the resonator frequency. Depending on the tunnel rate, qubit and resonator frequency are degenerate for different δ. This predicts an increasing separation of the minima with decreasing tunneling. Additionally, relaxation and dephasing have to be considered for a full explanation of the simulation data.

To further study the effect of qubit dephasing, the simulation was repeated for different decoherence rates $\gamma_\phi/2\pi = 500$ MHz (Fig. 35), $\gamma_\phi/2\pi = 1$ GHz (Fig. 36), $\gamma_\phi/2\pi = 2$ GHz (Fig. 37) and $\gamma_\phi/2\pi = 4$ GHz (Fig. 38). A major effect of increasing γ_ϕ seems to be the reduction of the observed features of positive and negative frequency shift, while maintaining the overall shape and position of minima ($2t < \nu_r$). This is more systematically studied in section *5.5.3 Qubit dephasing rate* γ_ϕ. Note that there is a change in the trend for linewidth when compared for different dephasing rates, most pronounced by a comparison of Fig. 35b and Fig. 38b: A double peak structure might be explained from Fig. 19a. At points where qubit transition and resonator frequency are degenerate, the resonator might excite the qubit, whereby qubit excitations not necessarily decay back into the resonator but additionally into the host crystal. In such a region, resonator losses are increased, shown by an increasing linewidth at those two positions, most pronounced in Fig. 35b. However, for increasing dephasing rates, those features successively wash out what can be seen in Fig. 38b.

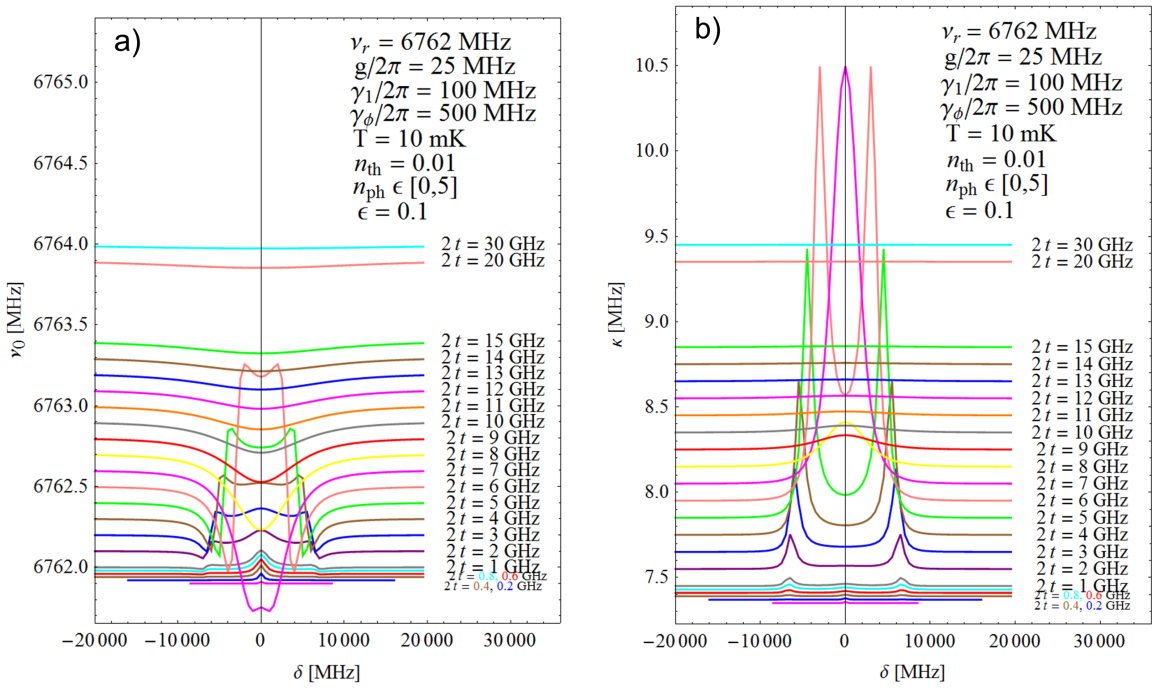

Figure 35: Resonator frequency shift (a) and linewidth (b) as a function of the energetic detuning δ for different interdot tunneling t. A qubit dephasing rate $\gamma_\phi/2\pi = 500$ MHz was simulated.

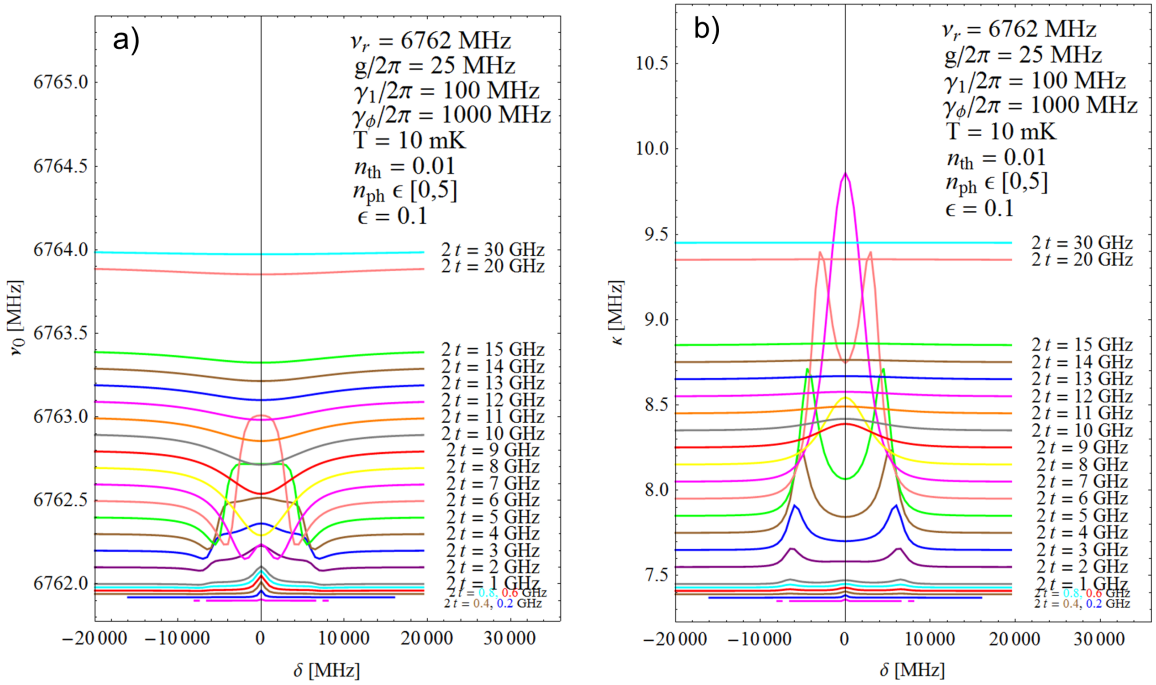

Figure 36: Resonator frequency shift (a) and linewidth (b) as a function of the energetic detuning δ for different interdot tunneling t. A qubit dephasing rate $\gamma_\phi/2\pi = 1$ GHz was simulated. All parameters in the inset. An offset of 100 kHz to subsequent curves was added for clarity

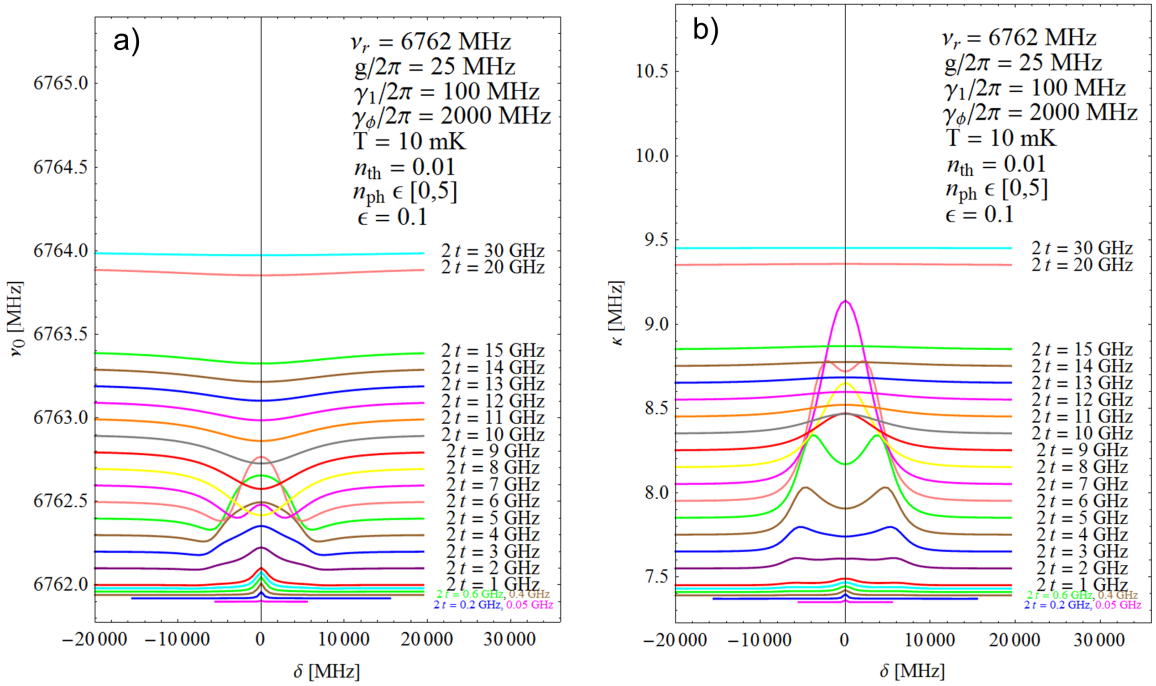

Figure 37: Resonator frequency shift (a) and linewidth (b) as a function of the energetic detuning δ for different interdot tunneling t. A qubit dephasing rate $\gamma_\phi/2\pi = 2$ GHz was simulated. All parameters in the inset. An offset of 100 kHz to subsequent curves was added for clarity.

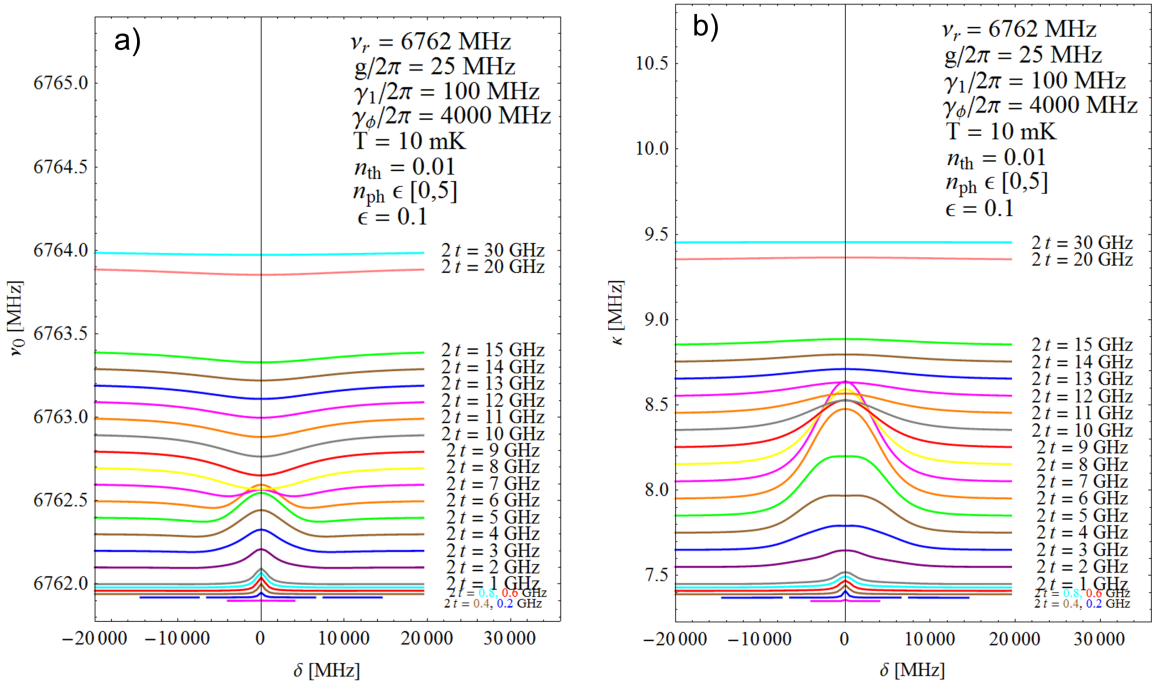

Figure 38: Resonator frequency shift (a) and linewidth (b) as a function of the energetic detuning δ for different interdot tunneling t. A qubit dephasing rate $\gamma_\phi/2\pi = 4$ GHz was simulated. An offset of 100 kHz to subsequent curves was added for clarity.

5.5.3 Qubit dephasing rate γ_ϕ

Again, both characteristic cases of a minimal qubit transition frequency smaller (Fig. 39) and larger (Fig. 40) than the bare resonator frequency are studied. In the case of ($2t < \nu_r$), higher dephasing rates smear out the double peak observed in frequency shift and linewidth for a shift to larger frequency respectively κ. The double peak, most pronounced at the qubit to resonator frequency degeneracy point successively disappears for increasing qubit dephasing γ_ϕ. Note that $\gamma_\phi >$ g in all simulations such that the coupled system is not in the strong coupling limit and avoided crossing not visible. A transition occurs, given the set of parameters in the inset, between 0.5 and 1 GHz for Fig. 39a and between 2.0 and 2.5 GHz for a measurement of the resonator linewidth (Fig. 39b) and the double peak successively vanishes. Additionally, the overall change in frequency and linewidth reduces with higher dephasing rates, also observed in the case of a larger interdot tunneling ($2t > \nu_r$, cf. Fig. 40). Note that the expression for qubit dephasing γ_ϕ and relaxation γ_1 mixes along δ, and lead to an overall inhomogeneous qubit decoherence rate γ_2

$$\gamma_2 = \gamma_1 sin^2\theta + \gamma_\phi cos^2\theta \tag{21}$$

with mixing angle $\theta = \arctan(2t/\delta)$. γ_ϕ and γ_1 are the bare dephasing respectively relaxation rates. In the simulation, γ_ϕ and γ_1 are given for large detuning δ and state the bare amplitudes, while the overall dephasing by means of equation (22) is considered along δ. We assume pure dephasing for $\theta = 0$. Note that the model uses a white noise approximation and the noise in tunneling t and detuning δ to be independent [49].

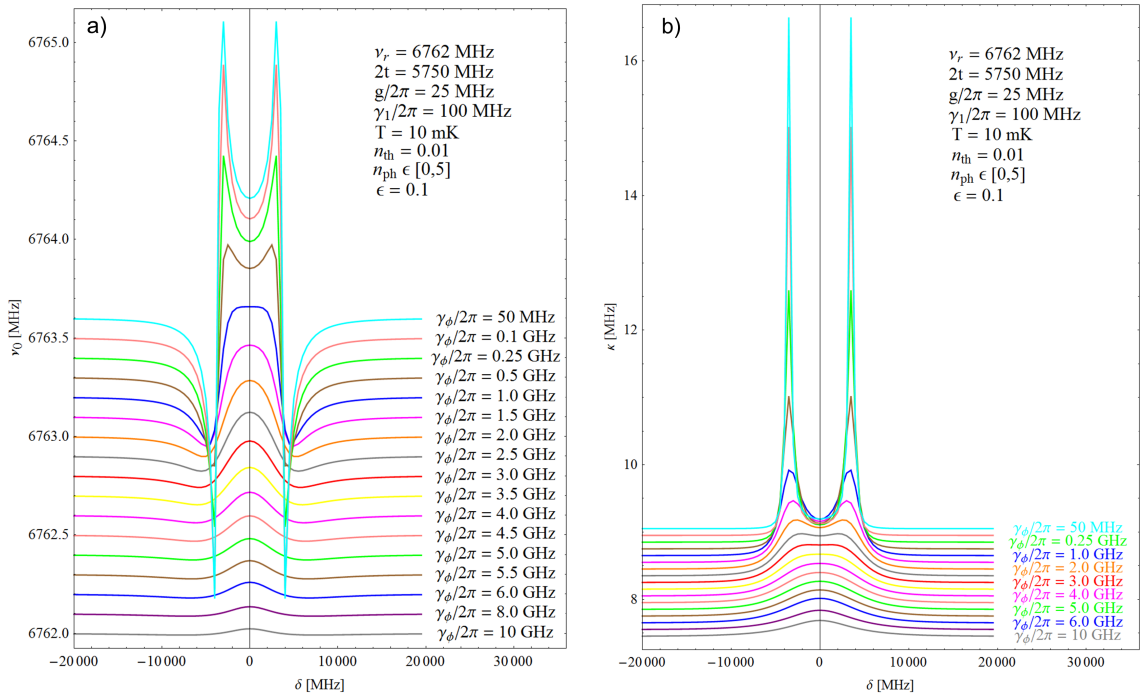

Figure 39: Case 1: Evolution of resonator resonance frequency (a) and linewidth (b) as a function of dephasing. In this configuration $2t < \nu_r$ with $\nu_r = 6.762$ GHz. An offset of 100 kHz to subsequent curves was included for clarity. Compare also Appendix D for inhomogeneous rate

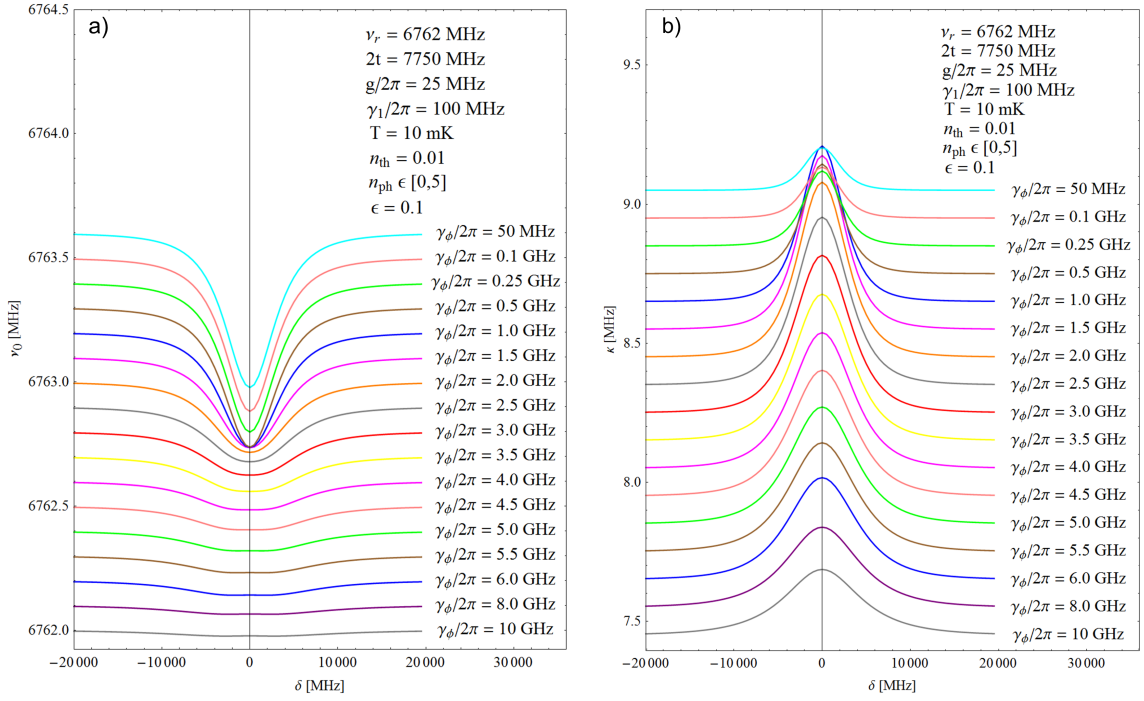

Figure 40: Case 2: Evolution of resonator resonance frequency (a) and linewidth (b) as a function of dephasing. In this configuration $2t > \nu_r$ with $\nu_r = 6.762$ GHz. An offset of 100 kHz to subsequent curves was included for clarity. Compare also Appendix D for inhomogeneous rate

5.5.4 Qubit relaxation rate γ_1

Petta *et al.* [44] report on charge relaxation times of 10 ns, i.e. a qubit relaxation rate γ_1 of 100 MHz, limited by the spontaneous emission of a phonon [44]. The effect of charge relaxation on frequency shift and linewidth are shown in Fig. 41 and Fig. 42 for different interdot tunneling t. Increasing relaxation leads to a signal reduction, both in amplitude and phase, although the overall shape is maintained up to several hundred MHz. Similar to dephasing γ_ϕ, the pure rate is indicated in the inset.

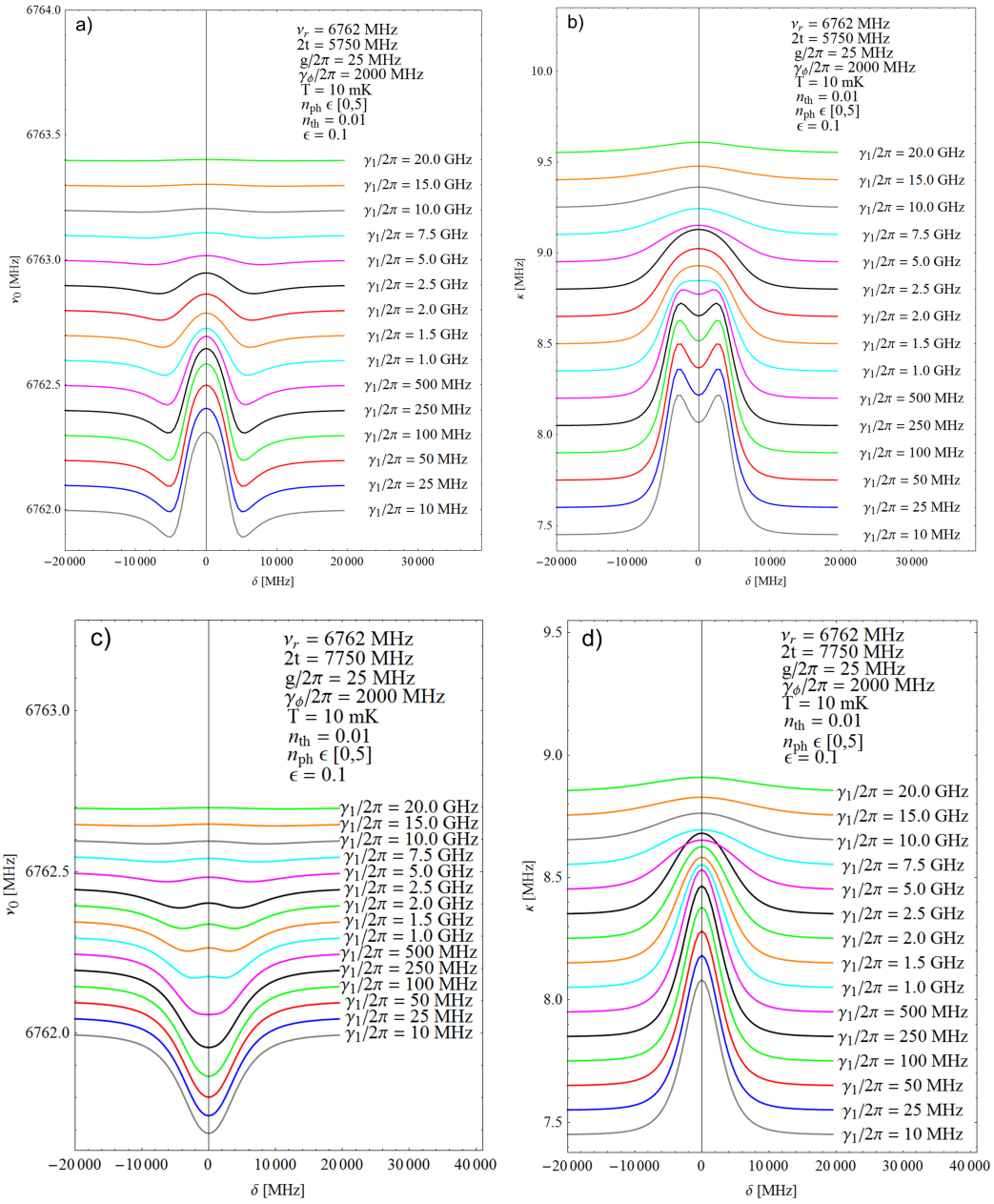

Figure 41: Resonator frequency shift (a),(c) and linewidth (b),(d) for two different tunnel rates t as a function of relaxation rate. $2t < \nu_r$ (a) and (b) resp. $2t > \nu_r$ (c) and (d). An offset of 100 kHz resp. 150 kHz to subsequent curves was added for clarity

5.5.5 Drive amplitude ϵ and qubit temperature T

The model includes a drive of the resonator by an external coherent field (cf. Eq. (16) for the drive in the Hamiltonian). The drive amplitude ϵ accounts for the strength of the drive and thus is proportional to the output power at a microwave generator. In the experiment, -14 dBm were applied. This corresponds to approximately 4.75 photons, taking -106 dBm for all attenuators down to the resonator, a resonator frequency of 6.76 GHz and $\kappa = 7.48$ MHz into account. We checked in the experiment that the data is independent of the drive field for the power applied and less. We also checked in the numerical simulation that the frequency shift remains unaffected for drive amplitudes between $\epsilon = 0.001$ and 10 (cf. Fig. 43a). However, there is a change in the linewidth from $\epsilon = 1$ to $\epsilon = 10$. Close to zero interdot detuning δ, the linewidth decreases for $\epsilon = 10$, a feature that was never observed in the experiment.

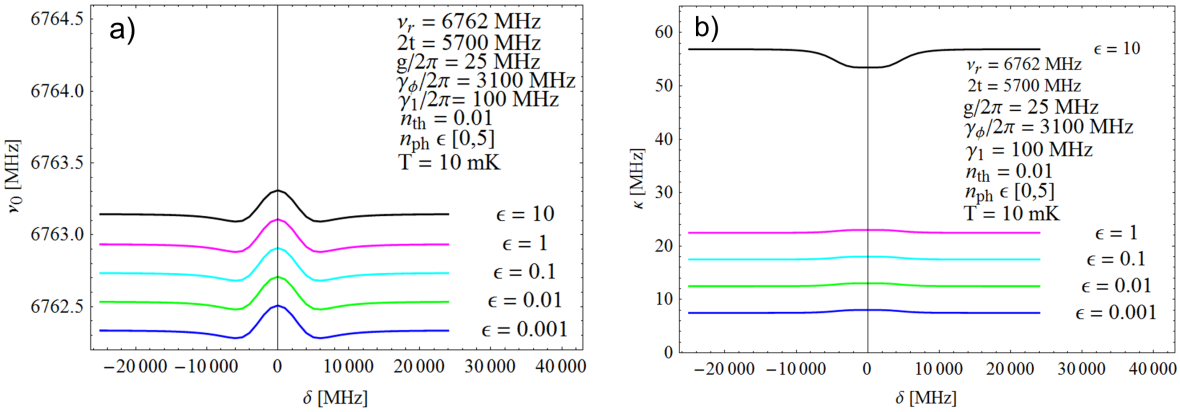

Figure 42: Resonator frequency (a) and linewidth (b) for different drive amplitude ϵ. Up to $\epsilon = 1$, no sensitive effects are visible. A constant offset of 200 kHz (a) respectively 5 MHz (b) was added for clarity

Fig. 42 shows the temperature dependence of the qubit from 0.1 mK to 10 K. The characteristics stay mainly unaffected up to 100 mK from where on degradation of the signal takes place while the overall shape stays maintained.

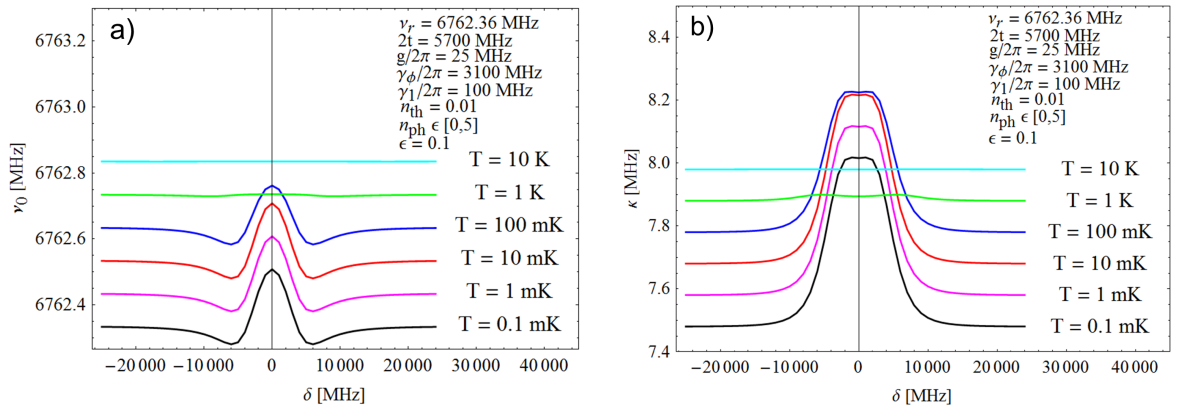

Figure 43: Resonator frequency (a) and linewidth (b) for different qubit temperature T. A constant offset of 100 kHz was added for clarity. Remaining parameters stated in the inset

5.6 Numerical simulation: Comparison to experimental data

In the following, experimental results on the resonator resonance frequency and linewidth in the vicinity of an interdot charge transfer line are compared with a numerical master equation simulation, based on the previously discussed results. Comparing single and many electron regime, conclusions on qubit dephasing rates are drawn.

5.6.1 Single electron DQD

A study of the resonator frequency and linewidth for different detuning δ close to the interdot charge degeneracy point, allows to compare experimental results with data obtained from numerical simulations and thereby to extract characteristics of the coupled system such as interdot tunneling t and qubit dephasing rate γ_ϕ. All measurements were carried out at 10 mK in a dilution refrigerator with microwave input power -14 dBm which corresponds to approximately 4.75 photons in the resonator, taking an attenuation of -106 dB into account. It was checked that the measurement results were independent of the applied microwave power or lower values. The integration time was set to (20*16384) μs for each data point.

Similar to the measurements described previously, the resonator was probed for different qubit detuning δ, i.e. along the red dashed line in Fig. 44. The measurement was repeated for different interdot tunnel coupling, i.e. for different voltages applied to the center gate V_c. For consistency, the position of the red dashed line was chosen in each case to cut the charge transfer line at $\Delta V_{LPG} = 1$ mV, measured from the bottom left edge, as depicted in Fig. 44 by the yellow line. This position was chosen in favor of the center point to avoid for close-lying resonances that are independent of the DQD charge state (cf. section 6). For each point along δ, a full transmission spectrum was recorded. The squared transmission amplitude was fitted by a Lorentzian function. A fit of the spectrum, similar to the procedure described in *2.2 Resonator Design*, allowed to extract parameters of the resonator. Fig. 45 shows data sets for resonator frequency and linewidth, measured along δ for different interdot tunnel rates respectively V_c (CG). Given by the red lines are results from numerical simulations, which reasonably well fit to the experimental data. A lever arm of $\alpha = 0.08$ eV/V was used for energy calibration, which best reproduces simulated results and agrees with previous and independent measurements of $\alpha_{LPG} = 0.12 \pm 0.04$ eV/V (cf. *3.3 Transport in non-linear regime*). The data was centered around $\delta = 0$ MHz, implying that the maximum of frequency shift and linewidth is observed at zero interdot detuning. A slope was subtracted from each curve. This slope is assumed to result from the resonator dependence on the applied top-gate voltage, i.e. the size of the depletion

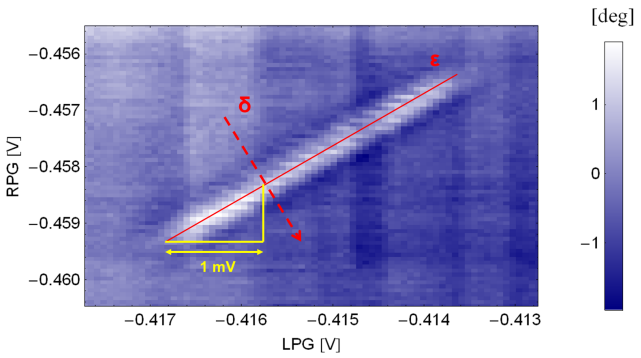

Figure 44: The system was characterized by measuring a transmission spectrum along the red dashed line, exemplarily shown for V_c = -301 mV (cf. Appendix B [A8] for all parameters)

region below the resonator gate, which is discussed in more detail in section *6 Influences of 2DEG on resonator characteristics.*

Each data set was simulated separately. For each, the parameters interdot tunneling t, accounting for different V_c and pure dephasing rate γ_ϕ were adjusted to best fit the experimental data. We independently extracted a coupling strength of $g/2\pi = 25$ MHz from a DC measurement of lever arms and from numerical simulations that give reasonable agreement with experimental results. A set of all parameters used for the numerical simulation is listed in Table 1 for different center gate voltages V_c.

Center gate voltage (V_c)	Qubit min. trans. frequency (2t)	Qubit dephasing rate ($\gamma_\phi/2\pi$)
-292.0 mV	13.0 GHz	0.4 GHz
-294.0 mV	10.4 GHz	0.7 GHz
-296.0 mV	9.0 GHz	1.0 GHy
-297.0 mV	7.5 GHz	1.25 GHz
-297.5 mV	6.85 GHz	2.0 GHz
-298.0 mV	6.7 GHz	2.85 GHz
-298.5 mV	5.7 GHz	3.1 GHz
-299.0 mV	5.4 GHz	3.4 GHz
-300.0 mV	5.25 GHz	3.5 GHz
-301.0 mV	5.0 GHz	3.75 GHz
-302.0 mV	4.75 GHz	4.75 GHz
-304.0 mV	4.15 GHz	5.1 GHz
-306.0 mV	3.2 GHz	5.8 GHz

Table 1: Simulation parameters, corresponding numerical simulations are shown in Fig. 46. Further parameter: $g/2\pi = 25$ MHz, $\gamma_1/2\pi = 100$ MHz, $n_{th} = 0.01$, $n_{ph} \in [0, 5]$, $\epsilon = 0.1$ MHz, T = 10 mK, refer to Appendix B [A15] for a set of all gate voltages

Fig. 45 shows dephasing rates as a function of the minimal qubit transition frequency 2t which were obtained from the simulation. Error bars were included to indicate a range for γ_ϕ which reasonably reproduces the data by eye. Note that the parameters were extracted to achieve a good agreement with experimental data, estimating a coupling strength $g/2\pi = 25$ MHz and qubit relaxation $\gamma_1/2\pi = 100$ MHz, typical for charge qubits [12] and might vary for different parameters. This becomes evident from the analysis in section 5.6 that showed similarities between different parameters chosen. However, there seems to be a tendency in the simulated data for dephasing rates to increase with decreasing interdot tunneling. This behavior is not yet understood.

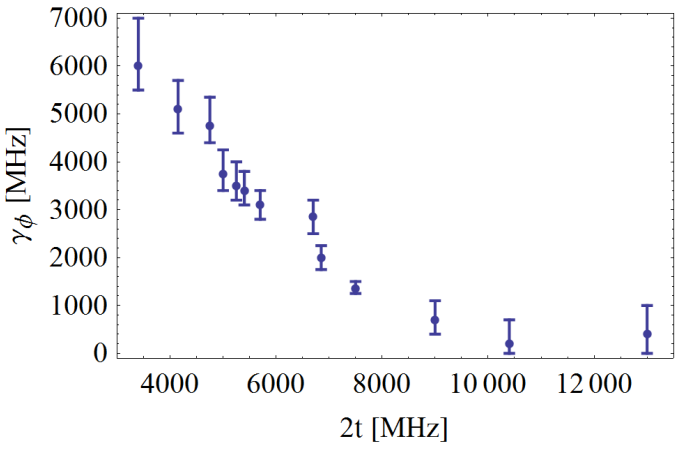

Figure 45: Dephasing as a function of the tunnel rate for different V_c, as stated in Table 1. Compare also Appendix E for inhomogeneous rates.

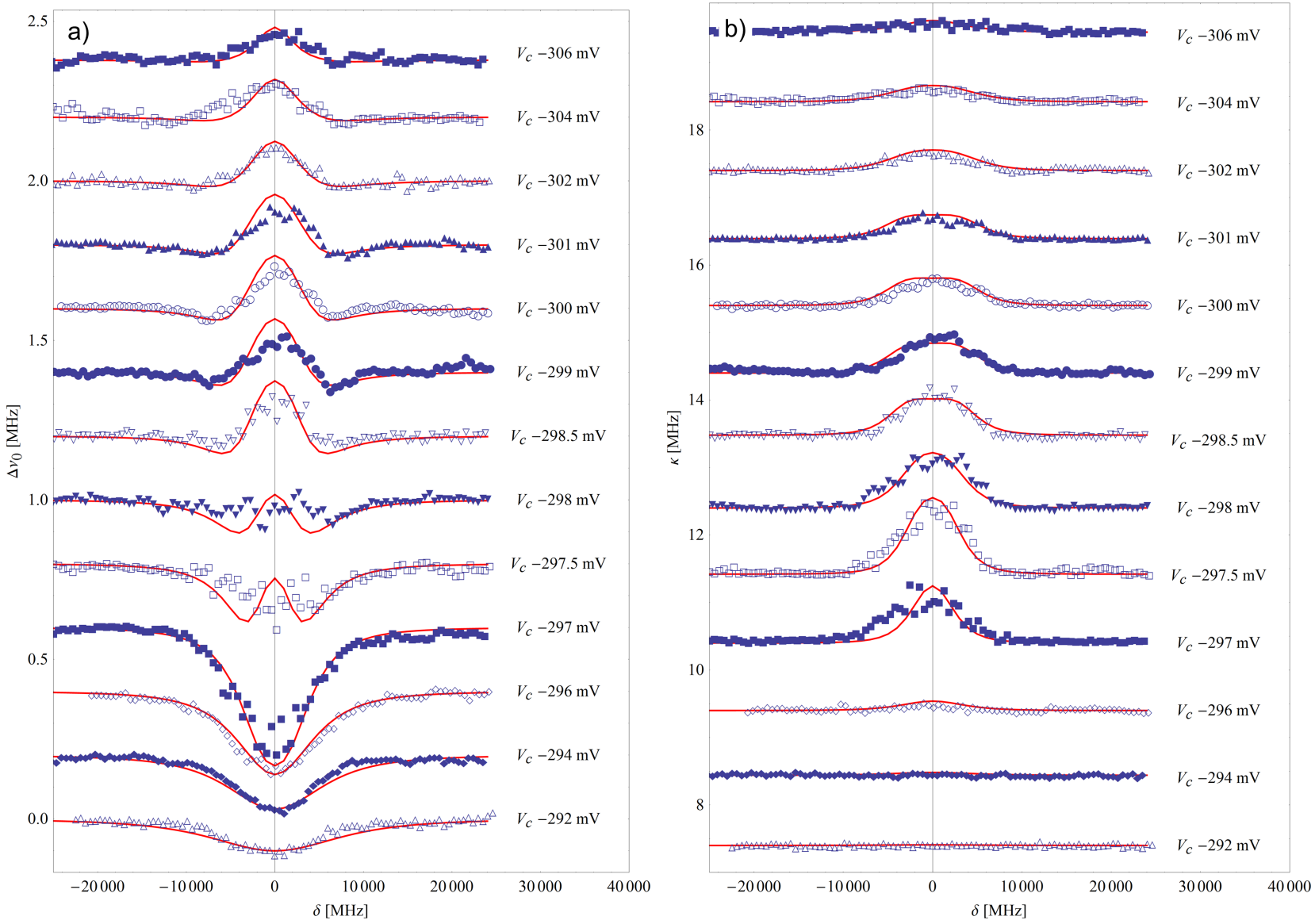

Figure 46: Evolution of the resonator frequency shift (a) and linewidth (b) for different center gate voltage (V_c) as a function of interdot detuning δ. Blue data points show experimental data while red lines give best results from a numerical simulation. Simulation parameters are stated in Table 1. Please refer to Appendix B [A15] for a full set of parameters.

5.6.2 Many electron DQD

It is interesting to compare the single with the many electron regime. Both measurements are done in the same sample which possibly allows to check for effects of close-spaced excited states on dephasing rates. We repeat the measurements described in the previous section in the many electron regime. Contrary to the single electron regime, the center of a charge degeneracy line was chosen to measure for zero detuning δ (cf. Fig. 44), while the resonator was probed with approximately 4.75 photons and integration time (20*16384) μs, identical to the single electron regime. Fig. 48 summarizes results for sets of different interdot tunnel rates respectively center gate voltages V_c. Red lines show data obtained from a numerical simulation that reproduces the data reasonably well. A coupling strength of $g/2\pi = 50$ MHz was estimated from the simulation data by minimizing the normalized square deviation between experimental and simulated data for V_c = -523 mV and different g. A larger coupling strength, in comparison to the single electron dot, is reasonable, suggesting a double quantum dot larger in size. Identical to the single electron dot, tunnel rates and dephasing were varied for the simulated results to agree with experimental data reasonable well (Table 2).

Center gate voltage (V_c)	Qubit min. trans. frequency (2t)	Qubit dephasing rate ($\gamma_\phi/2\pi$)
-518 mV	12.5 GHz	2.0 GHz
-521 mV	10.5 GHz	2.8 GHz
-523 mV	9.75 GHz	4.75 GHz
-525 mV	7.65 GHz	4.0 GHz
-526 mV	6.4 GHz	5.5 GHz
-527 mV	5.85 GHz	6.5 GHz
-528 mV	5.25 GHz	9.0 GHz
-529 mV	4.3 GHz	10.0 GHz
-530 mV	4.3 GHz	10.0 GHz
-531 mV	3.2 GHz	11.5 GHz
-538 mV	0.75 GHz	17.0 GHz

Table 2: Further parameter: $g/2\pi = 50$ MHz, $\gamma_1/2\pi = 100$ MHz, $n_{th} = 0.01$, $\epsilon = 0.1$, T = 10 mK, refer to Appendix B [A16] for a set of all gate voltages

Similar to the single electron case, Fig. 47 shows a tendency of γ_ϕ to increase with decreasing tunnel rate. Error bars were included to indicate a range for γ_ϕ that still reasonably well reproduces the data by eye. The parameters were achieved by ensuring agreement with experimental data (cf. Fig. 48), estimating a coupling strength of $g/2\pi = 50$ MHz and a qubit relaxation $\gamma_1/2\pi = 100$ MHz, typical for charge qubits [12] and might strongly vary for different parameters chosen. A lever arm of $\alpha = 0.18$ eV/V was applied which is in agreement with a lever arm of $\alpha = 0.23 \pm 6$ eV/V extracted from DC measurements in the non-linear regime.

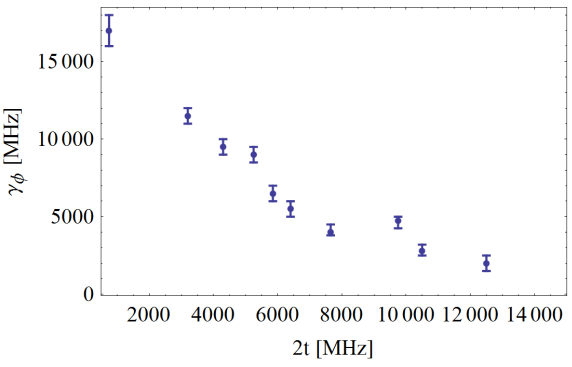

Figure 47: Dephasing as a function of the tunnel rate for different V_c in the many electron regime, as listed in Table 2

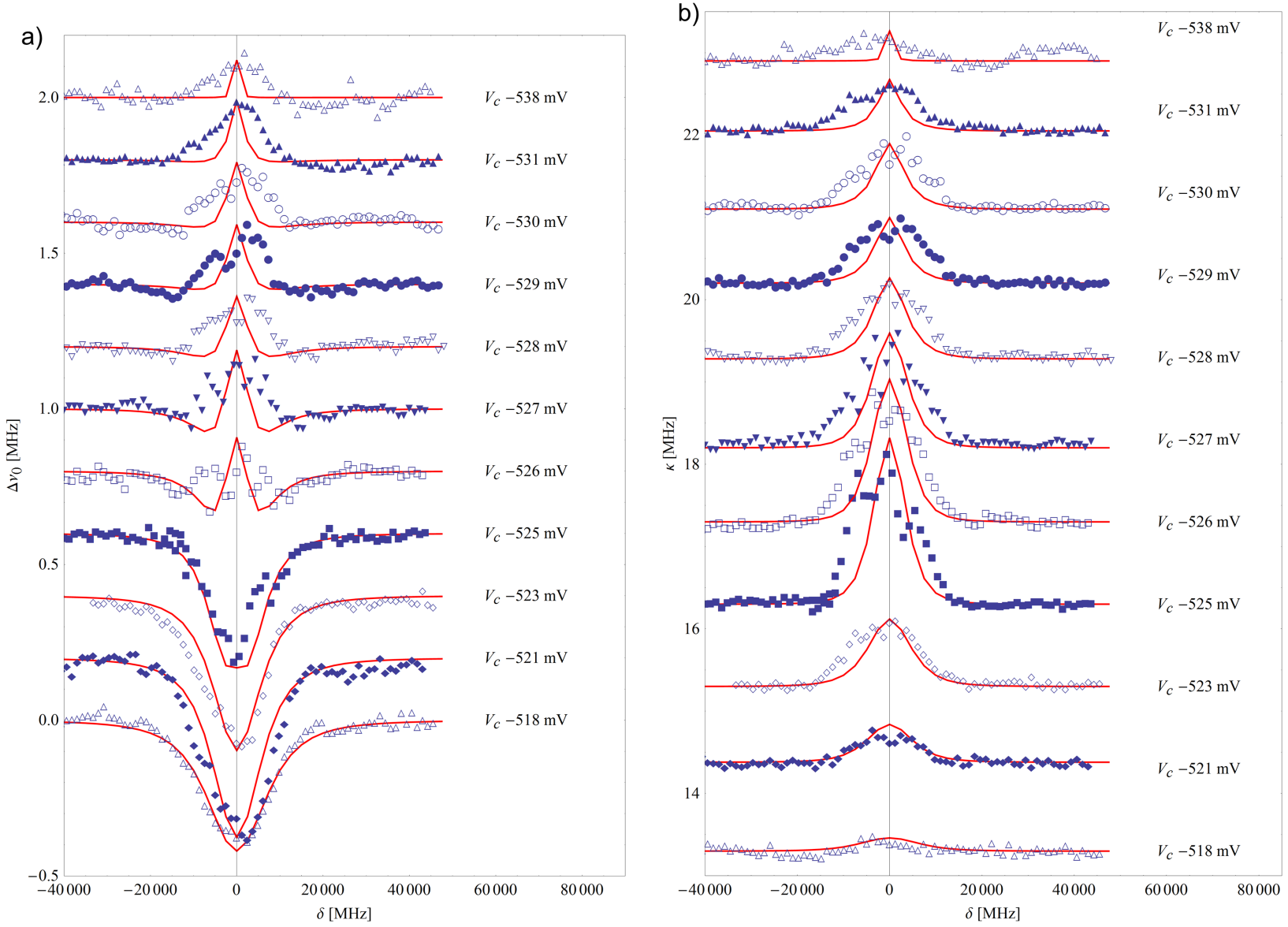

Figure 48: Evolution of the resonator frequency shift (a) and linewidth (b) for different center gate voltage (V_c) as a function of interdot detuning δ. Blue data points show experimental data while red lines give best results from a numerical simulation. Simulation parameters are stated in Table 2. Please refer to Appendix B [A16] for a full set of parameters.

5.6.3 Single versus many electron quantum dot

Fig. 49 summarizes dephasing rates in the single (red) and many (blue) electron regime. In both cases, decoherence rates increase with decreasing tunnel coupling, whereas higher dephasing rates are extracted from the simulated data in the case of the many electron regime. Note however, that a direct comparison is not possible at this stage, as tunnel and dephasing rates strongly depend on the remaining parameters chosen for the simulation. Indeed, it is evident from section 5.5, that different parameters in the simulation have comparable effects. Thus, more information on the simulated parameters is necessary for a more accurate description of the experimental data. Note that different decoherence rates not necessarily result from a possibly decreased coupling to excited states in the single electron dot. Other effects are thinkable, e.g. a different coupling of gate noise as a result of different lever arms in the single and many electron dot.

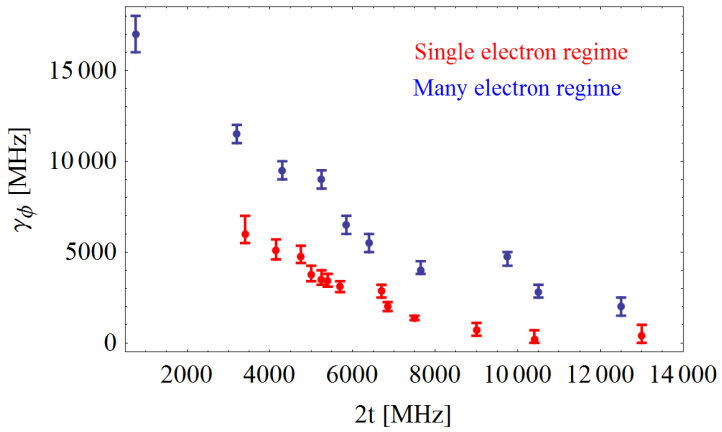

Figure 49: Dephasing as a function of the interdot tunnel rate for the single (red) and many (blue) electron regime. Shown are parameters that are used in numerical simulations, depicted by the red lines in Fig. 46 and 48.

5.6.4 Conclusion on numerical simulations

Comparing numerical results with experimental data allowed to estimate tunnel rate, dephasing and coupling strength. However, a pre-analysis showed that various parameters have comparable effects and a similar agreement might be achievable with experimental results for a set of different parameters. In fact, the choice of simulation parameters, other than t and γ_ϕ, relied on estimates from direct current measurement in combination with a comparison between numerical and experimental results (coupling strength g), typical characteristics of charge qubits (relaxation rate γ_1) and estimates on the setup (e.g. drive amplitude ϵ, temperature T). Thus, more accurate information on the system to further reduce the number of free parameters is necessary. One possibility might be to extract tunnel and charge relaxation rate from microwave spectroscopy or direct current measurements, e.g. from a measurement similar to the one suggested in reference [30, 44]. Such a measurement would be possible in the currently employed sample, although it is uncertain to which accuracy these parameters can be determined. Ongoing measurements on this sample try to extract tunnel coupling directly from QPC transconductance similar to [44].

5.7 Decoherence

Simulations, in reasonable agreement with the experimental results, show decoherence rates comparable to previously published work by Frey *et al.* [12], reporting on pure dephasing rates between 0.9 and 3.3 GHz for charge qubits in GaAs quantum dots. In this work, we analyzed coherence properties in the single electron regime, which were found to be comparable to dephasing rates observed in a many electron quantum dot, although the simulation suggests less dephasing within the same sample. However, coherence times stay low and remain a major obstacle on the way to strong coupling. There are various sources of decoherence in GaAs quantum dots, which have been discussed theoretically and experimentally in the past:

Excited states
Excited states might serve as an additional decoherence channel when electrons couple and hybridize with higher energy levels. In single electron dots, smaller in size than dots containing many electrons, energetically higher quantized states are further separated in energy (cf. section 3.1), which reduces coupling to those. Indeed, the previously discussed experimental data might give some evidence for this theory, although decoherence rates still remain large. A measurement of the coherence times in a one-electron GaAs double quantum dot by Petersson *et al.* [45] reports on a minimal decoherence rate of 140 MHz at the charge degeneracy point. Excited states thus might not be the major source of decoherence. Nevertheless, single electron DQDs have the benefit of a simpler qubit level structure when a hybridization with excited states is small and many-particle effects can be neglected.

Phonon decoherence
An electron that moves between charge states in the left and right dot, creates and annihilates phonons by its motion [50]. A coupling of the electron to those and other phonon modes, additionally reduces the coherence time. Vorojtsov *et al.* [50] suggest a theoretical model in which the coupling to phonons is proportional to the number of excess electrons in the respective dot, favoring single electron dots. However, phonon decoherence is reported to be not a major source of dephasing in this model and in comparison to experimental data. Vorojtsov *et al.* further suggest that background charge fluctuations and electromagnetic noise on top-gates might reduce coherence.

Electromagnetic field fluctuations
An additional source of decoherence may be fluctuations in the voltage applied to top-gates that possibly result from fluctuations within the voltage source or thermal noise. Recently suggested by Valente *et al.* [51], a theoretical model on voltage fluctuations estimates that those contribute only insignificantly. Furthermore, the model states that a strong intercapacitive coupling between gates enhances decoherence such that it is favorable to keep top-gates as isolated as possible with respect to each other. Although this mechanism might not be the dominant decoherence effect, voltage fluctuations on gates can be reduced in the setup by more stable voltage sources (cf. Appendix C for Microwave setup), cables that filter low-frequency noise or voltage dividers that allow to operate voltage sources at higher output voltages, thus reducing fluctuations when scaling down the output signal in a second step.

Fluctuating Background Charges
It is assumed that an electrostatic coupling to background charges, fluctuating in time, significantly contributes to dephasing [52, 53]. This might happen through a hybridization of quantum dot charge states with fluctuating background charges (FBC) that are due to random recharging processes of trap centers within the solid close to the quantum dot and create dynamical electric fields i.e. electrostatic potential fluctuations. A dynamic change in the electric field, caused by recharging process, might additionally contribute to dephasing. It was found that an ensemble of randomly distributed FBC centers, respectively its spectral density, resembles low-frequency $1/f$ noise in charge qubits [52, 54, 55], while the spectrum of single two-level charge fluctuators is Lorentzian, i.e. shows a $1/f^2$ dependence in its spectrum, resulting random telegraph noise [52]. Indeed, experiments have shown pronounced charge fluctuations, when directly measuring the conductance by means of a QPC, and a $1/f$ respectively $1/f^2$ dependence of the noise spectrum [56]. Various defect centers are proposed for FBC such as defects within the remote impurity layer forming the dopants, DX centers or defects close to the active region forming the dot. So far, only DX centers were shown to be non-dominant in terms of charge noise [56]. Additionally, it was suggested by Yurkevich *et al.* [53] that direct electron-electron interactions via a short-range Coulomb field enhances the effect of FBC dramatically, which favors a theory that defects close to the active dot region contribute most to charge noise. Yurkevich further suggests that charge fluctuations are the most dangerous mechanism for decoherence in charge qubits [53]. It might be fruitful to analyze different wafer-designs in terms of decoherence properties of charge qubits and to further study the currently employed wafer architecture in term of charge noise and decoherence mechanisms.

Leakage of charges from electrodes
Additionally to the previously discussed noise source which is inherent to the material, electrons might directly leak from top-gates into the semiconductor underneath and become trapped near the dot and/or subsequently tunnel from trap centers into the 2DEG [56]. Leakage can experimentally be reduced by pre-biasing the sample gates during the cool-down process [56]. Pre-biasing the sample during cool-down, electrons remain frozen in deep traps (DX centers) when the bias is removed. Given the potential landscape due to those additional electrons, less negative voltages at top-gates are necessary to form and operate a quantum dot. As a result leakage of electrons from the gate to 2DEG is reduced by means of a decreased potential difference in comparison to the case without pre-biasing. A noise reduction was observed experimentally in pre-biased structures [56, 57]. Note however, that pre-bias cooling was applied for all experiments presented. During the cool-down, all gates except for the left and right plunger gate, were biased at V = +300 mV. Nevertheless, high decoherence rates were evident.

6 Influences of 2DEG on resonator characteristics

Independent of the charge state of the dot, a change in amplitude and phase has been observed in LPG-RPG subspace which goes along with static resonances that are independent of the voltage applied to the right plunger gate, shown in Fig. 50. The following section discusses this observed dependency, suggest a model to understand the behavior and propose a way to improve the next sample generation. Note that in this section a DQD is not necessarily formed whereas difficulties with the gate design are discussed.

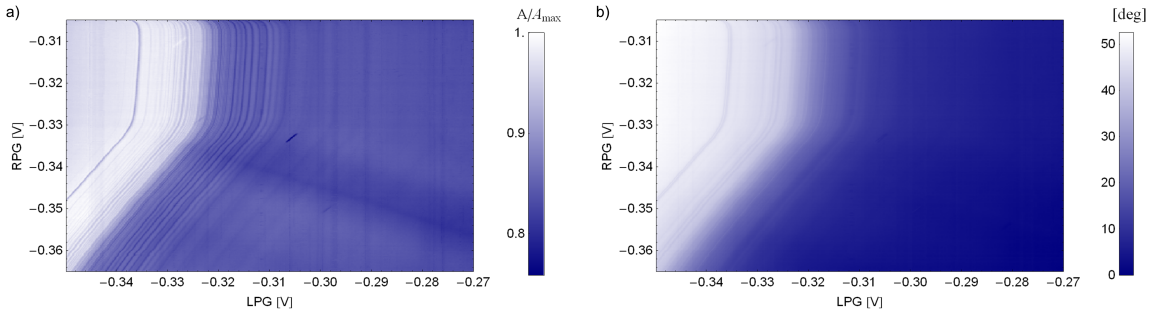

Figure 50: Transmission amplitude (a) and phase (b), full set of parameters in [A10]

In Fig. 50, a change in amplitude and phase seems to depend strongly on the voltage applied to the left plunger gate, while the change is first independent of voltage applied to the right plunger gate up to RPG $\simeq$ -330 mV. Note that LPG is the resonator gate. This suggest a dependence of the resonator characteristic on applied top-gate voltage, which is more systematically analyzed in the following.

6.1 Resonator transmission spectrum

Fig. 51 shows transmission spectra as a function of the voltage applied to the left plunger gate, while all other top-gates are held at a constant voltage. From such a measurement, we conclude that the change in transmission amplitude and phase, observed in Fig. 50, might be related to a change in resonator frequency as a function of the left plunger gate voltage. Indeed, in Fig. 50, the resonator is probed at a fixed frequency and the transmitted microwave signal becomes off-resonant what can be observed in a changed transmission amplitude and phase. Furthermore, the measured transmission spectra show that the voltage at LPG, for which the transmission signal changes, is not constant but depends on the voltage applied to the remaining gates. Fig. 52 gives the position in LPG space at which the transmission signal significantly changes in amplitude and phase as a function of the voltages applied to all remaining top-gates. Also given is an envelope which indicates the width over which these changes appear. The data were obtained by measuring the transmitted signal at fixed resonator frequency. The choice of the frequency is shown exemplary by the dotted red line in Fig. 53a, whereas Fig. 53b gives the transmission amplitude along such a line. The resonator transmission changes significantly within the blue region in Fig. 53b. Note that the values for blue region and red data points in Fig. 52 were obtained from a measurement similar to Fig. 53b. The red point corresponds to the mean value (m) within the surge, while the blue region gives start (s) and end (e) point. However, note that such a study depends on the measurement frequency and may only serve as an estimation on the position.

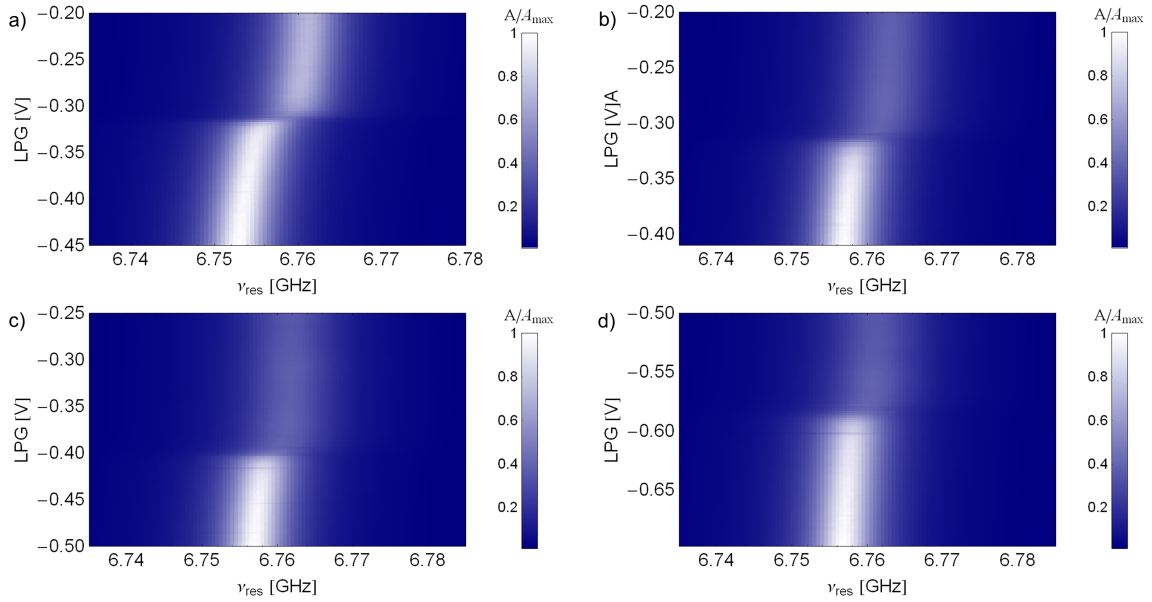

Figure 51: Resonator transmission spectrum as a function of V_{LPG}. Remaining top-gates at voltage 0 V (a) [A17], -0.2 V (b) [A18], -0.5 V (c) [A19] and -0.8 V (d) [A20]. Depending on the gate configuration, a transition appears at unequal values for V_{LPG} (see Fig. 52)

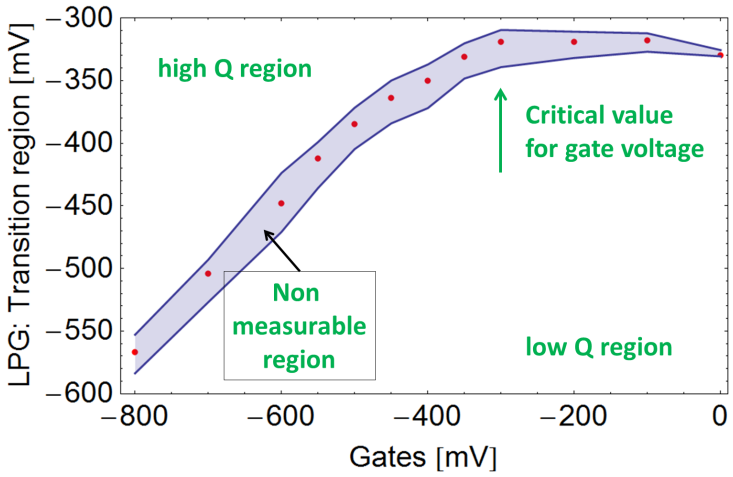

Figure 52: Position in LPG-space over which resonator characteristics change as a function of the voltage applied to remaining top-gates

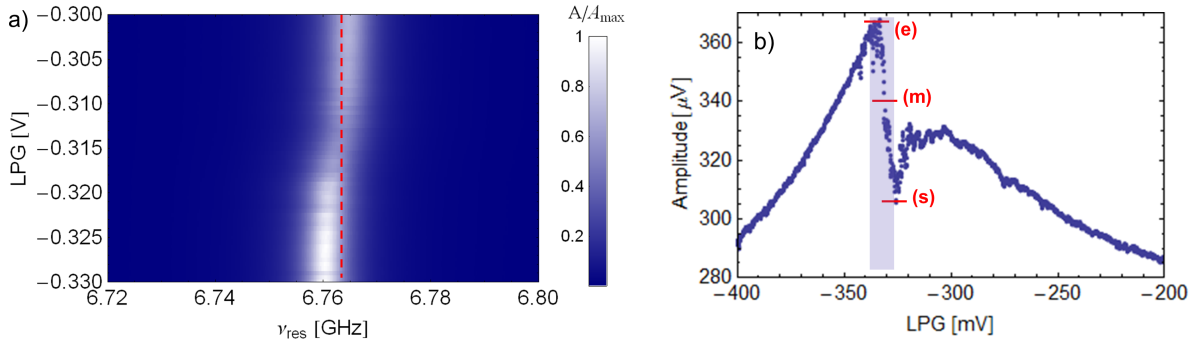

Figure 53: Transmission spectra as a function of the voltage applied to the left plunger gate (a). Transmitted amplitude for fixed resonator frequency (b) for a measurement depicted along the red dashed line in (a). A full set of parameters is available from Appendix B [A21]

6.2 Resonator regimes

A change in resonator characteristics appears continuous in Fig. 53a. Additionally, the transmitted signal shows a decreasing amplitude in this transition region. In the following, the resonator response is studied by a Lorentzian line fit similar to section 2.2. In each case, the full transmission spectrum for the fundamental mode was measured at different voltages applied to the left plunger gate, while all remaining top-gates were held at constant potential. A summary of the fitted resonance frequencies as well as the frequency shift $\Delta\nu$ is shown in Fig. 54 as a function of the left plunger gate voltage. The spectra were recorded for all dot gates set to 0 V, except for LPG.

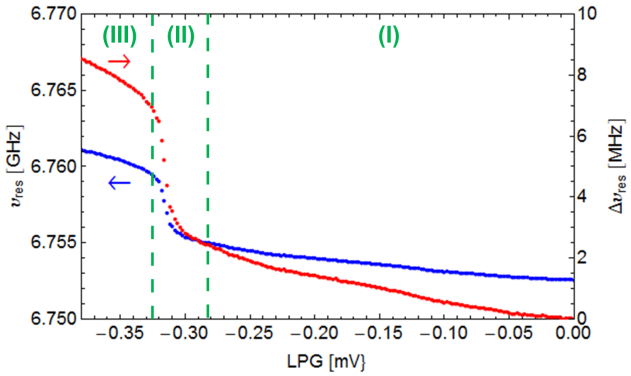

Figure 54: Resonator resonance frequency extracted from a Lorentzian line fit. Each point corresponds to data obtained from a full transmission spectrum. The voltage for the resonator gate LPG is changed while all remaining dot gates were held at 0 V. The resonance frequency (blue) and relative frequency change (red) are shown. Parameters in Appendix B [A21].

The plotted data show schematically three characteristic regimes (I) - (III) that can be understood from a capacitance model:

Starting from LPG equal to 0 V, the applied voltage is successively set more negative in region (I) whereby the potential landscape for electrons in the 2DEG underneath changes. In region (II), electrons below the gate are assumed to become depleted except for localized charge states that remain below the gate. In region (III), electrons are completely depleted below the gate and the depletion region is widened when applying more negative voltage. The shift in resonance frequency can then be explained by a capacitive effect. For more negative voltages applied to the resonator gate LPG, the effective 2DEG area underneath changes. The capacitance C between LPG and 2DEG decreases successively as C is assumed to scale with the effective electron gas area, similar to a plate capacitor. A change in capacitance however comes along with a different admittance of the 2DEG, similar to a measurement described in Fig. 17. The resonator probes the complex admittance of the coupled sys-

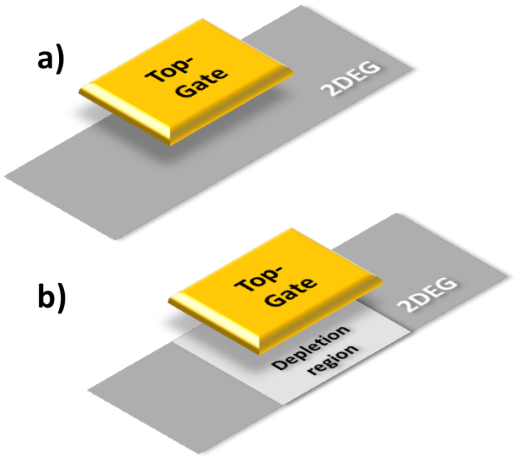

Figure 55: Capacitive change due to a change in the effective 2DEG area for region (I) shown in a) and (III) shown in b)

tem and thereby is sensitive to changes in capacitance. A frequency shift might thus be explained as a dispersive effect. Studying the resonator linewidth $\delta\nu$ respectively quality factor Q for the fundamental mode, similarly shows three characteristic regions:

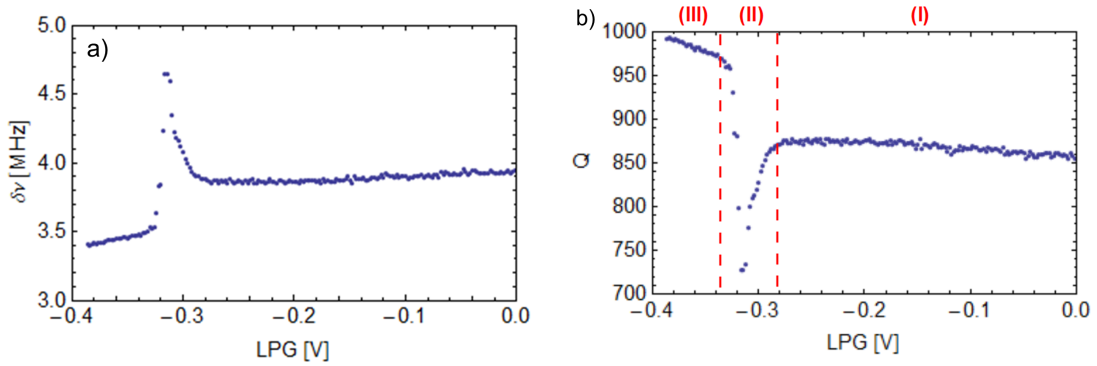

Figure 56: Resonator linewidth and quality factor extracted from a Lorentzian line fit. Each point corresponds to data obtained from a full transmission spectrum. The voltage for the resonator gate LPG is changed while all remaining gates are at 0 V. The resonator linewidth (a) and quality factor (b) are shown. A full set of parameters is listed in Appendix B [A21]

Region (I) again corresponds to a case in which the voltage applied to the resonator gate is successively set more negative which changes the potential landscape for the electron gas underneath and thereby reduces the density of electrons. However, the 2DEG is not yet depleted below the resonator. A dissipative channel between resonator gate and 2DEG remains. This results in a lower quality factor respectively larger linewidth of the resonator than initially designed for. In region (II), the electron gas underneath depletes. In this transition regime, localized islands of charges are assumed to remain below the resonator gate. The quality factor is further decreased in this region. It is assumed that resonator excitations shuffle electrons between localized island. The energy necessary for those processes might be provided throughout the resonator gate what results in a strongly dissipative process. Region (III), where all electrons are depleted, shows a significantly higher quality factor compared to (I) and (II). A lossy channel from resonator to 2DEG is reduced and the quality factor increased.

The assumption of a lossy channel into the 2DEG and thereby dissipative processes from the resonator is likewise in agreement with the amplitude obtained from each line fit (cf. Eq. (1)). The transmitted signal is significantly lower in region (I) compared to (III), which well agrees with the previous explanations. The additional drop in region (II) is again attributed to localized charge islands which serve as an additional dissipative channel. The assumption of localized charge islands in and close to region (II) might also be the reason for resonances that were observed close to the kink in Fig. 50 shown previously. Localized islands in mesoscopic structure might

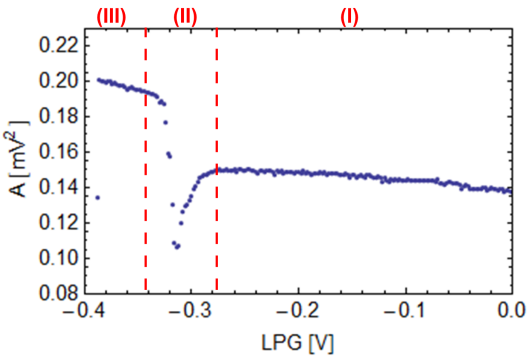

Figure 57: Resonator amplitude at resonance. The voltage for resonator gate LPG is changed while all remaining gates remain at 0 V

provide quantized charge states with transition frequencies at or close to the resonator frequency. The resonator therefore might excite electrons in those puddles (region II). For more negative LPG, those islands are emptied and additional resonances disappear (region III). On the contrary, puddles do not exist in region (I) in which the 2DEG is not yet depleted. This explains why resonances are predominantly seen in region (II). Note that the voltage applied to remaining gates have no effects on those resonances. This means that one predominantly probes the localization of charge states below LPG.

A measurement similar to the one described in Fig. 53b validates that those resonances are reproducible which additionally provides some evidence for this assumption:

Figure 58 shows a set of three measurement curves that were obtained for identical parameters but at different times. The red and blue curve were obtained within few minutes while the green curve was measured one day after. The position of the frequency change in LPG space is well reproduced as well as the wiggles close-by (red arrows), which correspond to additional resonances. The estimated spacing of 3 mV between resonances translates to an energy difference of 380 μeV assuming a lever arm of 0.12 eV/V. The lever arm was estimated under the assumption that one completely depletes the 2DEG below LPG by changing ΔV_{LPG} over 350 mV. Assuming an electron density of $5*10^{11}$ cm^{-2}, a Fermi wavelength of $\lambda_F = 35$ nm is calculated [58] and thereby a Fermi energy $E_F = 45$ meV. The lever arm α was estimated from the relation $\alpha \Delta V_{LPG} = E_F$.

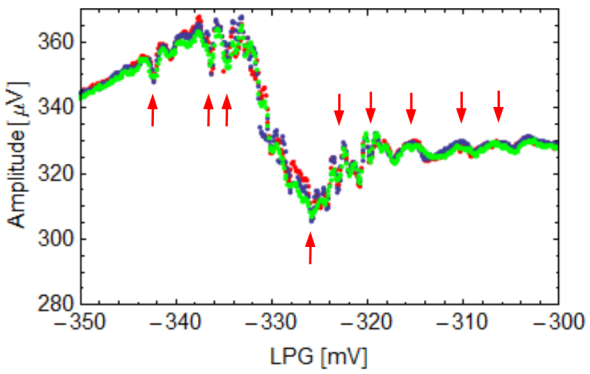

Figure 58: Transmitted amplitude for fixed resonator frequency for a measurement depicted along the red dashed line in Fig. 53a. Parameters cf. Appendix B [A21]

Data presented so far explains qualitatively the change in resonator characteristics as a result of different bias applied to the resonator gate LPG, while all remaining gates are on zero voltage. However, the data discussed so far can not explain all observed phenomena. Indeed, the question of a varying position of the depletion region in LPG space (cf. Fig. 28) remains and will be addressed in the following.

A set of resonator characteristics, obtained for different gate settings, is given in Fig. 59 for resonance frequency and amplitude and in Fig. 60 for resonator linewidth and quality factor. Similar to before, the full resonator transmission was probed for the fundamental mode for different voltages applied to the resonator gate LPG. All remaining gates were held at constant and identical potential. This voltage is exemplary given for the left side gate LSG while it has to be understood as being identical for all remaining gates except for LPG. Refer to Appendix B for a full set of all parameters.

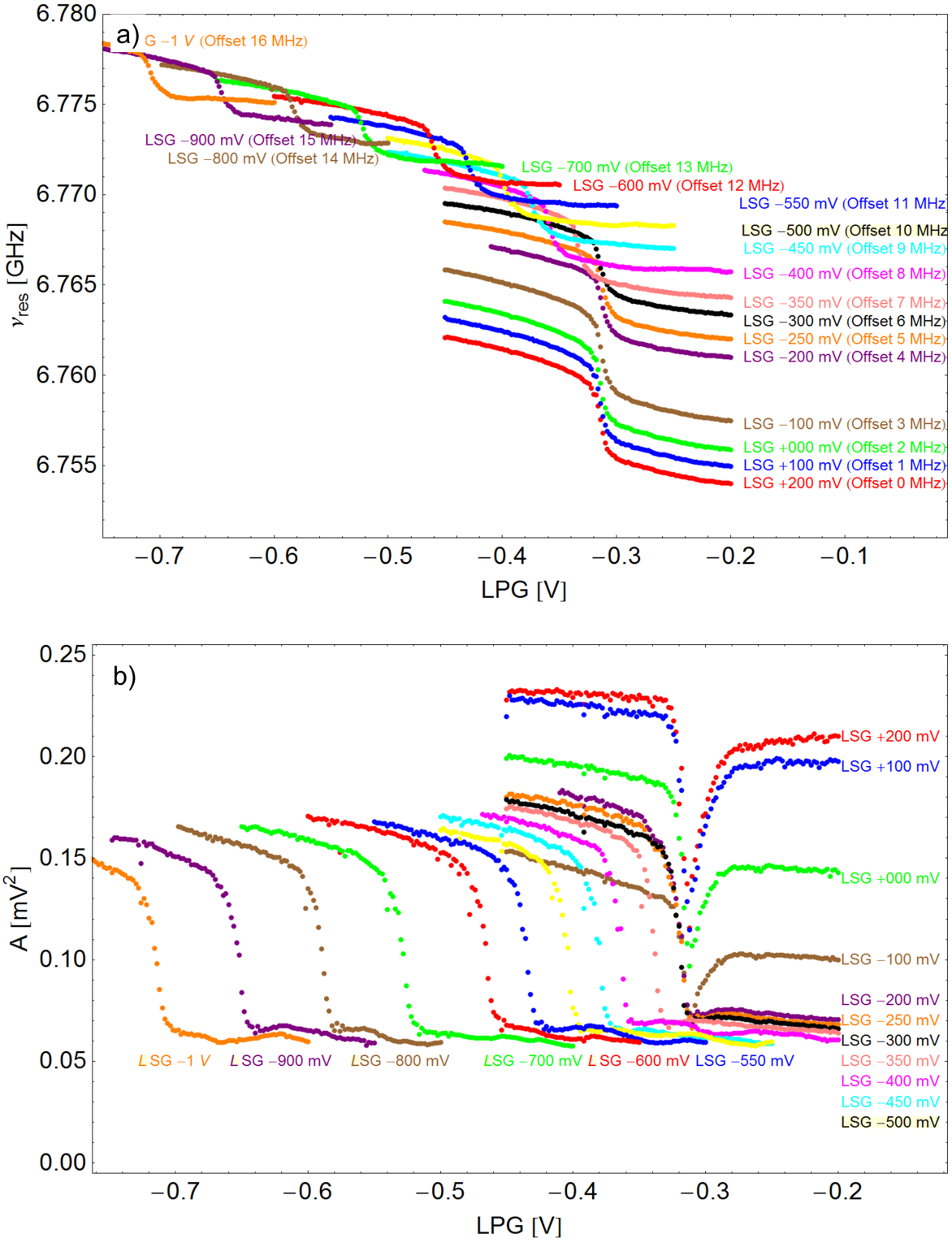

Figure 59: Resonator resonance frequency ν_{res} (a) and transmitted amplitude at resonance A (b) from a Lorentzian line fit. Each point corresponds to data obtained from a full transmission spectrum. The voltage for the resonator gate LPG is changed while all remaining gates were held at constant voltage in each curve. The gate voltage for all remaining top-gates is indicated exemplary for LSG (other gate voltages identical). An offset of n*1 MHz (a) to the resonator frequency was added at the nth curve for clarity. Further parameters in Appendix B [A22]

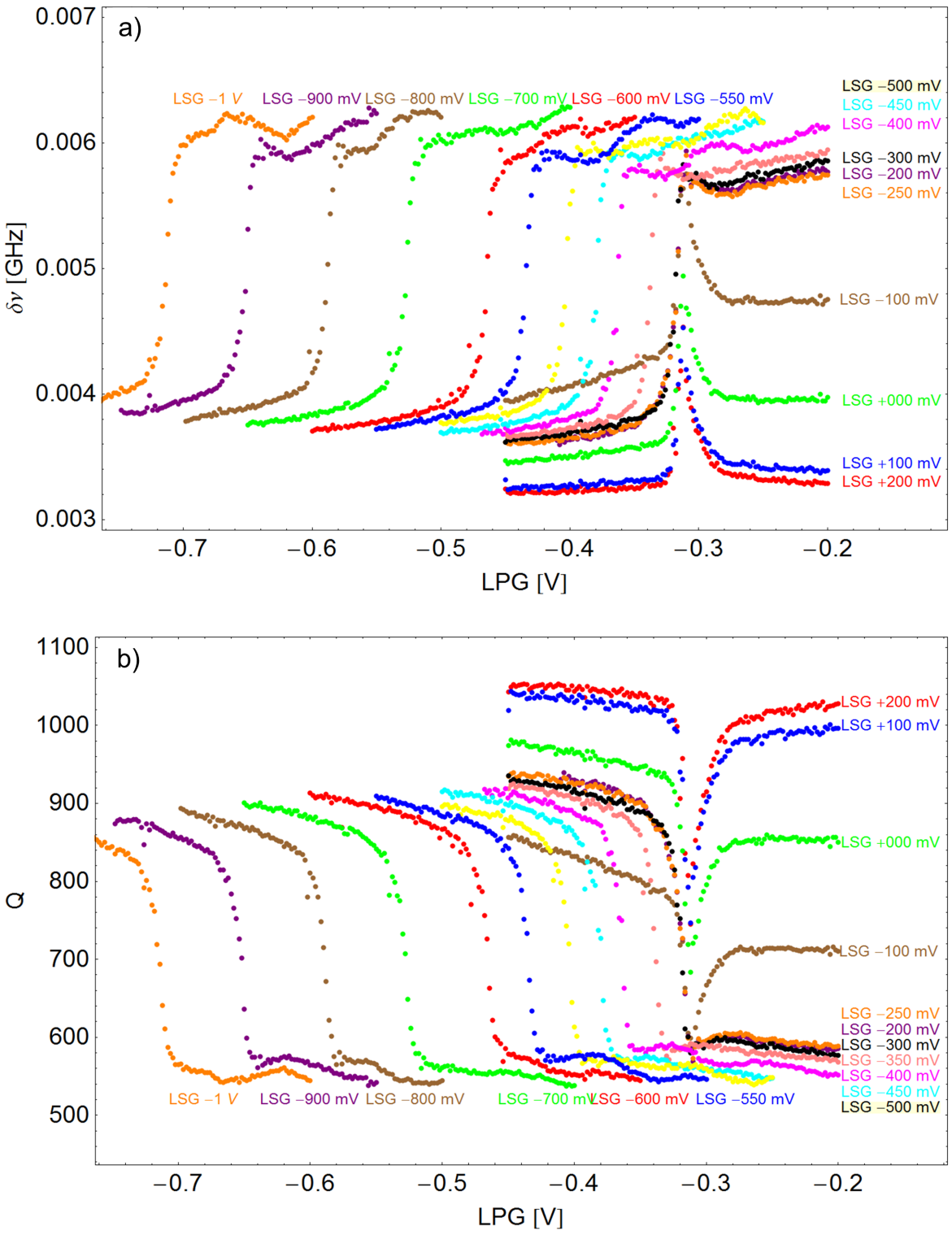

Figure 60: Resonator linewidth 2*$\delta\nu$ (a) and quality factor Q (b) obtained from a Lorentzian line fit. Each point corresponds to data obtained from a full transmission spectrum. The voltage for the resonator gate LPG is changed while all remaining gates were held at constant in each curve. The gate voltage for all remaining top-gates is indicated exemplary for LSG (other gate voltages identical). Further parameters in Appendix B [A22]

The observed phenomena, exemplary described for the quality factor Q in the following, can be attributed to three different regions:

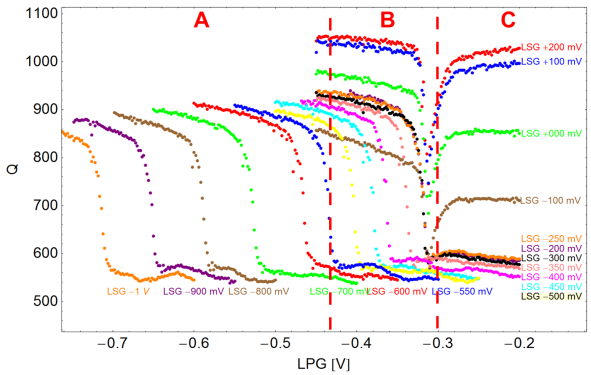

Region A:
$V_{LSG} < V_{LPG}$

Region B:
$V_{LSG} > V_{LPG}$
and $V_{LPG} < -300mV$

Region C:
$V_{LSG} > V_{LPG}$
and $V_{LPG} > -300mV$

Figure 61: Characterstic regions outlined for the resonator quality factor. Refer to Fig. 54b for an enlarged view

6.3 Capacitance model

Resonator characteristics of the different regions can be qualitatively understood from a capacitance model at which the resonator probes the admittance of the 2DEG:

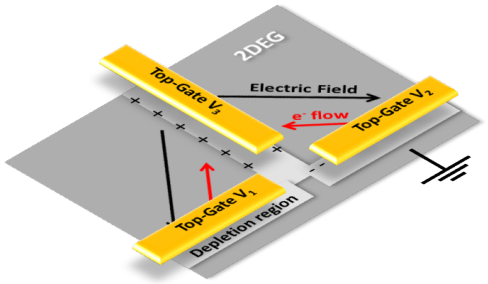

Figure 62: Capacitance model, region A

In **region A**, the top left and right part of the 2DEG become separated from the lower parts. This happens when the voltage applied to top-gates becomes more negative than an estimated value of -350 mV. Gates V_1 and V_2 create a depletion region underneath when exceeding -350 mV such that the upper two parts become isolated, i.e. the upper 2DEG becomes floating and thereby polarizable. Electrons accumulate close to the resonator gate and more negative voltage needs to be applied to reach the depletion threshold voltage. This explains the linear shift of the depletion region in gate voltage applied to LPG (V_3) observed in Fig. 52.

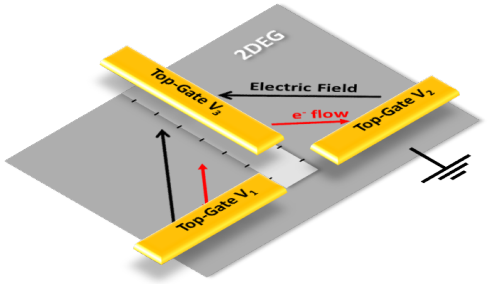

Figure 63: Capacitance model, region B

In **region B**, the voltage applied to V_1 and V_2 is not sufficient to deplete electrons beneath. Correspondingly there is no depletion region below those gates such that the upper parts of the 2DEG are not decoupled from the lower grounded 2DEG, electrons can not accumulate close to the resonator gate V_3 i.e. the 2DEG is not polarizable in such a configuration. However, starting from a voltage of -300 mV applied to LPG (V_3), the 2DEG starts depleting underneath. The depletion threshold voltage on the contrary is now independent from the voltages applied to the re-

maining top-gates, i.e. independent from V_2 and V_3. The position in LPG-space at which the quality factor changes remains the same, seen for LSG = +200 mV to LSG = -300 mV. Furthermore, the voltage applied to V_1 and V_1 is less negative than the voltage applied to LPG (V_3). This creates an electric field between both gates that pushes electrons additionally away from the resonator gate LPG. This explains the higher quality factor in comparison to other regions.

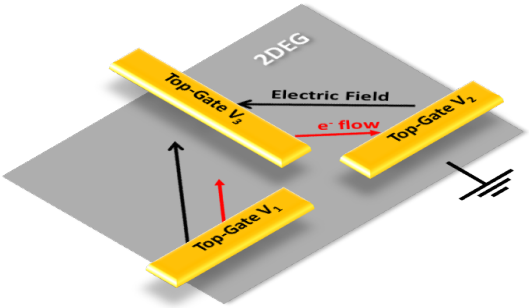

Figure 64: Capacitance model, region C

Characteristic for **region C** are top-gate voltages that are less negative than the threshold voltage necessary to deplete electrons below. All 2DEG regions are grounded via ohmic contacts. However, the voltage applied to V_1 and V_2 is less negative than V_3. A resulting electric field $\vec{E}$ pushes electrons in the 2DEG away from the resonator gate. This explains a higher quality factor in this region. The effect becomes less pronounced for decreasing difference in gate voltages $V_{1(2)}$ - V_3 which is in agreement with considerations on an electric field. There is a strong effect on the quality factor for $V_3 \gg V_{2(1)}$. The quality factor becomes comparable to quality factors observed in other regions when V_3 approaches $V_{2(1)}$ what becomes evident at around -300 mV.

What remains is to cross-check the hypothesis of a decoupled and floating 2DEG region from the grounded electron gas reservoir:

6.4 Consistency check: Floating 2DEG

In the following, the two dimensional electron gas is successively depleted below different top-gate combinations to check against the hypothesis of a decoupled and floating 2DEG. Please refer to Fig. 4 for the geometry and position of all top-gates used in the following.

Step 1: Source Drain Barrier (SDB)
In a first step, the transmission amplitude is probed as a function of the voltage applied to the resonator gate LPG. The measurement is carried out for fixed frequency whereby the frequency was chosen to have a good signal at mean when sweeping LPG. This is similar to the case discussed previously in Fig 53a in which the red dotted line indicates the chosen resonance frequency. During this measurement, SDB was set more and more negative in steps of 50 mV. SDB and LPG have no effects in terms of decoupling 2DEG areas from ground (cf. Fig. 4). The area stays well connected and no effect on the transmission amplitude becomes apparent in Fig. 65. This observation is consistent with the previous interpretation.

Step 2: Center Gate (V_c)
Next, the transmission amplitude was probed for different voltages applied stepwise to the center gate. Identical to step 1, the transmission amplitude is recorded as a function of V_{LPG} for different V_c. From the previous discussion, it is expected that at $\simeq$ -350 mV applied equally to center and resonator gate, the upper right region of the 2DEG becomes decoupled from the grounded reservoir and thereby floating (cf. Fig. 4). Fig. 66

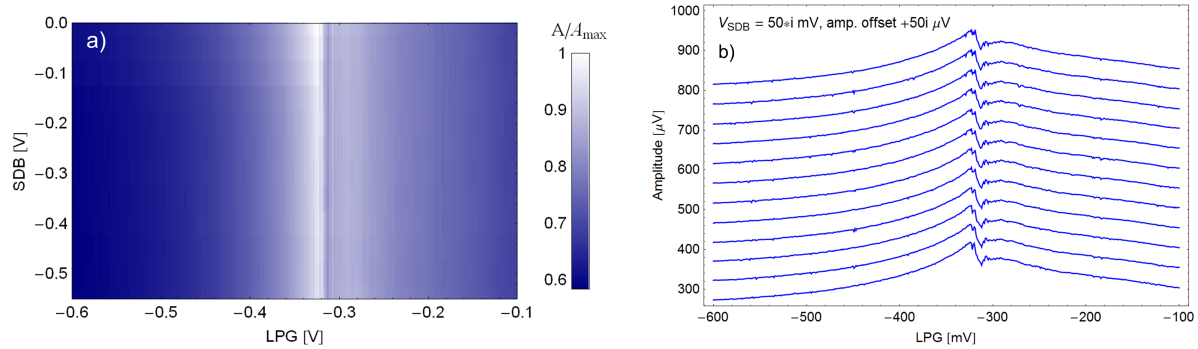

Figure 65: Transmission amplitude as a function of V_{LPG} at fixed frequency: False color image of the transmission amplitude for different V_{SDB} (a) and plotted transmission amplitude for different V_{SDB} (b). Note an offset of +50i with i ϵ [1,12], set for clarity. Appendix B [A23]

summarizes the results, however, no frequency shift is observable. Thus, V_c alone does not explain the shifted depletion region in LPG subspace which is assumed to be caused by a polarizable 2DEG, when floating. Still, this is in agreement with our theory. Although 2DEG at the right of the resonator gate is floating, the electron gas at the left stays well grounded.

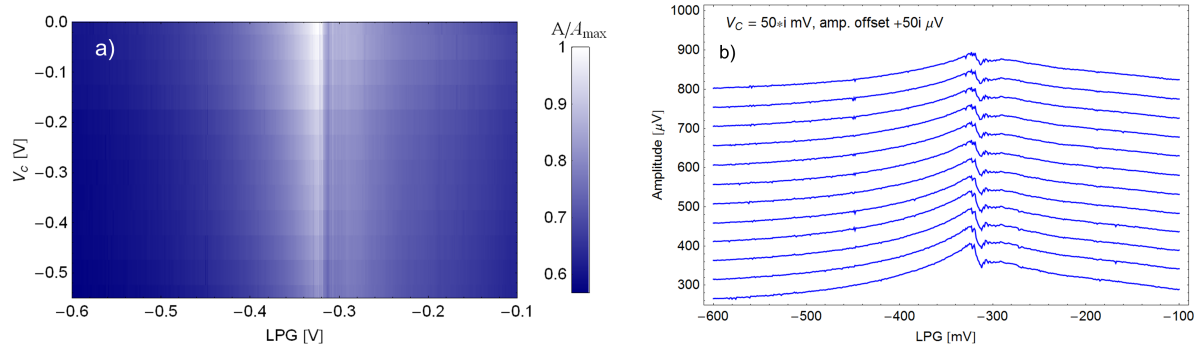

Figure 66: Transmission amplitude as a function of V_{LPG} at fixed frequency: False color image of the transmission amplitude for different V_c (a) and plotted transmission amplitude for different V_c (b). A constant offset was added for clarity. Appendix B [A24]

Step 3: Center Gate voltage equal to Left Side Gate voltage
In the following, the upper left and upper right part of the 2DEG are progressively decoupled from the grounded reservoir by equally setting left side gate (LSG) and center gate (V_c) more negative. At the same time, the transmitted amplitude is probed as a function of the voltage applied to the resonator gate (LSG). It turns out that below $V_c = V_{LSG} \simeq$ -320 mV, a linear shift of the depletion threshold in LPG-space becomes visible (cf. Fig. 67). This voltage appears to be typical and of the same range at which the resonator properties change abrupt by depleting electrons below LPG for all remaining gates set to 0 V (cf. Fig. 52). This behavior is understood because the depletion voltage is determined by the density of electrons which is assumed to be constant over the entire sample. Starting from this voltage, the upper part of the 2DEG becomes floating. Our model of a floating 2DEG in this region stays valid.

Step 4: Right Plunger Gate (Right Side Gate) equal to Left Side Gate voltage
In a last step, the upper 2DEG is isolated by successively setting the right plunger gate

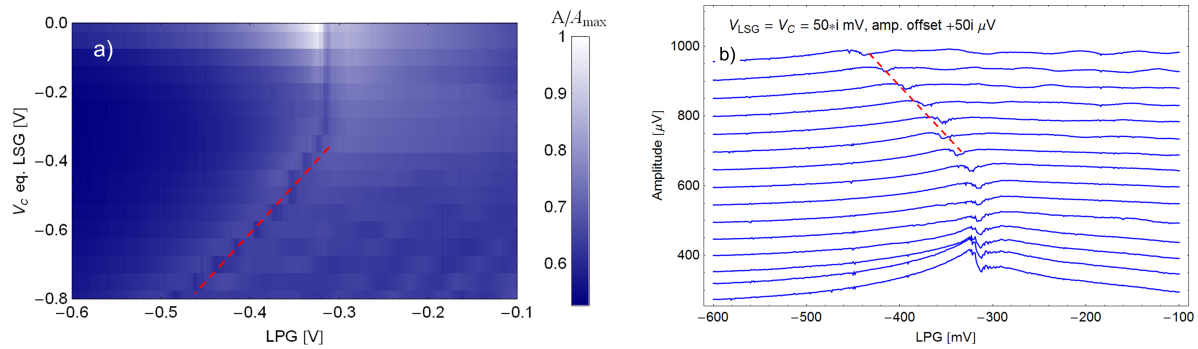

Figure 67: Transmission amplitude as a function of V_{LPG} at fixed frequency: False color image of the transmission amplitude for different $V_c = V_{LSG}$ (a) and plotted transmission amplitude for different $V_c = V_{LSG}$ (b). A constant offset was added for clarity. Appendix B [A25]

(RPG) in combination with the left side gate (LSG) more negative, thereby probing the transmission amplitude as a function of LPG. A linear shift of the depletion region below LSG, that indicates a transition to floating, appears at around $V_{RPG} = V_{LSG}$ = -600 mV. More negative voltage is necessary in comparison to step 3 as a channel between LSG and RPG remains that need to be closed first (cf. Fig. 4). The channel width is much narrower in step 3 compared to the case when decoupling the 2DEG by means of the gates $V_c = V_{LSG}$. This assumption is validated by isolating the 2DEG in terms of the right and left side gate, i.e. by setting successively $V_{RSG} = V_{LSG}$ more negative. Here, an even broader channel to the grounded 2DEG parts remain, compared to the case discussed before. A linear shift of the depletion region appears at around $V_{RPG} = V_{LSG}$ = -800 mV. A set of transmission amplitudes for fixed frequency is shown in Fig. 45 for the first (a) and second (b) discussed configuration.

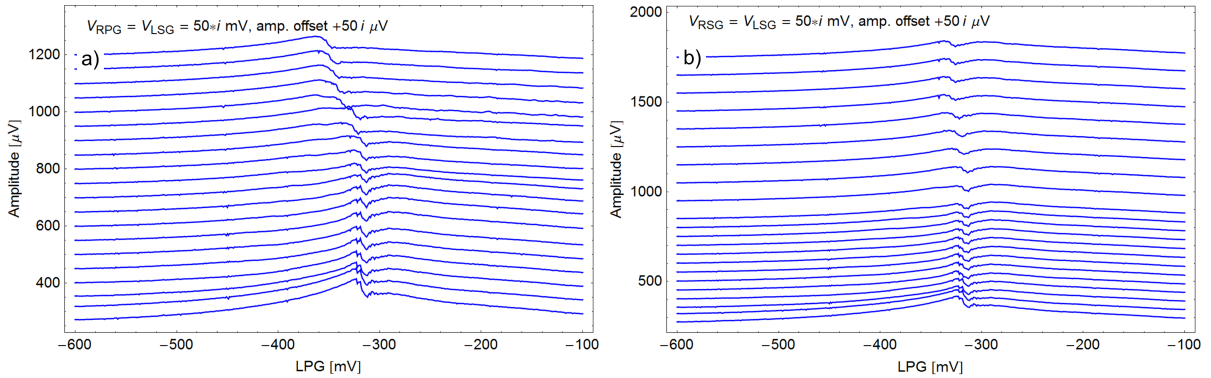

Figure 68: Transmission amplitude as a function of V_{LPG} at fixed frequency: Plotted transmission amplitude for different $V_{RPG} = V_{LSG}$ (a) $V_{RSG} = V_{LSG}$ (b). A constant offset was added for clarity. Full set of parameters available from Appendix B [A26, A27]

Conclusion:
Data presented and discussed in step 1 to step 4 are all consistent with the model of a floating 2DEG. The high-quality resonator is a sensitive tool for probing changes in the 2DEG such as a transition from grounded to floating and single electron processes, e.g. resonances due to localized charge states in islands close to the resonator gate. Although, initially not intended for experiments on a coupled resonator-DQD system, these studies nevertheless show that a transmission line resonator might be used as a sensitive

measuring device for dynamic processes in electron gases and for mesoscopic structures by probing the complex admittance. This may have the potential for new characterization methods in semiconductor nanostructure devices.

6.5 Implications for the next generation of samples

In the case of the currently used sample for microwave studies of a DQD charge qubit, the depletion of electrons below the resonator and the interplay of different gates on forming a floating 2DEG were important details to be considered. Those effects were not intended and avoidable by adjusting the design of the top-gates. It is necessary to avoid isolated pockets of 2DEG for any gate configurations such that the electron gas remains grounded everywhere except at the double quantum dot position. Furthermore, it is advantageous to decrease the area of electron gas below the resonator to avoid for an additional dissipative and decoherence channel. Ideally, the resonator characteristics shall be independent of top-gate configurations and only depend on the design parameters.

7 Conclusion and perspectives

Previous work by Loss and DiVincenzo proposed to use double quantum dots as quantum bits (DiVincenzo, Science 2005 [59]) and to implement a set of one and two qubit gates based on the spin states of two coupled single electron quantum dots (Loss and DiVincenzo, PRA 1998 [6], Burkard, Loss and DiVincenzo, PRB 1999 [60]). In an alternative scheme, charge states might be favorable in terms of coupling a double quantum dot (DQD) to a resonator and thereby probing the transition dipole moment. In this project, we studied a single electron double quantum dot charge qubit that is dipole coupled to a coplanar waveguide resonator which is a further step towards using semiconductor quantum dots for quantum information processing. Our system is a hybrid quantum device. A special aspect of the suggested system is the possibility to manipulate and probe the double quantum dot in electron transport as well as via a dipole coupling to a microwave resonator. A high controllability of charge states with applied top-gate voltages extends to various read-out concepts in this design approach. Additionally, the double quantum dot can be operated in the many, few or single electron regime at wish whereas the resonator stays sensitive for the dot characteristics in all these regimes. A major major goal of this project was to better understand the high dephasing rates of 0.9 GHz and 3.0 GHz that were reported in previously published experiments by Frey *et al.* [12]. In this previous work, the DQD was probed in the many electron regime at which some hundreds of electrons were estimated to be in each dot. However, in the many electron regime, closely spaced excited states are suspected to be a source of decoherence.

In the single electron regime, dephasing rates were found to range approximately from 400 MHz to 6 GHz in this work. These dephasing rates were obtained by comparing the experimental data with numerical simulations of the coupled system. The qubit relaxation was fixed at 100 MHz, maintaining a coupling of strength 25 MHz and a resonator linewidth of 7.4 MHz. A comparison to the many electron regime in the same sample showed higher relaxation rates in the many electron case, ranging from approximately 2.0 GHz to 17.0 GHz whereas a larger coupling strength of 50 MHz was estimated from a comparison between experimental data and numerical simulation. This comparison between numerical

and experimental data might validate our assumption of decoherence resulting from a coupling to excited states, although other mechanisms may contribute when comparing a single to a many electron dot. However, those results have to be considered with care as an estimate is only possible by a comparison between experimental data and simulation, leaving uncertainties in parameters that could not yet be obtained in experiments. This raises the questions on a selection of different measurement techniques that are best suited to extract as many parameters from the experiment as possible. By reducing the number of free parameters when numerically simulating the coupled resonator-qubit system, more accurate results on dephasing and its dependence on the tunneling rate in the single and many electron regime might be possible. This already sets an outlook for further measurements and improved measurement schemes.

Studies of the currently used sample design furthermore suggest improvements for the next sample generation. From measurements, it was evident that the resonator characteristics were sensitively dependent on applied top-gate voltages. Indeed, the resonator gate was seen to probe the state of the 2DEG beneath, such that differences in the 2DEG, independent of dot charge states, affected the resonator characteristics. For instance, large parts of 2DEG were situated underneath the resonator gate. This not only serves as an additional relaxation channel for resonator excitations, but also changes the resonator characteristics depending on a depletion of electrons under the resonator gate.

In conclusion, it was not yet possible to achieve strong coupling between resonator and double quantum dot as decoherence rates remained large and stayed comparable to previous measurements in GaAs [12]. It is essential to better understand the mechanisms that limit the coherence time in the currently used architecture and GaAs/AlGaAs heterostructure. Different sources might contribute such as excited states, phonon decoherence [50], electromagnetic field fluctuations on gates [51], fluctuating background charges [53] or leakage of charges from top-gates into the heterostructure [56], whereas fluctuating background charges are thought to dominate [53]. Although this thesis suggests that a hybridization to excited states is no major source of decoherence, various sources for decoherence remain. Recently published results by Toida *et al.* [13] on a lateral GaAs double quantum dot dipole coupled to a transmission line resonator however indicate significantly less dephasing. Thus, the material GaAs might not be the limiting factor which suggests to further study the architecture and heterostructure design. A first step for future experiments might be to optimize the setup in order to minimize voltage fluctuations on gates. Secondly it might be fruitful to analyze the current design approach in terms of decoherence and to further increase the coupling strength between resonator and qubit. In a third step, one might think about further studying GaAs/AlGaAs heterostructures to better understand decoherence mechanisms which limit current experiments. Altogether, there is no fundamental reason known up to date which prevents strong coupling and significantly less dephasing in such a system.

The approach to couple a double quantum dot qubit to a resonator is most promising in terms of quantum information processing devices. Despite a high controllability of charge states, quantum dots allow to experiment with single electrons and thereby give access to the spin degree of freedom. In the strong coupling regime, double quantum dots might serve as a versatile device in quantum networks respectively distributed quantum systems which are coupled through microwave transmission lines.

8 Appendix A: Formation of double quantum dot

1. **Determine $\mathbf{V}_{RSG}$**: Successively set RSG more negative and determine V_{RSG} at which the right side gate forms the right dot tunnel barrier via recording a pinchoff-curve. Note that RDB has to be biased such that the remaining channel between RDB and LSG is closed. Choose a voltage more negative than the voltage at which the pinch-off occurs. *Note that RSG has to be set increasingly more negative than the pinch-off value when a single-electron double quantum dot is formed which allows for less negative voltages applied to plunger gates when completely emptying the dot.*
2. **Determine $\mathbf{V}_{QPC}$**: Choose the voltage applied to the quantum point contact such that one measures at the first conductance resonance at a position where the slope is steepest.
3. **Determine $\mathbf{V}_{SDB}$**: Successively set the gate voltage for SDB more negative and determine at which voltage one pinches off the current between SDB and RSG. Choose the voltage applied to SDB more negative such that one pinches-off the current from a later DQD to the right lead. Later, tunnel processes should be possible here in the following, only.
4. **Determine $\mathbf{V}_c$**: Determine the voltage at which one pinches-off the current through the center barrier by setting the voltage at the center gate more negative while maintaining all previously applied voltage. The voltage for V_c should be chosen more negative than the threshold at which a pinch-off occurs. Later, only tunnel process should be allowed here.
5. **Determine $\mathbf{V}_{LSG}$**: Determines the coupling to the left lead. Determine a threshold at which one pinches-off the channel between SDB and LSG. Therefore, set the voltage applied to V_c back to 0 V and successively increase the voltage for LSG. Set the left side gate more negative than the pinch-off threshold. Only tunnel processes should be allowed between dot and left lead. Set V_{LSG} to a value such that the coupling to the left lead is similar to a coupling to the right lead for a symetrically coupled DQD to its leads. *Note that RSG has to be set significantly more negative than the pinch-off value when a single-electron double quantum dot is formed which allows for less negative voltages applied to plunger gates when completely emptying the dot.*
6. **Choose LPG-RPG subspace** to operate the dot in.
7. **Form the double quantum dot**: Set all gate voltages to the values determined in steps 1 - 6. No current flow should be possible when the voltages were chosen significantly more negative than the pinch-off threshold. Now, slightly set the voltage applied to SDB less negative while recording maps in LPG-RPG subspace. V_{SDB} should be chosen such that a direct current is visible at triple points respectively co-tunneling is visible in the charge stability diagram. SDB is chosen here in favour of LSG and RSG to achieve a enhance the coupling of the dot to its leads symmetrically for both leads. At the same time, the interdot coupling between both dots is increased.
8. **Check $\mathbf{V}_{QPC}$** : The voltage applied to QPC needs to be adjusted for maximal sensitivity once the double quantum dot was formed.

9 Appendix B: Parameter space

	Gate voltage in [mV]	Other
A1	LSG = 0, RSG = 0, V_c = 0, SDB = 0, RPG = 0, QPC = -920, RDB = -2000, LPG = -450, Bias CD 0, bias SD 0	pwr -7 dBm, avg 8192
A2	LSG = -635, RSG = -450, V_c = -390, SDB = -400, QPC = -750, RDB = -2000, Bias CD = 0.3, SD Bias = 0.025	
A3	LSG = -456, RSG = -340, V_c = -516, SDB = -725, QPC = -1120, RDB = -2000, Bias CD = 0.3, SD Bias = 0.025	
A4	LSG = -, RSG = -, V_c = -, SDB = , QPC = -, RDB = -, Bias CD = , SD Bias =	
A5	LSG = -648, RSG = -463, V_c = -301, SDB = -400, QPC = -710, RDB = -2000, Bias CD = 0.3 , SD Bias = 0.025	
A6	LSG = -648, RSG = -463, V_c = -297, SDB = -400, QPC = -750, RDB = -2000, Bias CD = 0 , SD Bias = 0 (LPG,RPG): (-417.75, -426.31) -> (-419.75, -460.31)	pwr -14 dBm, avg. 8192
A7	LSG = -648, RSG = -463, V_c = -297, SDB = -400, QPC = -750, RDB = -2000, Bias CD 0, Bias SD 0	pwr -7 dBm, avg 8192, ν_r = 6.76238 GHz
A8	LSG = -648, RSG = -463, V_c = -301, SDB = -400, QPC = -750, RDB = -2000, Bias CD 0, Bias SD 0	pwr -7 dBm, avg 8192 ν_r = 6.76199 GHz
A9	LSG = -633, RSG = -448, V_c = -320, SDB = -400, QPC = -750, RDB = -2000, Bias CD 0, bias SD 0	pwr -7 dBm, avg 8192 ν_r = 6.7629
A10	LSG = -577, RSG = -415.5, V_c = -365, SDB = -550, QPC = -920, RDB = -2000, Bias CD 0, bias SD 0	pwr -7 dBm, avg 8192 ν_r = 6.75737
A11	LSG = -648, RSG = -463, V_c = -301, SDB = -400, QPC = -710, RDB = -2000, Bias CD = 0.3 , SD Bias = 0.025	Lock-In: dIdVPG 0.2 didV 10
A12	LSG = -648, RSG = -463, V_c = -301, SDB = -400, QPC = -710, RDB = -2000, Bias CD = 0.3 , SD Bias = 0.025	Lock-In: dIdVPG 0.2 didV 10
A13	LSG = -648, RSG = -463, V_c = -301, SDB = -400, QPC = -750, RDB = -2000, Bias CD 0, bias SD 0	pwr -7 dBm, avg 8192 ν_r = 6.76199
A14	LSG = -648, RSG = -463, V_c = -301, SDB = -380, QPC = -750, RDB = -2000, Bias CD 0, Bias SD 0	pwr -14 dBm, avg 16384 ν_r = 6.76251 GHz
A15	LSG = -648, RSG = -463, SDB = -380, QPC = -750, RDB = -2000, Bias CD 0, Bias SD 0 (LPG,RPG): V_c = -306 (-417.75, -426.31) -> (-419.75, -460.31) V_c = -306 (LPG,RPG): (-419, -462) -> (-421, -460) V_c = -304, (LPG,RPG): (-419.82, -463.13) -> (-421.82, -461.13) V_c = -302, (LPG,RPG): (-420.82, -464.24) -> (-422.82, -462.24) V_c = -301, (LPG,RPG): (-421.14, -464.58) -> (-423.14, -462.58) V_c = -300, (LPG,RPG): (-421.62, -465.24) -> (-423.62, -463.24) V_c = -299, (LPG,RPG): (-420.64, -466.57) -> (-424.64, -462.57) V_c = -298.5, (LPG,RPG): (-422.3, -464.35) -> (-424.3, -462.35) V_c = -298, (LPG,RPG): (-421.9, -466.2) -> (-423.9, -464.2) V_c = -297.5, (LPG,RPG): (-418.04, -462.22) -> (-420.04, -460.22) V_c = -297, (LPG,RPG): (-417.75, -426.31) -> (-419.75, -460.31) V_c = -296, (LPG,RPG): (-422, -467.2) -> (-422, -465.2) V_c = -294, (LPG,RPG): (-424, -466.37) -> (-426, -464.37) V_c = -292, (LPG,RPG): (-424.5, -467.2) -> (-426.5, -465.2)	pwr -14 dBm, avg. 8192
A16	LSG = -490, RSG = -332, SDB = -725, QPC = -1120, RDB = -2000, Bias CD 0, Bias SD 0 (LPG,RPG): V_c = -306 (-417.75, -426.31) -> (-419.75, -460.31) V_c = -538 (LPG,RPG): (-0.71, -12) -> (-2.21, -10.3) V_c = -531, (LPG,RPG): (-2.95, -13.83) -> (-4.45, -12.33) V_c = -530, (LPG,RPG): (-3.32, -14.2) -> (-4.82, -12.7) V_c = -529, (LPG,RPG): (-3.4, -14.7) -> (-5.4, -12.7) V_c = -528, (LPG,RPG): (-3.6, -14.7) -> (-5.6, -12.7)	pwr -11 dBm, avg. 8192

	V_c = -527, (LPG,RPG): (-4.52, -15.19) -> (-6.02, -13.69) V_c = -526, (LPG,RPG): (-4.73, -15.41) -> (-6.23, -13.91) V_c = -525, (LPG,RPG): (-5.02, -15.67) -> (-6.52, -14.17) V_c = -523, (LPG,RPG): (-5.3, -15.79) -> (-6.8, -14.29) V_c = -518, (LPG,RPG): (-6.913, -17.25) -> (-8.475, -15.73)	
A17	LSG = 0, RSG = 0, V_c = 0, SDB = 0, RPG = 0, QPC = -920, RDB = -2000, Bias CD 0, bias SD 0	pwr -7 dBm, avg 8192
A18	LSG =-200, RSG = -200, V_c = -200, SDB = -200, RPG = -200, QPC = -920, RDB = -2000, Bias CD 0, bias SD 0	pwr -7 dBm, avg 8192
A19	LSG = -500, RSG = -500, V_c = -500, SDB = -500, RPG = -500, QPC = -920, RDB = -2000, Bias CD 0, bias SD 0	pwr -7 dBm, avg 8192
A20	LSG = -800, RSG = -800, V_c = -800, SDB = -800, RPG = -800, QPC = -920, RDB = -2000, Bias CD 0, bias SD 0	pwr -7 dBm, avg 8192
A21	LSG = 0, RSG = 0, V_c = 0, SDB = 0, RPG = 0, QPC = 0, RDB = 0, Bias CD 0, bias SD 0	pwr -7 dBm, avg 8192
A22	LSG = RSG = V_c = SDB = RPG = x mV, QPC = -920, RDB = -2000, Bias CD 0, bias SD 0	pwr -7 dBm, avg 8192
A23	LSG = RSG = V_c = RPG = LPG = QPC = RDB = 0, SDB = x mV, Bias CD 0, bias SD 0	pwr -7 dBm, avg 8192
A24	LSG = RSG = SDB = RPG = QPC = LPG = RDB = 0, V_c = x mV, Bias CD 0, bias SD 0	pwr -7 dBm, avg 8192
A25	RSG = SDB = RPG = LPG = QPC = RDB = 0, LSG = V_c = x mV, Bias CD 0, bias SD 0	pwr -7 dBm, avg 8192
A26	V_c = RSG = SDB = LPG = QPC = RDB = 0, LSG = RPG = x mV, Bias CD 0, bias SD 0	pwr -7 dBm, avg 8192
A27	V_c = LPG = SDB = RPG = QPC = RDB = 0, LSG = RSG = x mV, Bias CD 0, bias SD 0	pwr -7 dBm, avg 8192

Table 3: Set of applied parameters in experimental measurements

10 Appendix C: Microwave setup

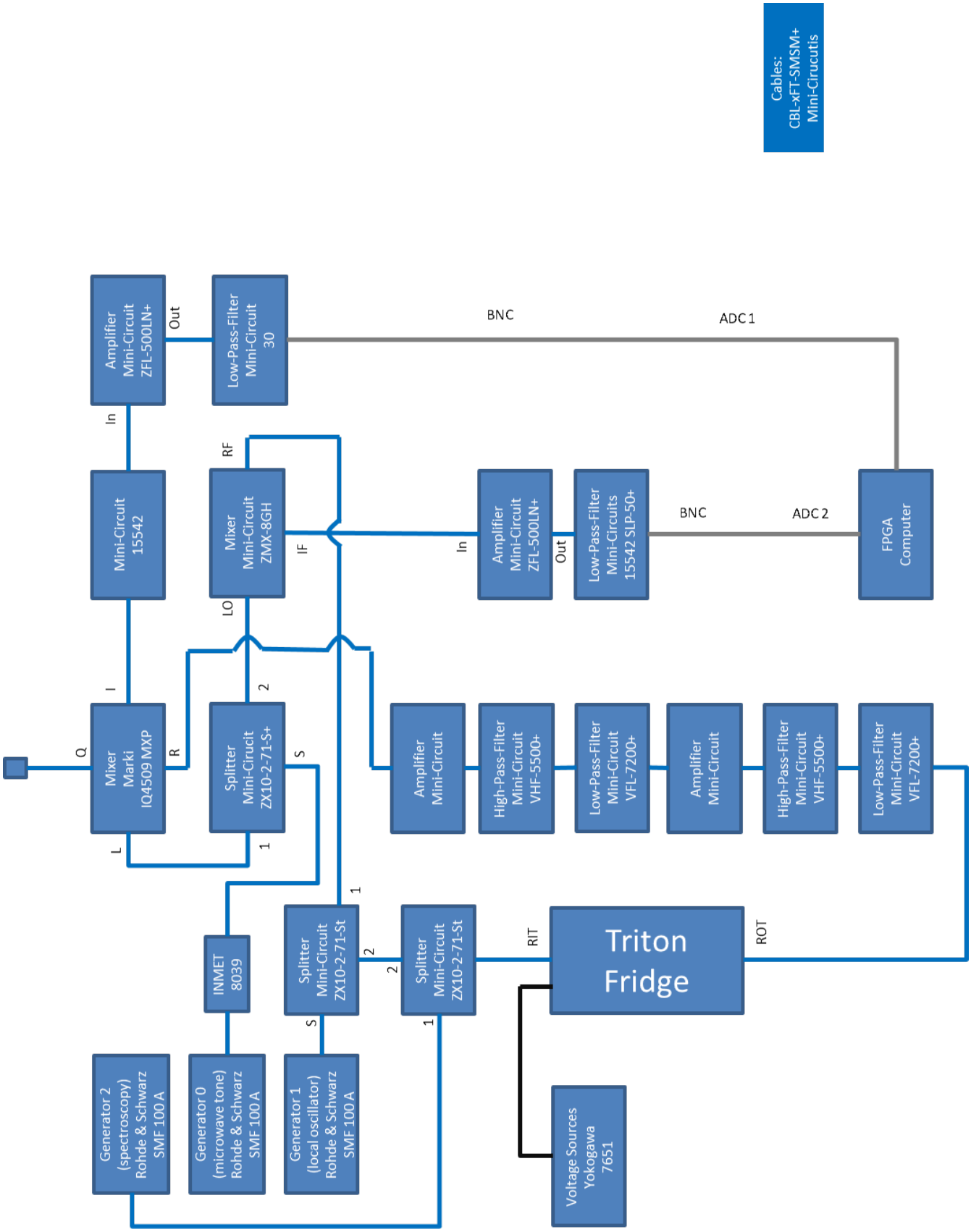

11 Appendix D: Decoherence from numerical simulations

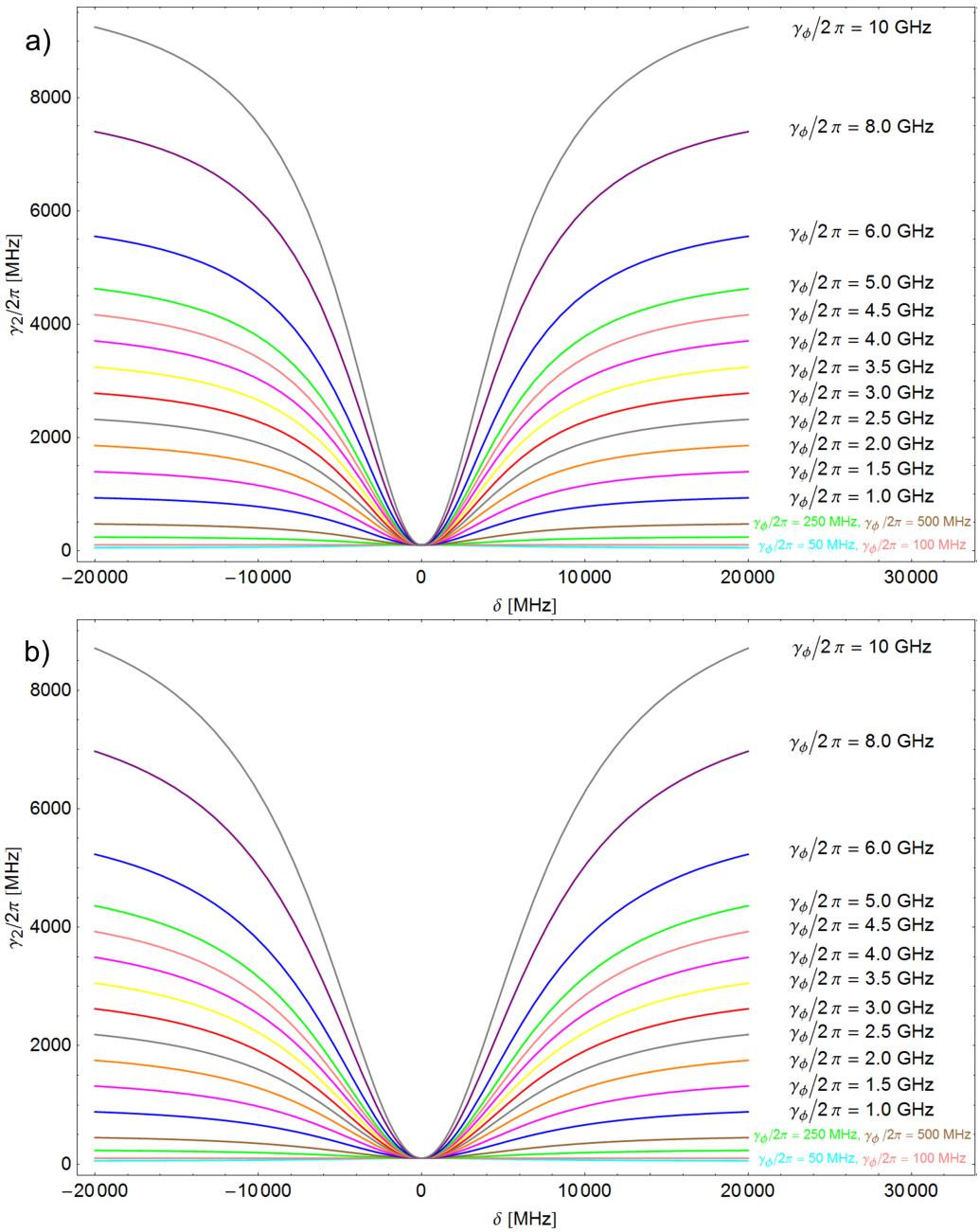

Figure 69: Decoherence rates calculated from Eq. (21) for 2t = 5750 MHz (a) and 2t = 7750 MHz (b). Further parameters: ν_r = 6762 MHz, g/2π = 25 MHz, $\gamma_1/2\pi$ = 100 MHz, T = 10 mK, n_{th} = 0.01, n_{ph} ϵ [0,5], ϵ = 0.1. Compare also section 5.5.3

12 Appendix E: Inhomogenous rates for exp. data (single electron DQD)

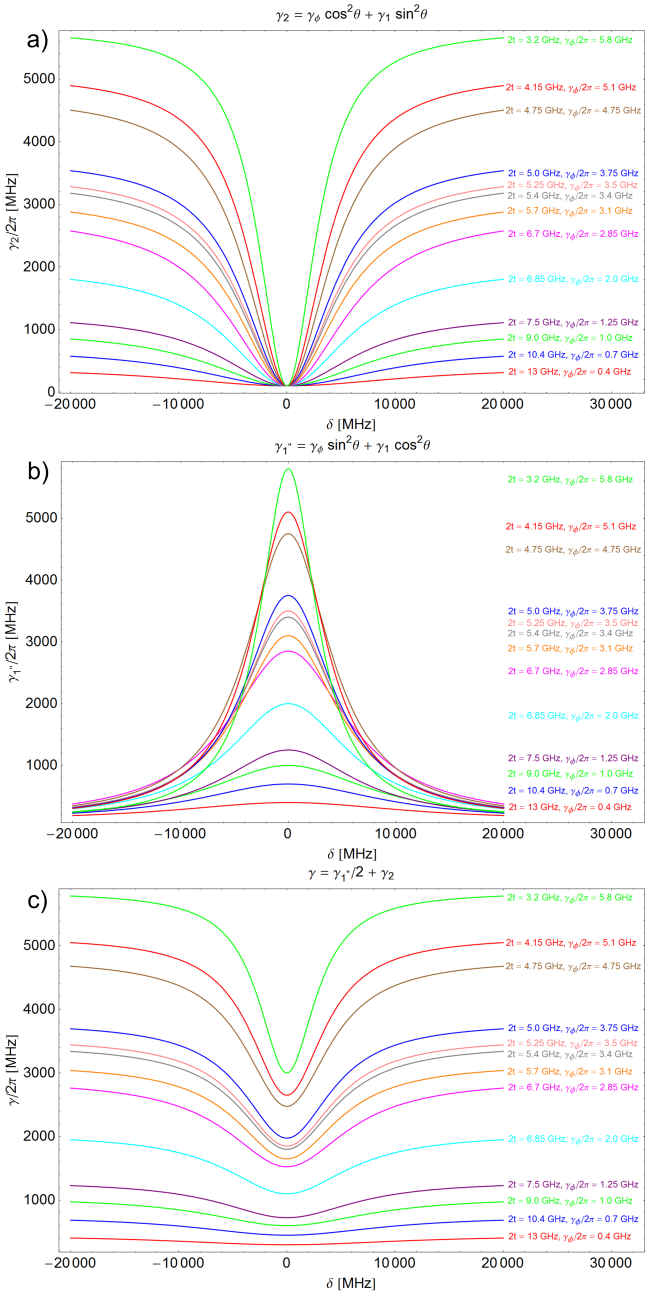

Figure 70: Inhomogenous rates for single electron regime based on Table1: Decoherence (a), relaxation (b), combined rate (c). γ_ϕ and γ_1 are bare dephasing and relaxation rates (cf. Eq. (21)) and $\tan\theta = 2\mathrm{t}/\delta$

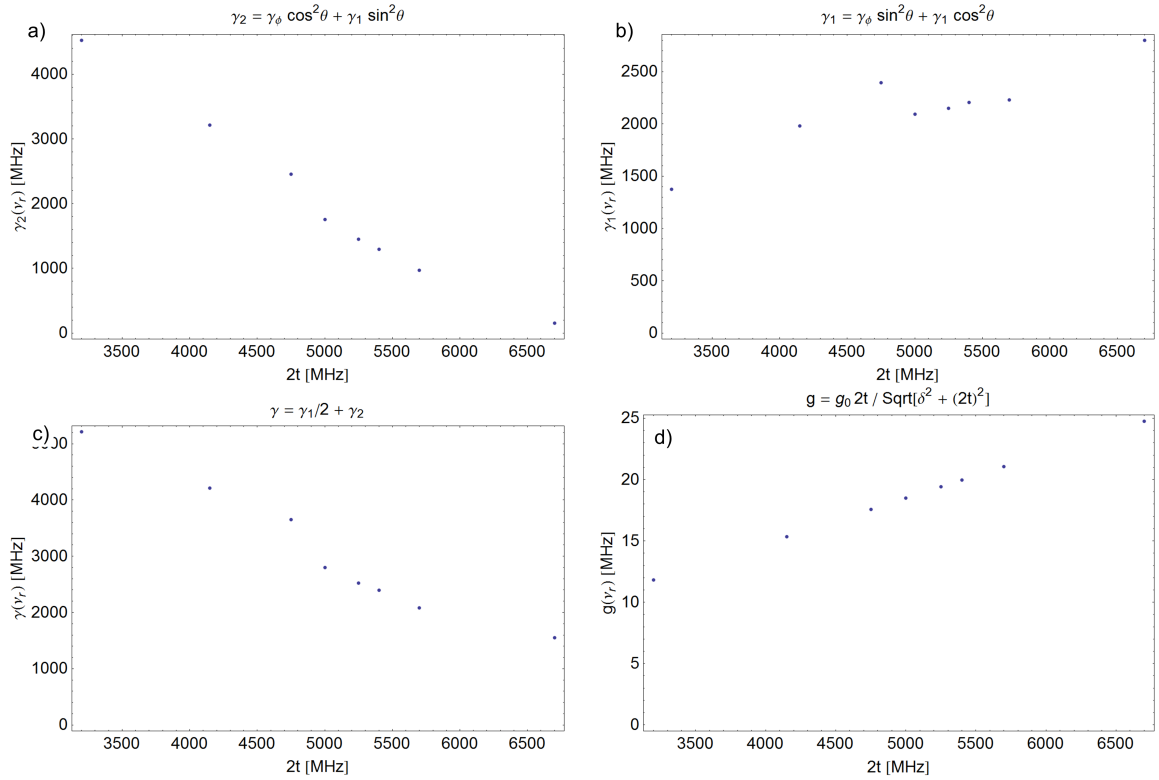

Figure 71: Inhomogenous rates for single electron regime based on Table 1 for qubit transition frequency Ω at resonator frequency ν_r: Decoherence (a), relaxation (b), combined rate (c) and coupling strength g (d). γ_ϕ and γ_1 are bare dephasing and relaxation rates (cf. Eq. (21)), tanθ = 2t/δ and g_0 = 25 MHz.

Acknowledgments

I would like to thank Dr. Julien Basset for his excellent support supervising the project and many valuable discussions. Special thanks to Tobias Frey for various interesting discussions about double quantum dots in the context of circuit QED.

Likewise, I would like to thank Prof. Klaus Ensslin and Prof. Thomas Ihn for many valuable discussions about experimental techniques and experimental data. Special thanks to Prof. Andreas Wallraff for numerous discussions on the experiment and circuit QED in general and for the possibility to conduct research in this fascinating field of physics.

Eventually, I would like to thank all members of the Quantum Device Lab and the Nanophysics group to make the lab such a nice place to work at.

References

[1] Michael A. Nielsen and Isaac L. Chuang. *Quantum Computation and Quantum Information*. Cambridge University Press, 2010.

[2] Peter W. Shor. Polynomial-time algorithms for prime factorization and discrete logarithms on a quantum computer. *SIAM Journal on Computing*, 26:1484–1509, 1997.

[3] Michael A. Nielsen and Isaac L. Chuang. *Quantum Computation and Quantum Information*, pages 277–279. Cambridge University Press, 2010.

[4] D. Leibfried, B. DeMarco, V. Meyer, D. Lucas, M. Barrett, J. Britton, W. M. Itano, B. Jelenkovic, C. Langer, T. Resonband, and D. J. Wineland. Experimental demonstration of a robust, high-fidelity geometric two ion-qubit phase gate. *Nature*, 422:412–415, 2003.

[5] A. Blais, R. - S. Huang, A. Wallraff, S. M. Girvin and R. J. Schoelkopf. Cavity quantum electrodynamics for superconducting electrical circuits: An architecture for quantum computation. *Physical Review A*, 69:062320, 2004.

[6] Daniel Loss and David P. DiVincenzo. Quantum computation with quantum dots. *Physical Review A*, 57:120–126, 1998.

[7] A. Wallraff, D. I. Schuster, A. Blais, L. Frunzio, R.-S. Huang, J. Majer, Kumar, S. M. Girvin and R. J. Schoelkopf. Strong coupling of a single photon to a superconducting qubit using circuit quantum electrodynamics. *Nature*, 431:162–167, 2004.

[8] A. Fedorov, L. Steffen, M. Baur, M. P. da Silva and A. Wallraff. Implementation of a toffoli gate with superconducting circuits. *Nature*, 481:170–172, 2012.

[9] H. J. Kimble. The quantum internet. *Nature*, 453:1023–1030, 2008.

[10] K. D. Petersson, L. W. McFaul, M. D. Schroer, M. Jung, J. M. Taylor, A. A. Houck and J. R. Petta. Circuit quantum electrodynamics with a spin qubit. *Nature*, 490:380–383, 2012.

[11] J. R. Petta, A. C. Johnson, J. M. Taylor, E. A. Laird, A. Yacoby, M. D. Lukin, C. M. Marcus, M. P. Hanson, A. C. Gossard. Coherent manipulation of coupled electron spins in semiconductor quantum dots. *Science*, 309:2180–2184, 2005.

[12] M. Beck A. Blais T. Ihn K. Ensslin T. Frey, P. J. Leek and A. Wallraff. Dipole coupling of a double quantum dot to a microwave resonator. *Physical Review Letters*, 108:046807, 2012.

[13] H. Toida, T. Nakajima, S. Komiyama. Vacuum rabi splitting in a semiconductor circuit QED system. *Physical Review Letters*, 110:066802, 2013.

[14] T. Frey, P. J. Leek, M. Beck, J. Faist, A. Wallraff, K. Ensslin and T. Ihn. Quantum dot admittance probed at microwave frequencies with an on-chip resonator. *Physical Review B*, 86:115303, 2012.

[15] T. Frey, P. J. Leek, M. Beck, K. Ensslin, A. Wallraff and T. Ihn. Characterization of a microwave frequency resonator via a nearby quantum dot. *Applied Physics Letters*, 98:262105, 2011.

[16] K. D. Petersson, C. G. Smith, D. Anderson, P. Atkinson, G. A. C. Jones, and D. A. Ritchie. Charge and spin state readout of a double quantum dot coupled to a resonator. *Nano Letters*, 10:2789–2793, 2010.

[17] M. Field, C. G. Smith, M. Pepper, D. A. Ritchie, J. E. F. Frost, G. A. C. Jones, and D. G. Hasko. Measurements of coulomb blockade with a noninvasive voltage probe. *Physical Review Letters*, 70:1311–1314, 1993.

[18] Thomas Ihn. *Semiconductor Nanostructures*. Oxford University Press, 2010.

[19] Zhiming M. Wang. *Self-Assembled Quantum Dots*. Springer, 2007.

[20] Thomas Ihn. *Semiconductor Nanostructures*, chapter 9.3. Capacitance between top gate and electron gas. Oxford University Press, 2010.

[21] D. Graf, M. Frommenwiler, P. Studerus, T. Ihn, K. Ensslin, D. C. Driscoll, and A. C. Gossard. Local oxidation of Ga[Al]As hetrostructures with modulated tip-sample voltages. *Journal of Applied Physics*, 99:053707, 2006.

[22] Thomas Ihn. *Semiconductor Nanostructures*, chapter 5 Material aspects of heterostructures, doping, surfaces, and gating. Oxford University Press, 2010.

[23] A. Wallraff, D. I. Schuster, A. Blais, L. Frunzio, R.-S. Huang, J. Majer, S. Kumar, S. M. Girvin, and J. R. Schoelkopf. Circuit quantum electrodynamics: Coherent coupling of a single photon to a cooper pair box. *extendet version of Nature (London)*, 431:162.

[24] Anna Stockklauser. Few electron double quantum dots for a circuit QED architecture. Master Thesis, ETH Zurich, 2012.

[25] M. Goeppl, A. Fragner, M. Baur, R. Bianchetti, S. Filipp et al. Coplanar waveguide resonators for circuit quantum electrodynamics. *Journal of Applied Physics*, 104:113904, 2008.

[26] W.G. van der Wiel, S. De Franceschi and J. M. Elzermann, T. Fujisawa, S. Tarucha, L. P. Kouwenhoven. Electron transport through double quantum dots. *Review of Modern Physics*, 75, 2003.

[27] Francoise Molitor. Electronic properties of graphene nanostructures. Ph.D. Thesis, ETH Zurich, Diss. ETH No. 19153.

[28] Leo P. Kouwenhoven, Charles M. Marcus, Paul L. McEuen, Seigo Tarucha, Robert M. Westervelt, and Ned S. Wingreen. *Electron Transport in Quantum Dots*. Kluwer, 1997.

[29] Thomas Ihn. *Semiconductor Nanostructures*, chapter 11 Ballistic electron transport in quantum point contacts. Oxford University Press, 2010.

[30] L. DiCarlo, H. J. Lynch, A. C. Johnson, L.I. Childress, K. Chrockett, C. M. Marcu, M. P. Hanson, A. C. Gossard. Differential charge sensing and charge delocalization in a tunable double quantum dot. *Physical Review Letters*, 92:22, 2004.

[31] D. Taubert, D. Schuh, W. Wegscheider, and S. Ludwig. Determination of energy scales in few-electron double quantum dots. *Review of Scientific Instruments*, 82:123905, 2011.

[32] W.G. van der Wiel, T. Fujisawa, T. H. Oosterkamp, L. P. Kouwenhoven. Microwave spectroscopy of a double quantum dot in the low- and high-power regime. *Physica B*, 272:31–35, 1999.

[33] A. W. Holleitner, H. Quin, F. Simmel, B. Irmer, R. H. Blick, J. P. Koffhaus, A. V. Ustinov and K. Eberl. Microwave spectroscopy on a double quantum dot with on-chip josephson oscillator. *New Journal of Physics*, 2, 2000.

[34] Bruno Kueng, Simon Gustavsson, Theodore Choi, Ivan Shorubalko, Oliver Pfaeffi, Fabian Hassler, Gianni Blatter, Matthias Reinwald, Werner Wegscheider, Silke Schoen, Thomas Ihn, and Klaus Ensslin. Measurement back-action in quantum-point-contact charge sensing. *Entropy*, 12(7):1721–1732, 2010.

[35] T. Duty, G. Johansson, K. Bladh, D. Gunnarsson, C. Wilson, and P. Delsing. Observation of quantum capacitance in the cooper-pair transistor. *Physical Review Letters*, 95:206807, 2005.

[36] Takeshi Ota, Toshiaki Hayashi, Koji Muraki, Toshimasa Fujisawa. Wide-band capacitance measurement on a semiconductor double quantum dot for studying tunneling dynamics. *Applied Physics Letters*, 96:032104, 2010.

[37] J. Gabelli, G. Feve, J-M. Berroir, B. Placais. A Coherent RC Circuit. *arxiv:1210.2874v1*, cond-mat.mes-hall, 2012.

[38] L. Childress, A. S. Sorensen and M. D. Lukin. Mesoscopic cavity quantum electrodynamics with quantum dots. *Physical Review A*, 69:042302, 2004.

[39] Alexandre Blais, Jay Gambetta, A. Wallraff, D. I. Schuster, S. M. Girvin, M. H. Devoret, and R. J. Schoelkopf. Quantum-information processing with circuit quantum electrodynamics. *Physical Review A*, 75:032329, 2007.

[40] Serge Haroche and Jean-Michel Raimond. *Exploring the Quantum - Atoms, Cavities, and Photons*, chapter 3.2.5 Beam-splitters as couplers to the environment: damping of a coherent state. Oxford University Press, 2011.

[41] Scully and Zubairy. *Quantum Optics*. Cambridge University Press, 2001.

[42] Christopher Gerry, Peter Knight. *Introductory Quantum Optics*, chapter 4.8 The Jaynes-Cummings model with large detuning: a dispersive interaction. Cambridge University Press, 2011.

[43] J. R. Petta, A. C. Johnson, J. M. Taylor, A. Yacoby, M. D. Lukin, C. M. Marcus, M. P. Hanson, A. C. Gossard. Charge and spin manipulation in a few-electron double dot. *Physica E*, 43:42–46, 2006.

[44] J. R. Petta, A. C. Johnson, C. M. Marcus, M. P. Hanson, and A. C. Gossard. Manipulation of a single charge in a double quantum dot. *Physical Review Letters*, 93:186802, 2004.

[45] K. D. Pettersson, J. R. Petta, H. Lu, and A. C. Gossard. Quantum coherence in a one-electron semiconductor charge qubit. *Physical Review Letters*, 105:246804, 2010.

[46] Alexandre Blais. Alexandre.Blais@USherbrooke.ca.

[47] Maxime Boissonneault. Mesure et retroaction sur un qubit multi-niveaux en electrodynamique quantique en circuit non lineaire. Ph.D. Thesis, Universite de Sherbrooke, 2011.

[48] Serge Haroche and Jean-Michel Raimond. *Exploring the Quantum - Atoms, Cavities, and Photons*. Oxford University Press, 2011.

[49] Tobias Frey, ETH Zurich. Private communication.

[50] Serguei Vorojtsov, Eduardo R. Mucciolo, and harold U. Barranger. Phonon decoherence of a double quantum dot charge qubit. *Physical Review B*, 71:205322, 2005.

[51] Diego C. B. Valente, Eduardo R. Mucciolo, and F. K. Wilhelm. Decoherence by electromagnetic fluctuations in double-quantum-dot charge qubits. *Physical Review B*, 82:125302, 2010.

[52] Toshifumi Itakura and Yasuhiro Tokura. Dephasing due to background charge fluctations. *Physical Review B*, 67:195320, 2003.

[53] Igor V. Yurkevich, Jim Baldwin, Igor V. Lerner, and Boris L. Altshuler. Decoherence of charge qubit coupled to interacting background charges. *Physical Review B*, 81:121305, 2010.

[54] O. Astfiev, Yu. A. Pashkin, Y. Nakamura, T. Yamamoto, and J. S. Tsai. Temperature square dependence of the low frequency 1/f charge noise in the josephson junction qubit. *Physical Review Letters*, 96:137001, 2006.

[55] Y.M. Galperin, B. L. Altshuler, D. V. Shatsev. Low-frequency noise as a source of dephasing of a qubit. *arXiv:cond-mat/0312490v1*, 2003.

[56] Christo Buizert, Frank H. L. Koppens, Michel Pioro-Ladriere, Hans-Peter Tranitz, Ivo T. Vink, Seigo Tarucha, Werner Wegscheider, And Lieven M. K. Vandersypen. Insitu reduction of charge noise in GaAs/AlGaAs schottky-gated devices. *Physical Review Letters*, 101:226603, 2008.

[57] M. Pioro-Ladriere, John H. Davies, A. R. Long, A. S. Sachrajda, Louis Gaudreau, P. Zawadzki, J. Lapointe, J. Gupta, Z. Wasilewski, and S. Studenikin. Decoherence of charge qubit coupled to interacting background charges. *Physical Review B*, 81:121305, 2010.

[58] Supriyo Datta. *Electron Transport in Mesoscopic Systems*, chapter 1.3 Characteristic lengths. Cambridge University Press, 1995.

[59] David P. DiVincenzo. Double quantum dot as a quantum bit. *Science*, 309:2173, 2005.

[60] Guido Burkard, Daniel Loss and David P. DiVincenzo. Coupled quantum dots as quantum gates. *Physical Review B*, 59:2070, 1999.